Supporting Information

Borylation and rearrangement reactions of azasilaanthracenes to afford B,N-doped nanographenes

Elena Zender[a], Danillo Valverde[b], Robert Neubaur[a], Sebastian Karger[a], Alexander Virovets[a], Michael Bolte[a], Hans-Wolfram Lerner[a], Yoann Olivier*[b], and Matthias Wagner*[a]

[a]*Institut für Anorganische und Analytische Chemie, Goethe-Universität Frankfurt, Max-von-Laue-Straße 7, D-60438 Frankfurt (Main), Germany*

[b]*Laboratory for Computational Modeling of Functional Materials, Namur Institute of Structured Matter, University of Namur, Rue de Bruxelles, 61, 5000 Namur, Belgium*

*To whom correspondence should be addressed.

Email: yoann.olivier@unamur.be; matthias.wagner@chemie.uni-frankfurt.de

Table of Contents

1. Experimental details and characterization data

General Considerations. If not stated otherwise, all reactions and manipulations were carried out under an atmosphere of dry nitrogen or argon using Schlenk techniques or in an inert-atmosphere glovebox. *n*Pentane, C_6D_6, and *o*-dichlorobenzene were dried over Na metal; C_6H_6, toluene, and THF were dried over Na/benzophenone; CH_2Cl_2 and CD_2Cl_2 were dried over CaH_2. Prior to use, the solvents were distilled from the drying agents. Toluene for coupling reactions was degassed by applying three freeze-pump-thaw cycles. BBr_3 was stored over Hg to remove traces of Br_2. All other commercially available starting materials were used as received. The starting materials 9,10-dihydro-10,10-dimethyl-9-aza-10-silaanthracene,[S1] mesitylmagnesium bromide (MesMgBr; Mes = mesityl),[S2] dimesitylzinc (Mes_2Zn),[S3] and mesityllithium (MesLi)[S4] were prepared according to literature procedures.

NMR spectra were recorded at 298 K using the following *Bruker* spectrometers: *Avance II 300*, *Avance III 400 HD*, *Avance III 500 HD*, or *Avance DRX 600*. Chemical shift values are referenced to (residual) solvent signals ($^1H/^{13}C\{^1H\}$; $CDCl_3$: δ = 7.26/77.16 ppm; CD_2Cl_2: δ = 5.32/53.84 ppm; C_6D_6: δ = 7.16/128.06 ppm), external $BF_3{\cdot}Et_2O$ (^{11}B: 0.00 ppm), or external $SiMe_4$ (^{29}Si: 0.00 ppm).[S5] Abbreviations: s = singlet, d = doublet, dd = doublet of doublets, ddd = doublet of doublets of doublets, t = triplet, m = multiplet, br = broad, n.o. = not observed. Resonances of carbon atoms attached to boron atoms were typically broadened and sometimes only observed in ^1H-^{13}C-HMBC NMR experiments due to the quadrupolar relaxation of boron. Boron resonances of triarylborane compounds are typically very broad ($h_{1/2}$ > 1100 Hz) and were only observed in highly concentrated samples. Resonance assignments were aided by ^1H-^1H-COSY, ^1H-^{13}C-HSQC, and ^1H-^{13}C-HMBC NMR experiments. The numbering schemes sometimes deviate from IUPAC recommendations and follow the nomenclature given in the reaction schemes.

Microwave-assisted reactions were carried out in a *Biotage Initiator*$^+$ synthesizer using septum-capped vials; the temperature was monitored by an infrared sensor. UV/Vis absorption spectra were recorded at room temperature using a *Varian Cary 60 Scan* UV/Vis spectrophotometer. UV/Vis absorption measurements were performed using solutions in the concentration range 2×10^{-5}–1×10^{-5} M. Photoluminescence (PL) spectra were recorded at room temperature using a *Jasco FP-8300* spectrofluorometer equipped with a calibrated *Jasco ILF-835* 100 mm diameter integrating sphere and analyzed using the *Jasco FWQE-880* software. For PL quantum yield (Φ_{PL}) measurements, each sample was carefully degassed with argon using an injection needle and a septum-capped cuvette. Under these conditions, the Φ_{PL} of the fluorescence standard 9,10-diphenylanthracene was determined as 97% (lit: 97%).[S6,S7] For all Φ_{PL} measurements, at least three samples of different concentrations were used (range 10^{-5}–10^{-7} M). PMMA layers for emission spectra and decay curves were prepared by dissolving ca. 2 mg of sample in toluene (3 mL) and triturating this solution with 1.6 g of PMMA powder. The resulting dispersion (approximately 200 µL) was placed in a cylindrical sample holder with a diameter of 13 mm and dried at 40 °C under vacuum. The resulting PMMA-dispersed layer (ca. 0.1 wt%) was then examined spectroscopically. Emission spectra and decay curves were recorded with an *Edinburgh Instruments FLS920* fluorescence spectrometer equipped with an *OSRAM* 450 W xenon arc lamp for the emission spectra, an *OSRAM* xenon flash lamp for the µs decay times, and a *COHERENT* 375 nm Obis laser for the ns decay time. A sample chamber installed with a mirror optic for powder samples was used. For detection, a *Hamamatsu R2658P* single-photon counting photomultiplier tube was used. The decay curves were fitted by a single exponential to determine the lifetimes.

Cyclic voltammetry (CV) measurements were performed in a glovebox at room temperature in a one-chamber, three-electrode cell using an *EG&G Princeton Applied Research 263A* potentiostat. A platinum-disk electrode (2.00 mm diameter) was used as the working electrode with a platinum-wire counter electrode and a silver-wire reference electrode, which was coated with AgCl by immersion into

HCl/HNO_3 (3:1). Prior to measurements, the solvent THF was dried over Na/benzophenone, distilled, and degassed by applying three freeze-pump-thaw cycles. [nBu$_4$N][PF_6] (*Sigma Aldrich*; used as received) was employed as the supporting electrolyte (0.1 M; concentration of each respective analyte: 1 mM). All potential values were referenced against the FcH/FcH^+ redox couple (FcH = ferrocene; $E_{1/2}$ = 0 V). Scan rates were varied between 100 and 600 mV s^{-1}. High-resolution mass spectra were measured in positive-ion mode using a *Thermo Fisher Scientific MALDI LTQ Orbitrap XL* or *Bruker Apollo II MTP timsTOFfleX* (MALDI) and α-cyano-4-hydroxycinnamic acid or *trans*-2-[3-(4-*t*-butylphenyl)-2-methyl-2-propenylidene]malononitrile as the matrix.

1.1. Synthesis of 1

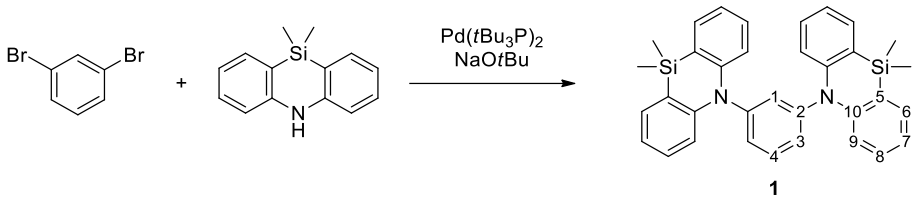

1

A microwave vial was charged with 9,10-dihydro-10,10-dimethyl-9-aza-10-silaanthracene (0.505 g, 2.24 mmol), Pd(*t*Bu$_3$P)$_2$ (57.2 mg, 0.112 mmol), and NaO*t*Bu (0.460 g, 4.79 mmol), closed with a septum cap, evacuated, and re-filled with argon. After the addition of 1,3-dibromobenzene (0.25 g, 1.1 mmol) and degassed toluene (20 mL), the mixture was heated to 170 °C in a microwave reactor for 1 h. The reaction mixture was cooled to room temperature and filtered through a short plug of neutral Al_2O_3 using C_6H_6 as the eluent. All volatiles were removed from the filtrate under reduced pressure to afford **1** as a colorless solid. Yield: 0.560 g (1.07 mmol, 97%).

Single crystals suitable for X-ray diffraction were grown by slow evaporation of a solution of **1** in *n*hexane/CH_2Cl_2.

Note: **1** decomposes upon prolonged contact with silica gel.

^{1}H NMR (500.2 MHz, $CDCl_3$): δ = 7.87 (t, $^3J_{HH}$ = 7.9 Hz, 1H, H-4), 7.55 (dd, $^3J_{HH}$ = 7.2 Hz, $^4J_{HH}$ = 1.7 Hz, 4H, H-6), 7.45 (dd, $^3J_{HH}$ = 7.9 Hz, $^4J_{HH}$ = 2.0 Hz, 2H, H-3), 7.21–7.18 (m, 5H, H-1, H-8), 6.97 (ddd, $^3J_{HH}$ = 7.2 Hz, $^3J_{HH}$ = 7.2 Hz, $^4J_{HH}$ = 0.9 Hz, 4H, H-7), 6.54 (br d, $^3J_{HH}$ = 8.6 Hz, 4H, H-9), 0.48 (s, 12H, Si(CH_3)$_2$).

^{13}C{^{1}H} NMR (125.8 MHz, $CDCl_3$): δ = 149.2 (C-10), 146.9 (C-2), 134.5 (C-6), 133.6 (C-1), 133.1 (C-4), 130.7 (C-3), 130.0 (C-8), 120.2 (C-7), 119.8 (C-5), 117.3 (C-9), 0.4 (Si(CH_3)$_2$).

^{29}Si{^{1}H} NMR (99.4 MHz, $CDCl_3$): δ = –24.5.

HRMS (MALDI) *m/z*: $[M]^{\bullet+}$ calculated for $[C_{34}H_{32}N_2Si_2]^{\bullet+}$: 524.20985, found: 524.20917.

1.2. Synthesis of 3^{Mes}

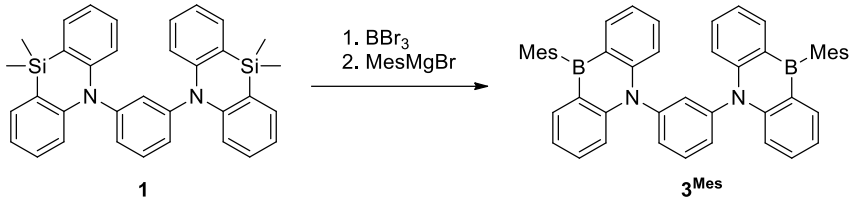

1 **3^{Mes}**

A glass tube fitted with a J. Young PTFE valve was charged with **1** (33.2 mg, 63.3 µmol), BBr_3 (0.03 mL, 0.08 g, 0.3 mmol), and CH_2Cl_2 (1.5 mL). After stirring for 1 d at room temperature with the valve closed, all volatiles were removed from the mixture under reduced pressure and the residue was dissolved in toluene (3 mL). The solution was cooled to –78 °C and MesMgBr (1.39 M in THF, 0.14 mL, 0.19 mmol) was added dropwise with stirring. The reaction mixture was allowed to reach room temperature and stirred overnight. The mixture was filtered through a short plug of silica gel using $CHCl_3$ as the eluent. All volatiles were removed from the filtrate under reduced pressure. After column chromatography (silica gel, C_6H_{12}:$CHCl_3$ = 4:1), the product **3^{Mes}** was obtained as a colorless solid. Yield: 17.6 mg (26.3 µmol, 42%).

The reported ^{1}H NMR shift values are consistent with literature data.[S1]

^{1}H NMR (500.2 MHz, $CDCl_3$): δ = 8.14 (t, $^3J_{HH}$ = 7.9 Hz, 1H), 7.89 (dd, $^3J_{HH}$ = 7.7 Hz, $^4J_{HH}$ = 1.7 Hz, 4H), 7.81 (dd, $^3J_{HH}$ = 7.9 Hz, $^4J_{HH}$ = 2.0 Hz, 2H), 7.63 (ddd, $^3J_{HH}$ = 8.7 Hz, $^3J_{HH}$ = 7.0 Hz, $^4J_{HH}$ = 1.7 Hz, 4H), 7.52 (t, $^4J_{HH}$ = 2.0 Hz, 1H), 7.15 (ddd, $^3J_{HH}$ = 7.7 Hz, $^3J_{HH}$ = 7.0 Hz, $^4J_{HH}$ = 0.9 Hz, 4H), 7.11 (br d, $^3J_{HH}$ = 8.7 Hz, 4H), 6.99 (s, 2H), 6.95 (s, 2H), 2.42 (s, 6H), 2.08 (s, 6H), 1.92 (s, 6H).

1.3. Synthesis of 4

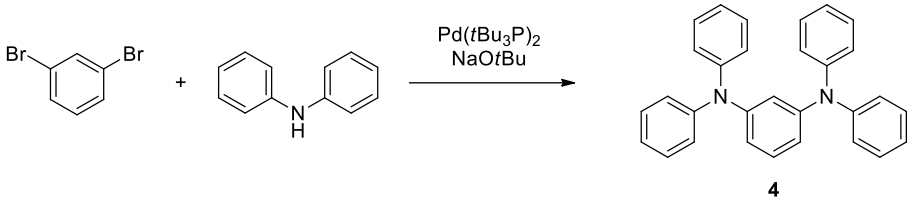

4

A microwave vial was charged with 1,3-dibromobenzene (0.104 g, 0.441 mmol), diphenylamine (0.150 g, 0.886 mmol), Pd(tBu$_3$P)$_2$ (0.022 g, 0.043 mmol), and NaOtBu (0.180 g, 1.87 mmol), closed with a septum cap, evacuated, and re-filled with argon. After the addition of degassed toluene (5 mL), the mixture was heated to 170 °C in a microwave reactor for 1 h. The reaction mixture was cooled to room temperature and filtered through a short plug of neutral Al_2O_3 using C_6H_6 as the eluent. All volatiles were removed from the filtrate under reduced pressure and the solid residue was washed with *n*hexane (4 x 3 mL) to afford **4** as a colorless solid. Yield: 0.098 g (0.24 mmol, 54%).

The reported ^{1}H NMR shift values are consistent with literature data.[S8]

^{1}H NMR (400.1 MHz, $CDCl_3$): δ = 7.22–7.18 (m, 8H), 7.10–7.04 (m, 9H), 6.96 (br t, $^3J_{HH}$ = 7.3 Hz, 4H), 6.87 (t, $^4J_{HH}$ = 2.2 Hz, 1H), 6.66 (dd, $^3J_{HH}$ = 8.1 Hz, $^4J_{HH}$ = 2.2 Hz, 2H).

1.4. Synthesis of 2^{Br}

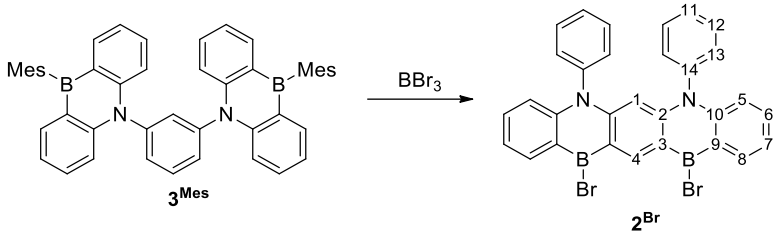

3^{Mes} 2^{Br}

An NMR tube was charged with $\mathbf{3^{Mes}}$ (21.1 mg, 31.6 µmol), BBr_3 (0.04 mL, 0.1 g, 0.4 mmol), and C_6H_6 (0.5 mL). The NMR tube was flame-sealed under vacuum and subsequently heated to 180 °C in an oven for 59 h. After cooling to room temperature, whereupon a red precipitate formed, the NMR tube was opened and the liquid was separated from the solid *via* syringe. The solid was washed with C_6H_6 (2 x 0.5 mL). All volatiles were removed under reduced pressure to afford $\mathbf{2^{Br}}$ as a red solid.

Single crystals suitable for X-ray diffraction were grown by slowly cooling the reaction mixture to room temperature in a sand bath.

Note: The product was not clean enough, judging from its ^{1}H NMR spectrum, to determine a reliable yield. It was not possible to purify the product further due to its high sensitivity to water. However, we were able to determine the structure *via* 2D NMR spectroscopy, single-crystal X-ray structure analysis, and conversion of $\mathbf{2^{Br}}$ into $\mathbf{2^{Mes}}$ (see below).

^{1}H NMR (500.2 MHz, CD_2Cl_2): δ = 9.78 (s, 1H, H-4), 8.55 (dd, $^3J_{HH}$ = 7.8 Hz, $^4J_{HH}$ = 1.7 Hz, 2H, H-8), 7.54 (ddd, $^3J_{HH}$ = 8.7 Hz, $^3J_{HH}$ = 7.0 Hz, $^4J_{HH}$ = 1.7 Hz, 2H, H-6), 7.47–7.44 (m, 6H, H-11, H-12), 7.27 (ddd, $^3J_{HH}$ = 7.8 Hz, $^3J_{HH}$ = 7.0 Hz, $^4J_{HH}$ = 0.9 Hz, 2H, H-7), 7.08–7.06 (m, 4H, H-13), 6.76 (br d, $^3J_{HH}$ = 8.7 Hz, 2H, H-5), 5.78 (s, 1H, H-1).

^{13}C{^{1}H} NMR (125.8 MHz, CD_2Cl_2): δ = 150.5 (C-2), 149.6 (C-4), 147.8 (C-10), 141.1 (C-14), 136.7 (C-8), 134.5 (C-6), 131.2 (C-12), 129.9 (C-13), 129.3 (C-11), 124.5* (br, C-9), 121.2 (C-7), 119.7* (br, C-3), 117.6 (C-5), 103.2 (C-1). *) This signal was detected through a ^{1}H-^{13}C-HMBC NMR experiment.

^{11}B NMR (160.5 MHz, CD_2Cl_2): δ = 50.1 (br).

1.5. Synthesis of 2^{Mes}

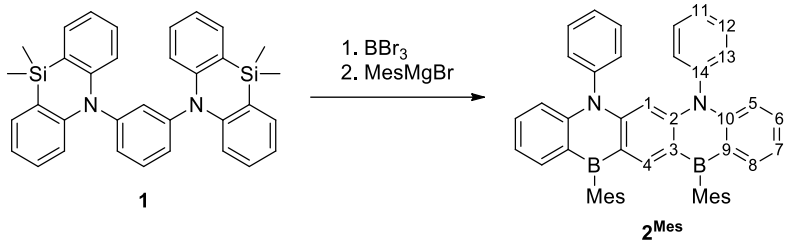

1 2^{Mes}

Method A: A thick-walled glass ampoule was charged with **1** (0.112 g, 0.213 mmol), BBr_3 (0.24 mL, 0.63 g, 2.5 mmol), and C_6H_6 (3 mL). The ampoule was flame-sealed under vacuum and subsequently heated to 180 °C in an oven for 116 h. After cooling to room temperature, whereupon a red precipitate formed, the ampoule was opened and the content transferred to a Schlenk tube. All volatiles were removed under reduced pressure and the residue was suspended in toluene (5 mL). After cooling the suspension to –78 °C, MesMgBr (1.39 M in THF, 0.46 mL, 0.64 mmol) was added dropwise with stirring. The reaction mixture was allowed to warm to room temperature and stirred overnight. The mixture was filtered through a short plug of silica gel using $CHCl_3$ as the eluent. All volatiles were removed from the filtrate under reduced pressure. After column chromatography (silica gel, C_6H_{12}:$CHCl_3$ = 4:1), the product $\mathbf{2^{Mes}}$ was obtained as a yellow solid. Yield: 0.056 g (0.084 mmol, 39%).

Note: The red precipitate formed in this reaction could be identified as $\mathbf{2^{Br}}$ (see section 1.4).

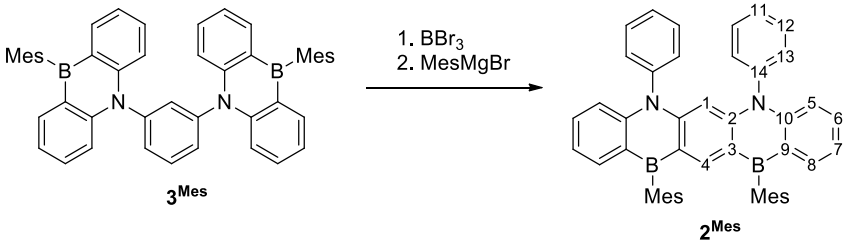

3^{Mes} 2^{Mes}

Method B: A thick-walled glass ampoule was charged with $\mathbf{3^{Mes}}$ (50.2 mg, 75.1 µmol), BBr_3 (0.09 mL, 0.2 g, 0.9 mmol), and C_6H_6 (2 mL). The ampoule was flame-sealed under vacuum and subsequently heated to 180 °C in an oven for 92 h. After cooling to room temperature, whereupon a red precipitate formed, the ampoule was opened and the liquid was separated from the solid *via* syringe. The solid was washed with C_6H_6 (2 x 1 mL) and all volatiles were removed under reduced pressure. The solid was transferred to a Schlenk tube and suspended in toluene (3 mL). After cooling the suspension to –78 °C, MesMgBr (1.39 M in THF, 0.16 mL, 0.22 mmol) was added dropwise with stirring. The reaction mixture was allowed to warm to room temperature and stirred overnight. The mixture was filtered through a short plug of silica gel using $CHCl_3$ as the eluent. All volatiles were removed from the filtrate under reduced pressure. After column chromatography (silica gel, C_6H_{12}:$CHCl_3$ = 4:1), the product $\mathbf{2^{Mes}}$ was obtained as a yellow solid. Yield: 21.9 mg (32.8 µmol, 44%).

Note: When this reaction was carried out in C_6D_6 instead of C_6H_6, partial deuteration of the product took place. See section 1.11.2 for further details.

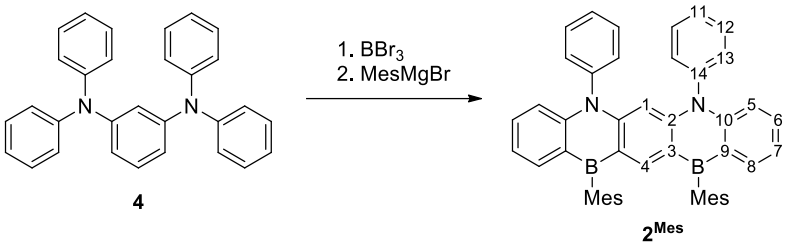

4 **2^{Mes}**

Method C: A thick-walled glass ampoule was charged with **4** (41.4 mg, 0.100 mmol), BBr_3 (0.11 mL, 0.29 g, 1.2 mmol), and *o*-dichlorobenzene (1.5 mL). The ampoule was flame-sealed under vacuum and subsequently heated to 180 °C in an oven for 112 h. After cooling to room temperature, the ampoule was opened and the red-colored content transferred to a Schlenk tube. All volatiles were removed under reduced pressure and the residue was suspended in toluene (5 mL). After cooling the suspension to –78 °C, MesMgBr (0.90 M in THF, 0.33 mL, 0.30 mmol) was added dropwise with stirring. The reaction mixture was allowed to reach room temperature and stirred overnight. The mixture was filtered through a short plug of silica gel using $CHCl_3$ as the eluent. All volatiles were removed from the filtrate under reduced pressure. After column chromatography (silica gel, C_6H_{12}:$CHCl_3$ = 4:1), the product **2^{Mes}** was obtained as a yellow solid. Yield: 38.8 mg (58.0 µmol, 58%).

Single crystals suitable for X-ray diffraction were grown by recrystallization of **2^{Mes}** from acetone.

^{1}H NMR (500.2 MHz, $CDCl_3$): δ = 8.23 (s, 1H, H-4), 7.87 (dd, $^3J_{HH}$ = 7.6 Hz, $^4J_{HH}$ = 1.5 Hz, 2H, H-8), 7.47–7.41 (m, 8H, H-6, H-11, H-12), 7.18–7.16 (m, 4H, H-13), 7.06 (ddd, $^3J_{HH}$ = 7.6 Hz, $^3J_{HH}$ = 6.9 Hz, $^4J_{HH}$ = 0.9 Hz, 2H, H-7), 6.82 (s, 4H, Mes-CH-*m*), 6.74 (br d, $^3J_{HH}$ = 8.6 Hz, 2H, H-5), 5.77 (s, 1H, H-1), 2.36 (s, 6H, Mes-CH_3-*p*), 1.95 (s, 12H, Mes-CH_3-*o*).

^{13}C{^{1}H} NMR (125.8 MHz, $CDCl_3$): δ = 151.0 (C-4), 150.2 (C-2), 147.3 (C-10), 141.6 (C-14), 139.3* (br, Mes-C-*i*), 139.0 (Mes-C-*o*), 137.5 (C-8), 136.2 (Mes-C-*p*), 132.8 (C-6), 130.7 (C-12), 130.1 (C-13), 128.4 (C-11), 126.6 (Mes-CH-*m*), 126.2* (br, C-9), 120.6* (br, C-3), 120.0 (C-7), 116.8 (C-5), 102.0 (C-1), 23.4 (Mes-CH_3-*o*), 21.3 (Mes-CH_3-*p*). *) This signal was detected through a ^{1}H-^{13}C-HMBC NMR experiment.

^{11}B NMR (160.5 MHz, $CDCl_3$): δ = n.o.

HRMS (MALDI) *m/z*: $[M]^{\bullet+}$ calculated for $[C_{48}H_{42}B_2N_2]^{\bullet+}$: 668.3529, found: 668.3536.

1.6. Synthesis of 5

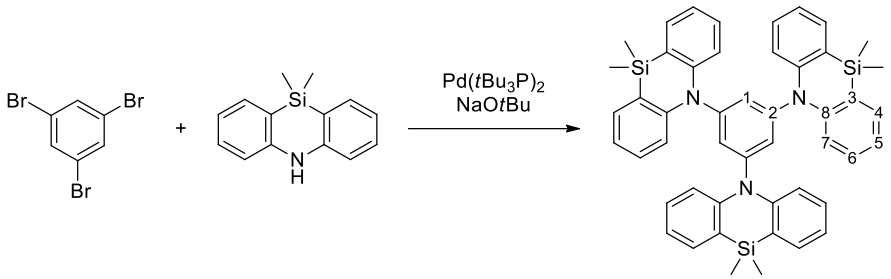

5

A microwave vial was charged with 1,3,5-tribromobenzene (0.205 g, 0.651 mmol), 9,10-dihydro-10,10-dimethyl-9-aza-10-silaanthracene (0.430 g, 1.91 mmol), Pd(tBu$_3$P)$_2$ (0.049 g, 0.096 mmol), and NaOtBu (0.364 g, 3.79 mmol), closed with a septum cap, evacuated, and re-filled with argon. After the addition of degassed toluene (10 mL), the mixture was heated to 170 °C in a microwave reactor for 1 h. The reaction mixture was cooled to room temperature and filtered through a short plug of neutral Al_2O_3 using C_6H_6 as the eluent. All volatiles were removed from the filtrate under reduced pressure. The resulting solid was washed with *n*hexane (4 x 4 mL) to afford **5** as a colorless solid. Yield: 0.460 g (0.615 mmol, 94%).

Single crystals suitable for X-ray diffraction were grown by recrystallization of **5** from acetone.

^{1}H NMR (500.2 MHz, $CDCl_3$): δ = 7.54 (dd, $^3J_{HH}$ = 7.2 Hz, $^4J_{HH}$ = 1.7 Hz, 6H, H-4), 7.27 (ddd, $^3J_{HH}$ = 8.6 Hz, $^3J_{HH}$ = 7.2 Hz, $^4J_{HH}$ = 1.7 Hz, 6H, H-6), 7.09 (s, 3H, H-1), 7.02 (ddd, $^3J_{HH}$ = 7.2 Hz, $^3J_{HH}$ = 7.2 Hz, $^4J_{HH}$ = 0.9 Hz, 6H, H-5), 6.86 (br d, $^3J_{HH}$ = 8.6 Hz, 6H, H-7), 0.46 (s, 18H, Si(CH_3)$_2$).

^{13}C{^{1}H} NMR (125.8 MHz, $CDCl_3$): δ = 149.1 (C-2), 149.0 (C-8), 134.5 (C-4), 130.1 (C-6), 125.5 (C-1), 122.7 (C-3), 121.2 (C-5), 119.1 (C-7), –0.3 (Si(CH_3)$_2$).

^{29}Si{^{1}H} NMR (99.4 MHz, $CDCl_3$): δ = –23.5.

HRMS (MALDI) *m/z*: $[M]^{\bullet+}$ calculated for $[C_{48}H_{45}N_3Si_3]^{\bullet+}$: 747.2916, found: 747.2911.

1.7. Synthesis of 8

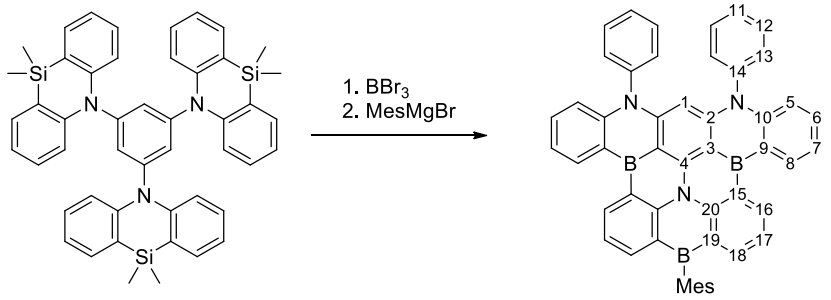

5 **8**

A thick-walled glass ampoule was charged with **5** (0.082 g, 0.11 mmol), BBr_3 (0.29 mL, 0.77 g, 3.1 mmol), and C_6H_6 (1.5 mL). The ampoule was flame-sealed under vacuum and subsequently heated to 180 °C in an oven for 7 d. After cooling to room temperature, whereupon a red precipitate formed, the ampoule was opened and the liquid removed *via* syringe. The remaining solid was washed with *n*pentane (2 x 0.5 mL) and transferred to a Schlenk tube. All volatiles were removed under reduced pressure and the residue was suspended in toluene (15 mL). After cooling the suspension to –78 °C, MesMgBr (1.39 M in THF, 0.47 mL, 0.65 mmol) was added dropwise with stirring. The reaction mixture was allowed to warm to room temperature and stirred overnight. The mixture was filtered through a short plug of silica gel using $CHCl_3$ as the eluent. All volatiles were removed from the filtrate under reduced pressure. After column chromatography (silica gel, C_6H_{12}:$CHCl_3$ = 10:1 to 4:1), the product **8** was obtained as a yellow solid. Yield: 23.0 mg (31.8 µmol, 29%).

Single crystals suitable for X-ray diffraction were grown by slow evaporation of a solution of **8** in $CHCl_3$.

Note: (i) When this reaction was performed on a larger scale (0.28 mmol of **5**), the yield of **8** dropped to 16%; when MesLi was used instead of MesMgBr, no **8** could be isolated at all. (ii) **6**, **7**, and $\mathbf{2^{Mes}}$ are also products of this reaction. However, we were not able to separate **6** and **7** completely from **8** and $\mathbf{2^{Mes}}$, respectively, *via* column chromatography (see section 1.8 for a synthesis protocol for **6** and **7**).

^{1}H NMR (600.2 MHz, $CDCl_3$): δ = 9.31 (dd, $^3J_{HH}$ = 7.0 Hz, $^4J_{HH}$ = 2.1 Hz, 2H, H-16 or H-18), 8.77 (dd, $^3J_{HH}$ = 7.7 Hz, $^4J_{HH}$ = 1.6 Hz, 2H, H-8), 8.41 (dd, $^3J_{HH}$ = 7.0 Hz, $^4J_{HH}$ = 2.1 Hz, 2H, H-16 or H-18), 7.74 (dd, $^3J_{HH}$ = 7.0 Hz, $^3J_{HH}$ = 7.0 Hz, 2H, H-17), 7.51–7.45 (m, 8H, H-6, H-11, H-12), 7.33 (ddd, $^3J_{HH}$ = 7.7 Hz, $^3J_{HH}$ = 6.9 Hz, $^4J_{HH}$ = 1.0 Hz, 2H, H-7), 7.22–7.20 (m, 4H, H-13), 7.06 (s, 2H, Mes-CH-*m*), 6.82 (br d, $^3J_{HH}$ = 8.5 Hz, 2H, H-5), 5.68 (s, 1H, H-1), 2.48 (s, 3H, Mes-CH_3-*p*), 2.11 (s, 6H, Mes-CH_3-*o*).

^{13}C{^{1}H} NMR (150.9 MHz, $CDCl_3$): δ = 149.7 (C-2), 148.7 (C-4), 147.4 (C-20), 147.3 (C-10), 142.3 (C-16 or C-18), 142.2 (C-14), 142.1 (C-16 or C-18), 140.1* (br, Mes-C-*i*), 139.6 (Mes-C-*o*), 136.9 (Mes-C-*p*), 135.8 (C-8), 131.1 (C-6), 130.9 (C-12), 130.2 (C-13), 129.0* (br, C-15 or C-19), 128.4 (C-11), 127.4* (br, C-15 or C-19), 127.2 (Mes-CH-*m*), 123.5* (br, C-9), 122.8 (C-17), 120.7 (C-7), 117.1 (C-5), 113.2* (br, C-3), 97.0 (C-1), 23.6 (Mes-CH_3-*o*), 21.5 (Mes-CH_3-*p*). *) This signal was detected through a ^{1}H-^{13}C-HMBC NMR experiment.

^{11}B NMR (160.5 MHz, $CDCl_3$): δ = n.o.

HRMS (MALDI) *m/z*: $[M]^{\bullet+}$ calculated for $[C_{51}H_{36}B_3N_3]^{\bullet+}$: 723.3183, found: 723.3210.

1.8. Synthesis of 6 and 7

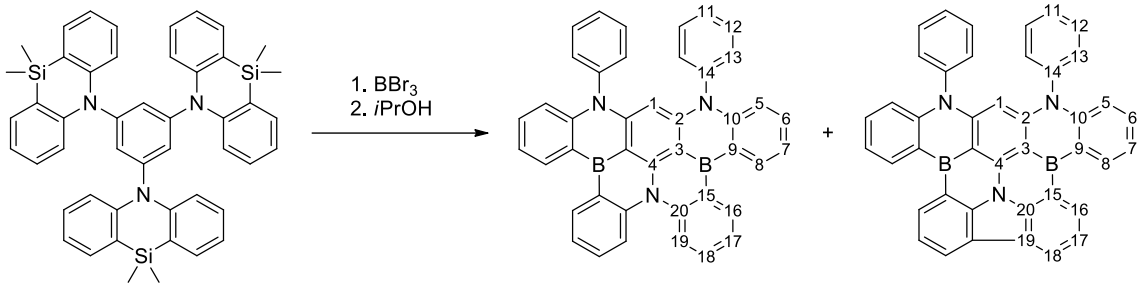

5 **6** **7**

A thick-walled glass ampoule was charged with **5** (238.2 mg, 318.4 µmol), BBr_3 (0.91 mL, 2.4 g, 9.6 mmol), and C_6H_6 (5 mL). The ampoule was flame-sealed under vacuum and subsequently heated to 180 °C in an oven for 11 d. After cooling to room temperature, whereupon a red precipitate formed, the ampoule was opened and the liquid removed *via* syringe. The remaining solid was washed with *n*hexane (3 x 1 mL) and dissolved in CH_2Cl_2 (70 mL) and *i*PrOH (5 mL). The mixture was filtered through a short plug of silica gel using CH_2Cl_2 as the eluent. All volatiles were removed from the filtrate under reduced pressure. After column chromatography (silica gel, C_6H_{12}:CH_2Cl_2 = 10:1), the products **6** and **7** were obtained as yellow solids. Yield: **6**: 11.3 mg (19.0 µmol, 6%); **7**: 16.6 mg (28.0 µmol, 9%).

Single crystals suitable for X-ray diffraction were grown by slow evaporation of a solution of **6** in CH_2Cl_2/toluene and recrystallization of **7** from C_6H_6.

Note: (i) **6** is not long-term stable in $CHCl_3$ under ambient conditions, especially in highly diluted solutions. See Figure S27 for a study of the decomposition of **6** in $CHCl_3$/$CDCl_3$. (ii) **6** has previously been published in a patent by Hatakeyama *et al.* with ^{1}H NMR data.[S9] We provide a full characterization below.

6:

^{1}H NMR (500.2 MHz, $CDCl_3$): δ = 8.91 (dd, $^3J_{HH}$ = 7.4 Hz, $^4J_{HH}$ = 1.7 Hz, 2H, H-8), 8.82 (dd, $^3J_{HH}$ = 7.6 Hz, $^4J_{HH}$ = 1.7 Hz, 2H, H-16), 8.31 (br d, $^3J_{HH}$ = 8.5 Hz, 2H, H-19), 7.54 (ddd, $^3J_{HH}$ = 8.5 Hz, $^3J_{HH}$ = 7.1 Hz, $^4J_{HH}$ = 1.7 Hz, 2H, H-18), 7.48–7.41 (m, 10H, H-6, H-11, H-12, H-17), 7.34 (br dd, $^3J_{HH}$ = 7.4 Hz, $^3J_{HH}$ = 7.4 Hz, 2H, H-7), 7.14–7.12 (m, 4H, H-13), 6.81 (br d, $^3J_{HH}$ = 8.5 Hz, 2H, H-5), 5.25 (s, 1H, H-1).

^{13}C{^{1}H} NMR (125.8 MHz, $CDCl_3$): δ = 149.8 (C-2), 147.6 (C-10), 147.0 (C-20), 141.9 (C-14), 134.9 (C-8), 134.6 (C-16), 131.1 (C-6), 131.0/130.4/129.9[#] (br, C-12, C13), 130.8* (br, C-15), 129.0 (C-18), 128.3 (C-11), 124.0 (C-19), 123.9* (br, C-9), 123.5 (C-17), 120.6 (C-7), 117.2 (C-5), 110.9* (br, C-3), 93.9 (C-1), n.o. (C-4). [#]) There are three broadened signals for C-12 and C-13, which we cannot assign further due to overlapping cross peaks in the 2D NMR spectra. All in all, this observation points toward a hindered rotation about the N–Ph bonds due to the helical distortion of the molecule. In line with that, (motional) broadening of the H-12 and H-13 signals can also be seen in the ^{1}H NMR spectrum. *) This signal was detected through a ^{1}H-^{13}C-HMBC NMR experiment.

^{11}B NMR (160.5 MHz, $CDCl_3$): δ = n.o.

HRMS (MALDI) *m/z*: $[M]^{\bullet+}$ calculated for $[C_{42}H_{27}B_2N_3]^{\bullet+}$: 595.2386, found: 595.2402.

7:

^{1}H NMR (500.2 MHz, $CDCl_3$): δ = 9.17 (dd, $^{3}J_{HH}$ = 7.4 Hz, $^{4}J_{HH}$ = 1.7 Hz, 2H, H-8), 9.10 (br d, $^{3}J_{HH}$ = 7.5 Hz, 2H, H-16), 8.50 (dd, $^{3}J_{HH}$ = 7.5 Hz, $^{4}J_{HH}$ = 0.9 Hz, 2H, H-18), 7.80 (dd, $^{3}J_{HH}$ = 7.5 Hz, $^{3}J_{HH}$ = 7.5 Hz, 2H, H-17), 7.48–7.42 (m, 8H, H-6, H-11, H-12), 7.34 (br dd, $^{3}J_{HH}$ = 7.4 Hz, $^{3}J_{HH}$ = 7.4 Hz, 2H, H-7), 7.18–7.16 (m, 4H, H-13), 6.83 (br d, $^{3}J_{HH}$ = 8.5 Hz, 2H, H-5), 5.29 (s, 1H, H-1).

^{13}C{^{1}H} NMR (125.8 MHz, $CDCl_3$): δ = 151.4 (C-2), 147.6 (C-10), 142.4 (C-4), 141.9 (C-14, C-20), 135.4 (C-8), 133.1 (C-16), 131.2, (C-6) 130.8 (C-12), 130.1 (C-13), 128.4 (C-11), 126.1* (br, C-9), 125.4 (C-19), 124.0 (C-18), 123.3 (C-17), 123.0* (br, C-15), 120.5 (C-7), 117.5 (C-5), 110.8* (br, C-3), 94.5 (C-1). *) This signal was detected through a ^{1}H-^{13}C-HMBC NMR experiment.

^{11}B NMR (160.5 MHz, $CDCl_3$): δ = n.o.

HRMS (MALDI) *m/z*: $[M]^{\bullet+}$ calculated for $[C_{42}H_{25}B_2N_3]^{\bullet+}$: 593.2229, found: 593.2244.

1.9. Synthesis of 9^{Mes}

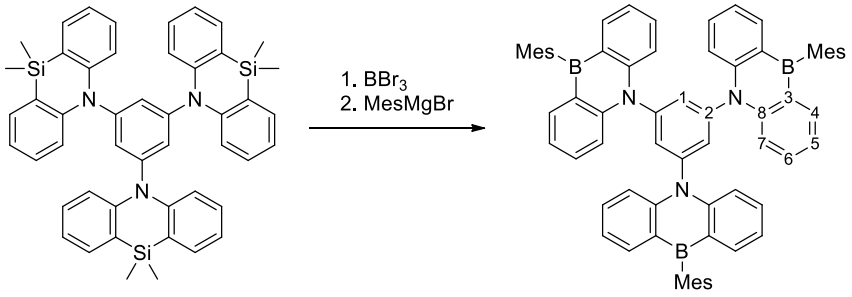

5 **9^{Mes}**

A glass tube fitted with a J. Young PTFE valve was charged with **5** (0.208 g, 0.278 mmol) and excess neat BBr_3 (2.0 mL). After stirring for 1 d at room temperature with the valve closed, all volatiles were removed from the mixture under reduced pressure and the residue was suspended in toluene (8 mL). The suspension was cooled to –78 °C and MesMgBr (1.39 M in THF, 0.90 mL, 1.3 mmol) was added dropwise with stirring. The reaction mixture was allowed to reach room temperature and stirred overnight. The mixture was filtered through a short plug of silica gel using $CHCl_3$ as the eluent. All volatiles were removed from the filtrate under reduced pressure. After column chromatography (silica gel, C_6H_{12}:$CHCl_3$ = 4:1), the product **9^{Mes}** was obtained as a colorless solid. Yield: 0.151 g (0.157 mmol, 56%).

Single crystals suitable for X-ray diffraction were grown by slow evaporation of a solution of **9^{Mes}** in CH_3CN.

^{1}H NMR (500.2 MHz, $CDCl_3$): δ = 7.95 (s, 3H, H-1), 7.91 (dd, $^3J_{HH}$ = 7.7 Hz, $^4J_{HH}$ = 1.8 Hz, 6H, H-4), 7.78 (ddd, $^3J_{HH}$ = 8.6 Hz, $^3J_{HH}$ = 7.0 Hz, $^4J_{HH}$ = 1.8 Hz, 6H, H-6), 7.38 (br d, $^3J_{HH}$ = 8.6 Hz, 6H, H-7), 7.20 (ddd, $^3J_{HH}$ = 7.7 Hz, $^3J_{HH}$ = 7.0 Hz, $^4J_{HH}$ = 0.9 Hz, 6H, H-5), 6.96 (s, 6H, Mes-CH-*m*), 2.41 (s, 9H, Mes-CH_3-*p*), 1.97 (s, 18H, Mes-CH_3-*o*).

^{13}C{^{1}H} NMR (125.8 MHz, $CDCl_3$): δ = 146.9 (C-2), 146.3 (C-8), 139.5 (br, Mes-C-*i*), 139.4 (Mes-C-*o*), 137.8 (C-4), 136.8 (Mes-C-*p*), 134.8 (C-1), 133.5 (C-6), 127.1 (Mes-CH-*m*), 126.4 (br, C-3), 120.6 (C-5), 116.2 (C-7), 23.3 (Mes-CH_3-*o*), 21.4 (Mes-CH_3-*p*).

^{11}B NMR (160.5 MHz, $CDCl_3$): δ = n.o.

HRMS (MALDI) *m/z*: $[M]^{\bullet+}$ calculated for $[C_{69}H_{60}B_3N_3]^{\bullet+}$: 963.5061, found: 963.5096.

1.10. Synthesis of 1,3,5-$(Ph_2N)_3C_6H_3$

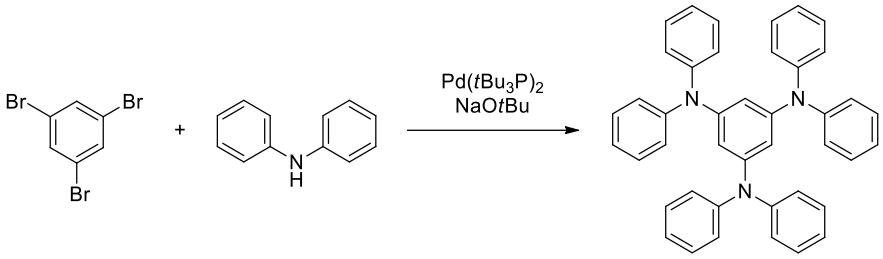

A microwave vial was charged with 1,3,5-tribromobenzene (0.123 g, 0.391 mmol), diphenylamine (0.200 g, 1.18 mmol), Pd(tBu$_3$P)$_2$ (0.030 g, 0.059 mmol), and NaOtBu (0.236 g, 2.46 mmol), closed with a septum cap, evacuated, and re-filled with argon. After the addition of degassed toluene (5 mL), the mixture was heated to 170 °C in a microwave reactor for 1 h. The reaction mixture was cooled to room temperature and filtered through a short plug of neutral Al_2O_3 using C_6H_6 as the eluent. All volatiles were removed from the filtrate under reduced pressure and the solid residue was washed with *n*hexane (4 x 3 mL) to afford 1,3,5-$(Ph_2N)_3C_6H_3$ as a colorless solid. Yield: 0.146 g (0.252 mmol, 64%).

The reported ^{1}H NMR shift values are consistent with literature data.[S8]

^{1}H NMR (400.1 MHz, $CDCl_3$): δ = 7.18–7.13 (m, 12H), 7.04–7.01 (m, 12H), 6.93–6.89 (m, 6H), 6.42 (s, 3H).

1.11. Investigation of the rearrangement reaction of 3^{Mes}

1.11.1. Demesitylation of 3^{Mes} with BBr_3

3^{Mes} (10.2 mg, 15.3 µmol) was dissolved in C_6D_6 (0.5 mL) in an NMR tube. After the addition of BBr_3 (0.21 M in C_6D_6, 0.08 mL, 0.02 mmol), the NMR tube was flame-sealed under vacuum and subsequently heated between 100 °C and 180 °C in an oven. The reaction was monitored by NMR spectroscopy. Before heating, the ^{1}H NMR spectrum showed mainly signals of unreacted **3^{Mes}** (Figure S1a). After heating to 100 °C for 40 h, the ^{1}H NMR spectrum indicated the presence of three species: small amounts of still unconsumed starting material and two new compounds. While most resonances in the aromatic region of the ^{1}H NMR spectrum overlapped with other signals (which impeded a detailed analysis), the strongly upfield-shifted resonances of H-1 remained fully resolved; the same applied for the Mes-CH_3 resonances. An analysis of the corresponding integral values indicated that the two new products originated from single (**$3^{Br,Mes}$**, labeled in yellow) and double Mes/Br-exchange (**3^{Br}**, labeled in blue) on the starting material (Figure S1b). This result is in line with the observation that further heating to 180 °C led to almost complete consumption of the starting material and of **$3^{Br,Mes}$**, mainly giving the doubly demesitylated species **3^{Br}** (Figure S1c). The by-product of this demesitylation is Mes(H/D).

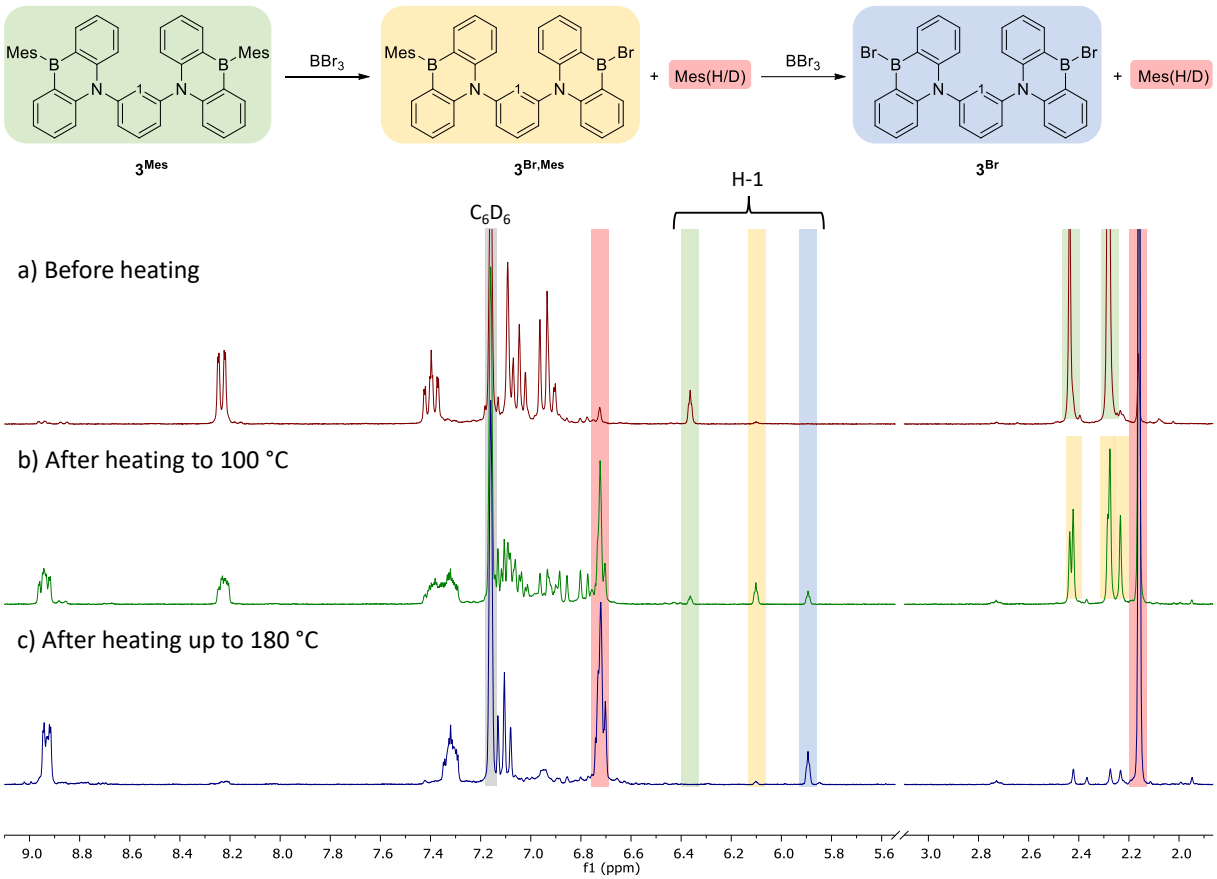

Figure S1. ^{1}H NMR spectra (300.0 MHz, C_6D_6) of the reaction mixture of **3^{Mes}** and BBr_3 (approx. 1 equiv) in C_6D_6 (a) before heating, (b) after heating to 100 °C for 40 h, and (c) after further heating to 120 °C for 48 h, 140 °C for 30 h, and 180 °C for 32 h.

Note: We did not isolate the product of this NMR experiment. However, its ^{1}H NMR spectrum compares well with the ^{1}H NMR spectrum of the reaction mixture of **1** with BBr_3 at room temperature, which should give the same product through Si/B-exchange (Figure S2).

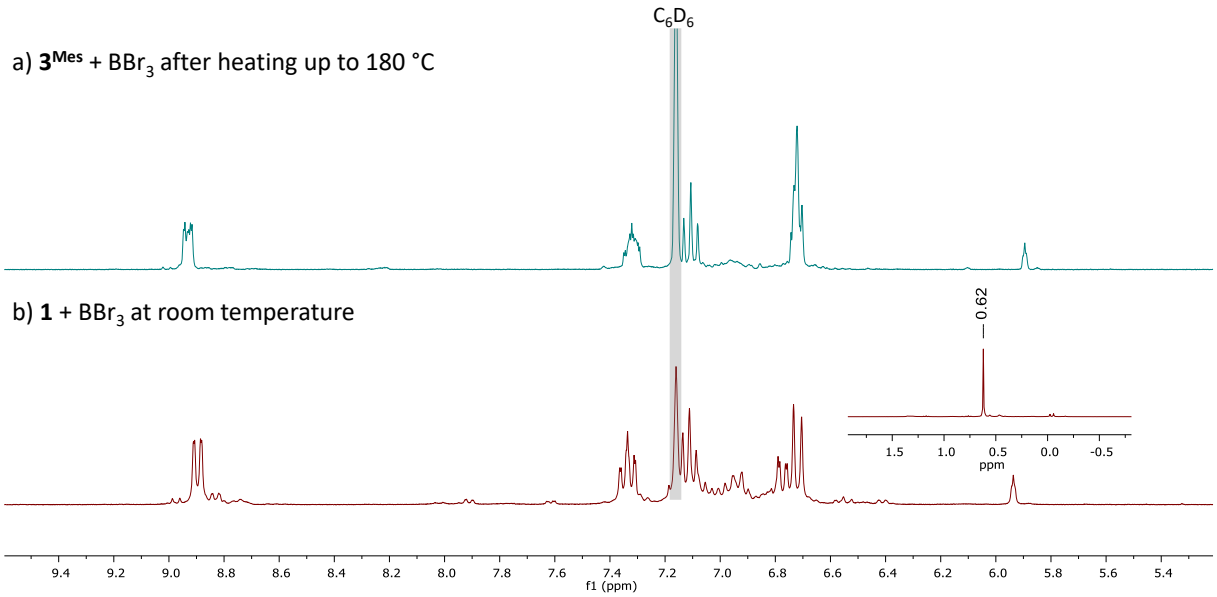

Figure S2. Aromatic regions of the ^{1}H NMR spectra (300.0 MHz, C_6D_6) of the reactions mixtures of (a) $\mathbf{3^{Mes}}$ and BBr_3 (approx. 1 equiv) after heating up to 180 °C and (b) **1** and BBr_3 (approx. 13 equiv) after storing at room temperature. The inset shows the signal of Me_2SiBr_2 that forms during the Si/B-exchange reaction.

1.11.2. Deuteration and rearrangement of $\mathbf{3^{Mes}}$ with BBr_3 in C_6D_6

$\mathbf{3^{Mes}}$ (31.6 mg, 47.3 µmol) was dissolved in C_6D_6 (0.5 mL) in an NMR tube. After the addition of BBr_3 (0.06 mL, 0.2 g, 0.6 mmol), the NMR tube was flame-sealed under vacuum and heated to 180 °C in an oven for 53 h. The NMR tube was cooled to room temperature, whereupon a red precipitate formed. The NMR tube was opened, the solid was separated from the mother liquor, and dried under reduced pressure. A portion of the solid (16 mg) and Mes_2Zn (0.023 g, 0.076 mmol) were suspended in C_6D_6 (0.5 mL) in an NMR tube, which was then flame-sealed under vacuum. After heating to 50 °C in an oven for 30 h, the NMR tube was opened and all volatiles were removed under reduced pressure. The residue was subjected to column chromatography (silica gel, C_6H_{12}:$CHCl_3$ = 1:1) to obtain a yellow solid.

The ^{1}H NMR spectrum of the product contained only singlet resonances in the aromatic region. A comparison of this spectrum with the spectrum of $\mathbf{2^{Mes}}$ showed that the singlets had the same chemical shift values as the signals for H-4,6,8,12 and for Mes-CH-*m* of $\mathbf{2^{Mes}}$ (Figure S3). We propose a partial deuteration of $\mathbf{2^{Mes}}$ as an explanation of this phenomenon ($^{3}J_{DH}$ << $^{3}J_{HH}$ in arenes[S10]; acid-mediated deuterations of arenes with C_6D_6 as the deuterium source have previously been published[S11]): The D atoms are apparently mainly attached to the C atoms *ortho* and *para* to the N atoms, but the integral ratios between the signals indicate that deuteration is not completely selective and to some extent also occurs at the *meta* positions. The effect of deuteration can be seen in the ^{13}C{^{1}H} NMR spectrum as well, as the resonances of D-bonded C atoms are broadened/reduced in intensity (Figure S4). We also attempted to perform ^{2}H NMR spectroscopy for further analysis of the sample. However, only one multiplet with broadened signals in the aromatic region could be observed (Figure S5).

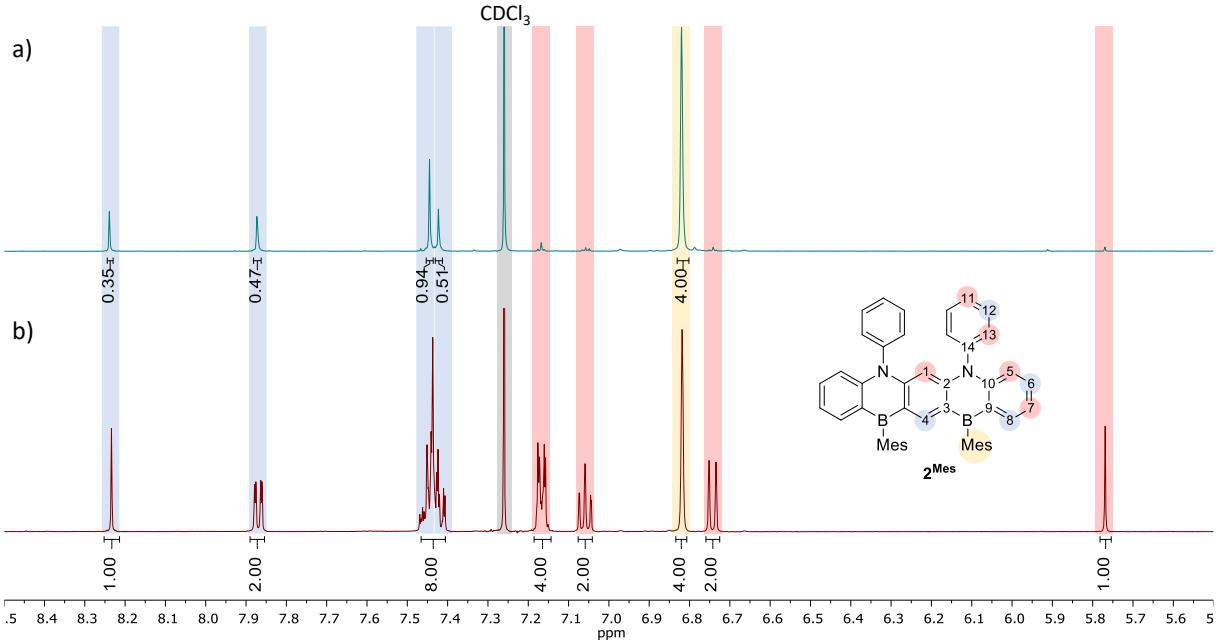

Figure S3. Aromatic regions of the ^{1}H NMR spectra (500.2 MHz, $CDCl_3$) of (a) the product of the reaction of **3**^{Mes} with BBr_3 (approx. 13 equiv)/Mes_2Zn (exc.) in C_6D_6 and of (b) **2**^{Mes}. Signals of partly deuterated positions are marked in blue; signals of almost completely deuterated positions are marked in red. The aromatic signal of non-deuterated Mes is marked in yellow.

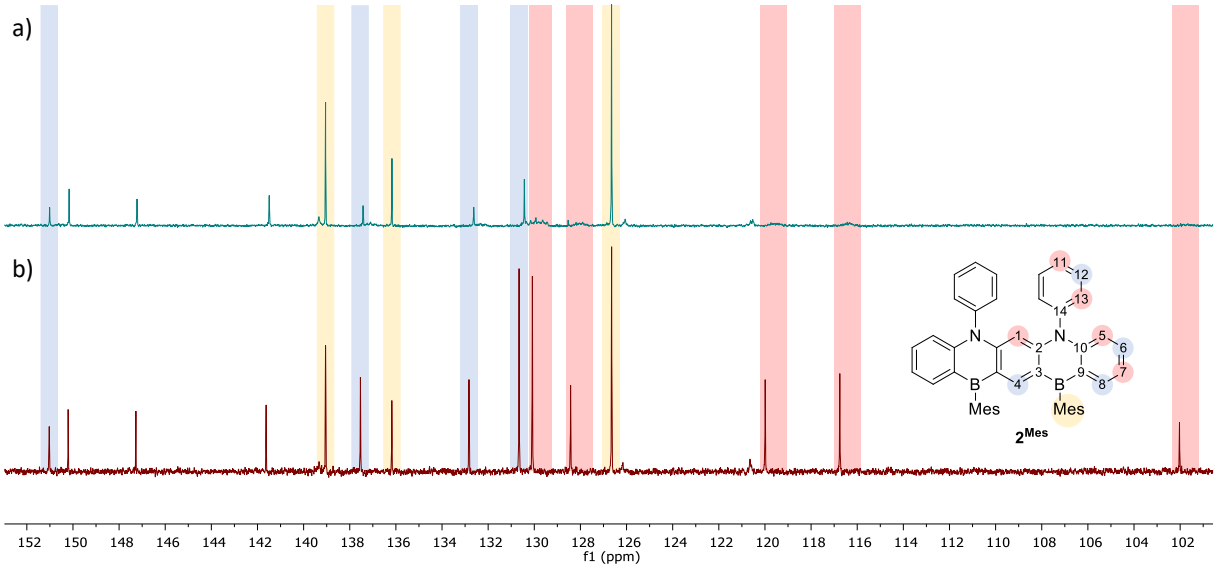

Figure S4. Aromatic regions of the $^{13}C\{^{1}H\}$ NMR spectra (125.8 MHz, $CDCl_3$) of (a) the product of the reaction of **3**^{Mes} with BBr_3 (approx. 13 equiv)/Mes_2Zn (exc.) in C_6D_6 and of (b) **2**^{Mes}. Signals of partly deuterated positions are marked in blue; signals of almost completely deuterated positions are marked in red. The aromatic signals of non-deuterated Mes are marked in yellow. Signals of B- or N-bonded C atoms are not marked.

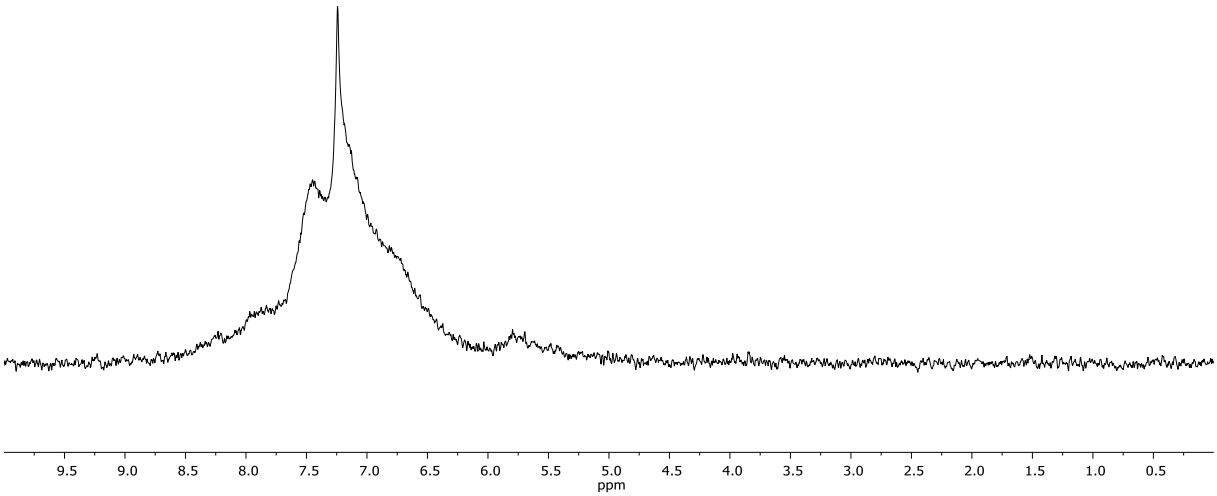

Figure S5. ^{2}H NMR spectrum (76.8 MHz, $CHCl_3$) of the product of the reaction of **3^{Mes}** with BBr_3 (approx. 13 equiv)/Mes_2Zn (exc.) in C_6D_6.

Deuteration could already be observed in the ^{1}H NMR spectrum of the red precipitate formed in the reaction of **3^{Mes}** with BBr_3 in C_6D_6 at 180 °C (Figure S6; the same reaction in C_6H_6 gave **2^{Br}**, cf. section 1.4), which shows that H/D-exchange occurs already at this step.

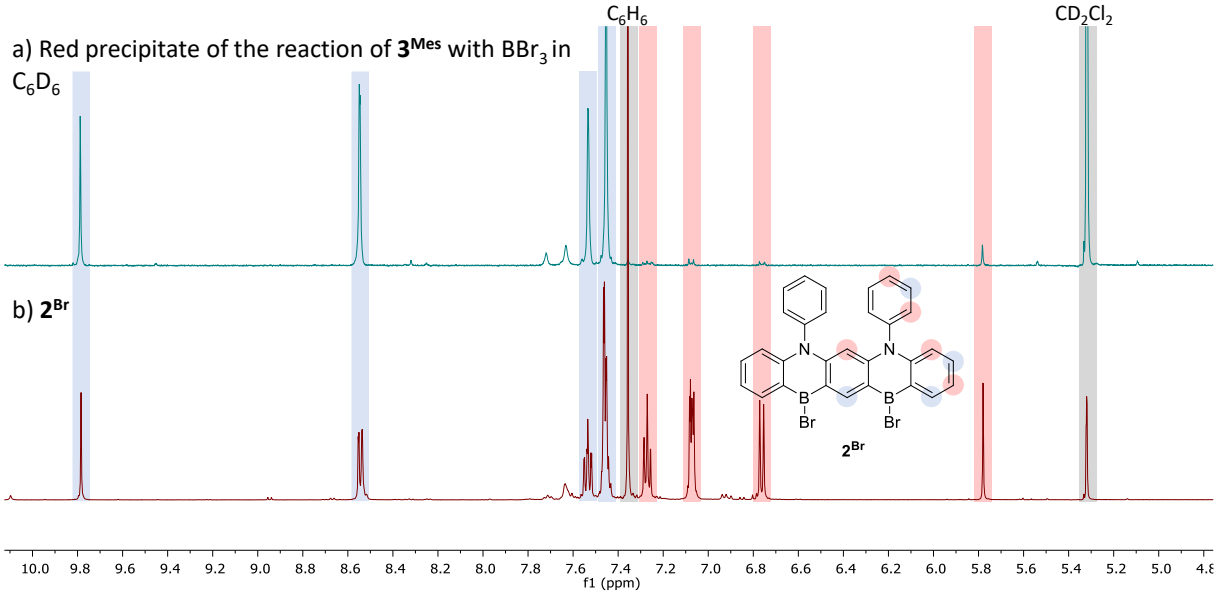

Figure S6. Aromatic regions of the ^{1}H NMR spectra (CD_2Cl_2) of (a) the red solid formed in the reaction of **3^{Mes}** with BBr_3 (approx. 13 equiv) in C_6D_6 at 180 °C (400.1 MHz) and (b) **2^{Br}** (500.2 MHz). Signals of partly deuterated positions are marked in blue; signals of almost completely deuterated positions are marked in red.

1.12. Investigation of the rearrangement reaction of 5

1.12.1. Reaction of 5 with BBr_3

In contrast to the reactions of $\mathbf{3}^{Mes}$ or **1** with BBr_3 in C_6H_6 at 180 °C (see sections 1.4 and 1.5), where the red precipitate formed consisted of only one species, the reaction of **5** with BBr_3 in C_6H_6 at 180 °C (see section 1.7 and 1.8) produced a red precipitate that showed signals of more than one species in the ^{1}H NMR spectrum. After mesitylation of this precipitate, four different main products could be identified in the ^{1}H NMR spectrum: **6**, **7**, **8**, and $\mathbf{2}^{Mes}$. Since the signals of **6** and **7** were absent in a ^{1}H NMR spectrum of the red precipitate recorded prior to mesitylation (Figure S7), these products are likely formed during the mesitylation step (or the *i*PrOH quench; see section 1.8). In contrast, $\mathbf{2}^{Br}$ apparently is a constituent of the red precipitate (Figure S7), showing that C–N-bond cleavage must have happened already at this step.

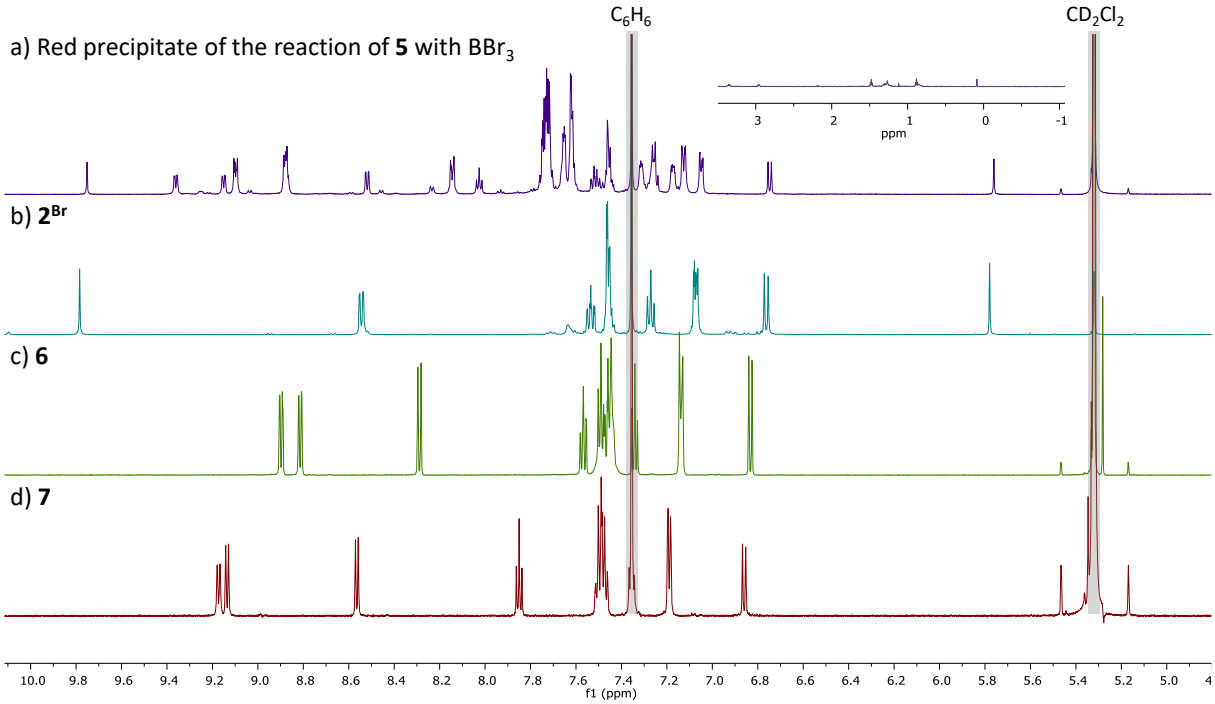

Figure S7. Aromatic regions of the ^{1}H NMR spectra (CD_2Cl_2) of (a) the red precipitate formed in the reaction of **5** with BBr_3 (approx. 28 equiv) in C_6H_6 at 180 °C (600.2 MHz; the inset shows the alkyl region), (b) $\mathbf{2}^{Br}$ (500.2 MHz), (c) **6** (600.2 MHz), and (d) **7** (600.2 MHz).

1.12.2. Borylation reaction of 1,3,5-$(Ph_2N)_3C_6H_3$ with BBr_3

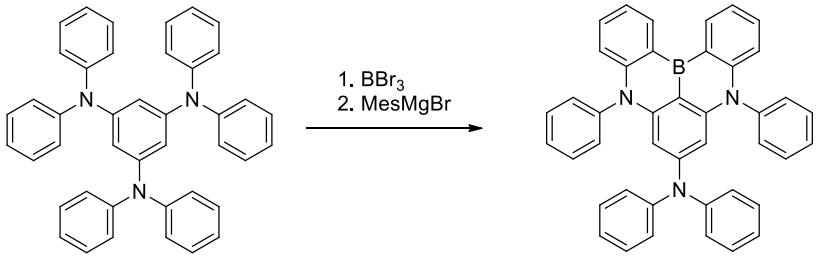

An NMR tube was charged with 1,3,5-$(Ph_2N)_3C_6H_3$ (15.6 mg, 26.9 µmol), BBr_3 (0.07 mL, 0.2 g, 0.7 mmol), and C_6H_6 (0.6 mL). The NMR tube was flame-sealed under vacuum and subsequently heated to 180 °C in an oven for 14 h. After cooling to room temperature, the NMR tube was opened, and the liquid was removed *via* syringe. The remaining solid was washed with *n*pentane (2 x 0.2 mL) and all volatiles were removed under reduced pressure. The solid was transferred to a Schlenk tube and suspended in toluene (3 mL). After cooling the suspension to –78 °C, MesMgBr (1.39 M in THF, 0.12 mL, 0.17 mmol) was added dropwise with stirring. The reaction mixture was allowed to warm to room temperature and stirred overnight. After removal of all volatiles, the resulting solid was analyzed *via* NMR spectroscopy. The ^{1}H NMR spectrum of the crude product mixture showed signals of the monoborylated system[S12] (see Scheme above) as the main product. Even when 1,3,5-$(Ph_2N)_3C_6H_3$ was heated to 180 °C with BBr_3 for a prolonged period (up to 14 d) and then mesitylated, the crude product mixture contained no **6**, **7**, or **8** besides the monoborylated product.

2. Plots of NMR spectra

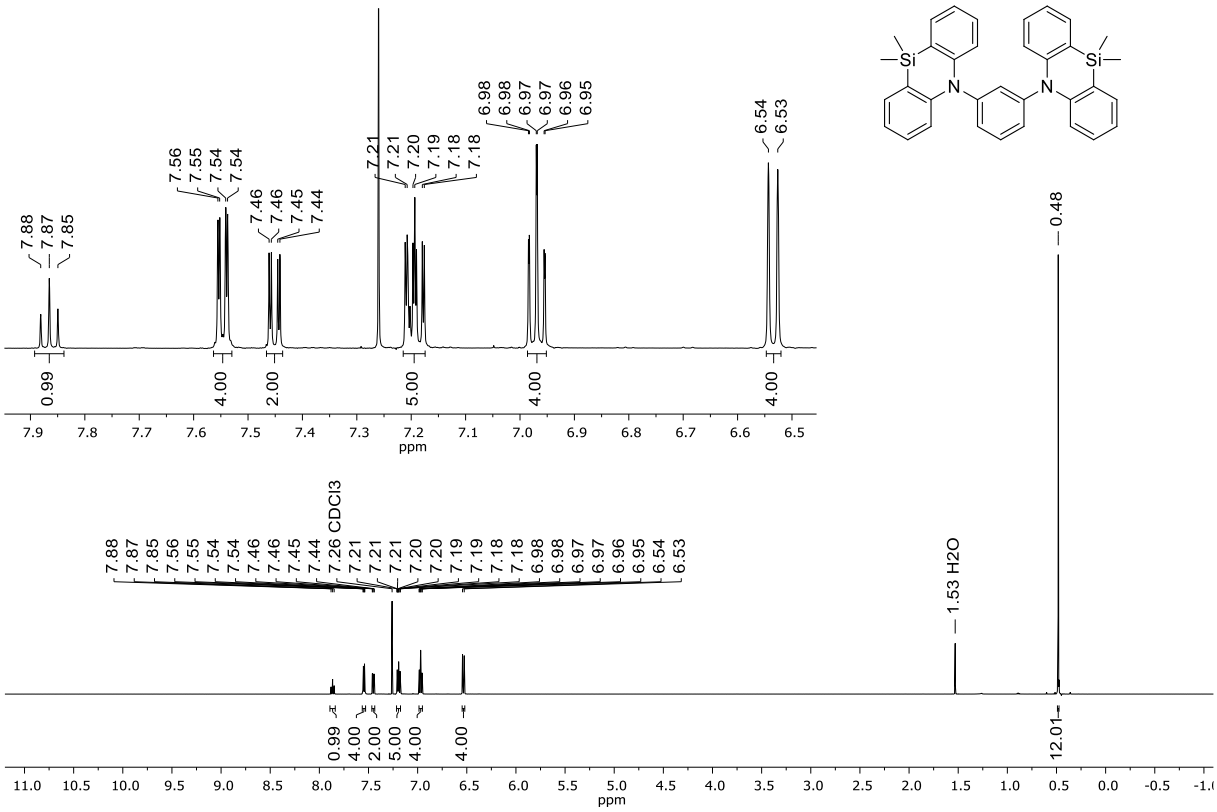

Figure S8. ^{1}H NMR spectrum (500.2 MHz, $CDCl_3$) of **1**.

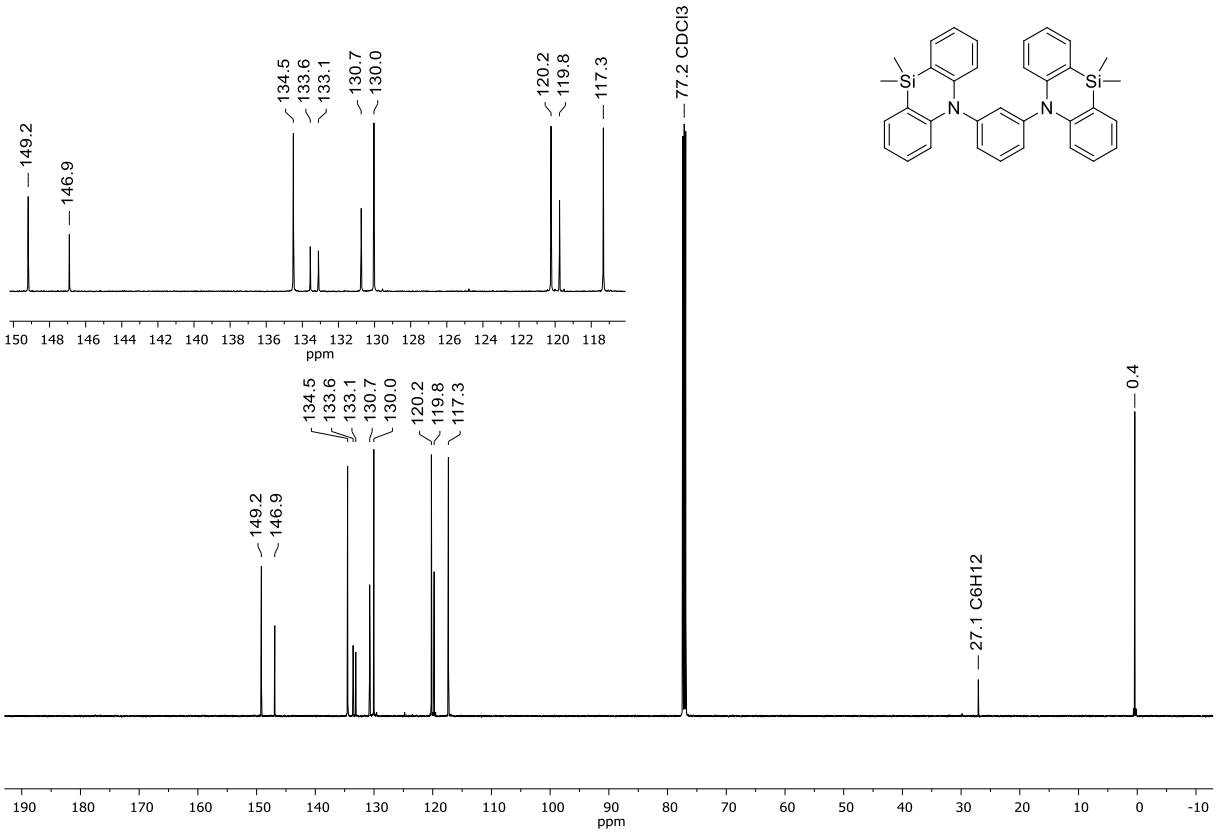

Figure S9. $^{13}C\{^{1}H\}$ NMR spectrum (125.8 MHz, $CDCl_3$) of **1**.

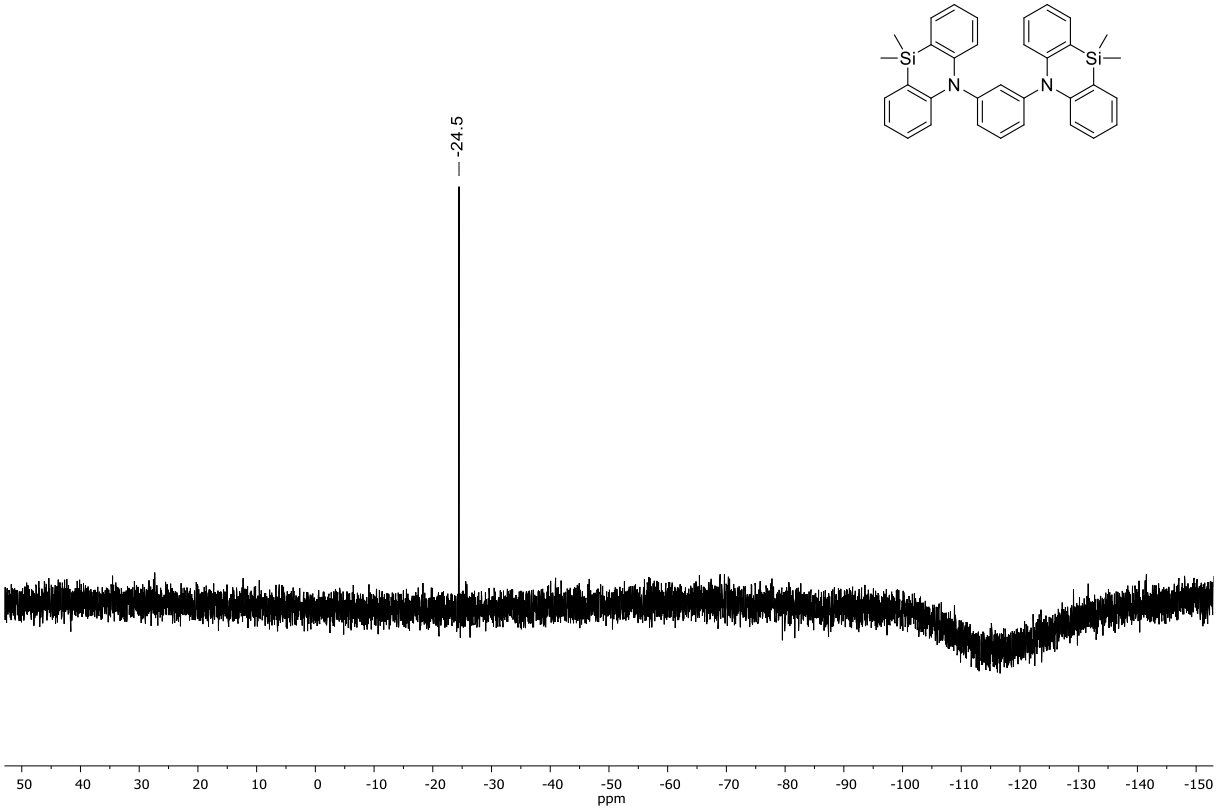

Figure S10. $^{29}Si\{^{1}H\}$ NMR spectrum (99.4 MHz, $CDCl_3$) of **1**.

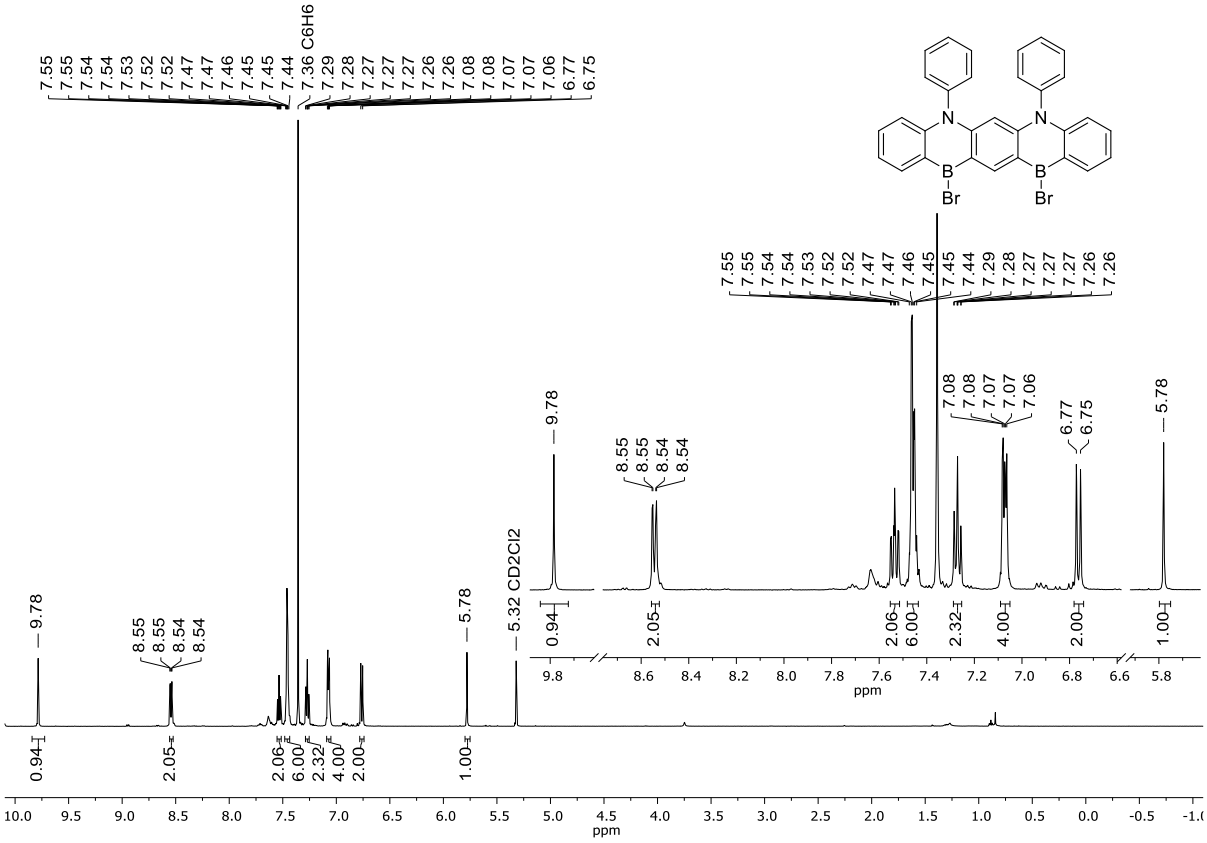

Figure S11. ^{1}H NMR spectrum (500.2 MHz, CD_2Cl_2) of **2^{Br}**.

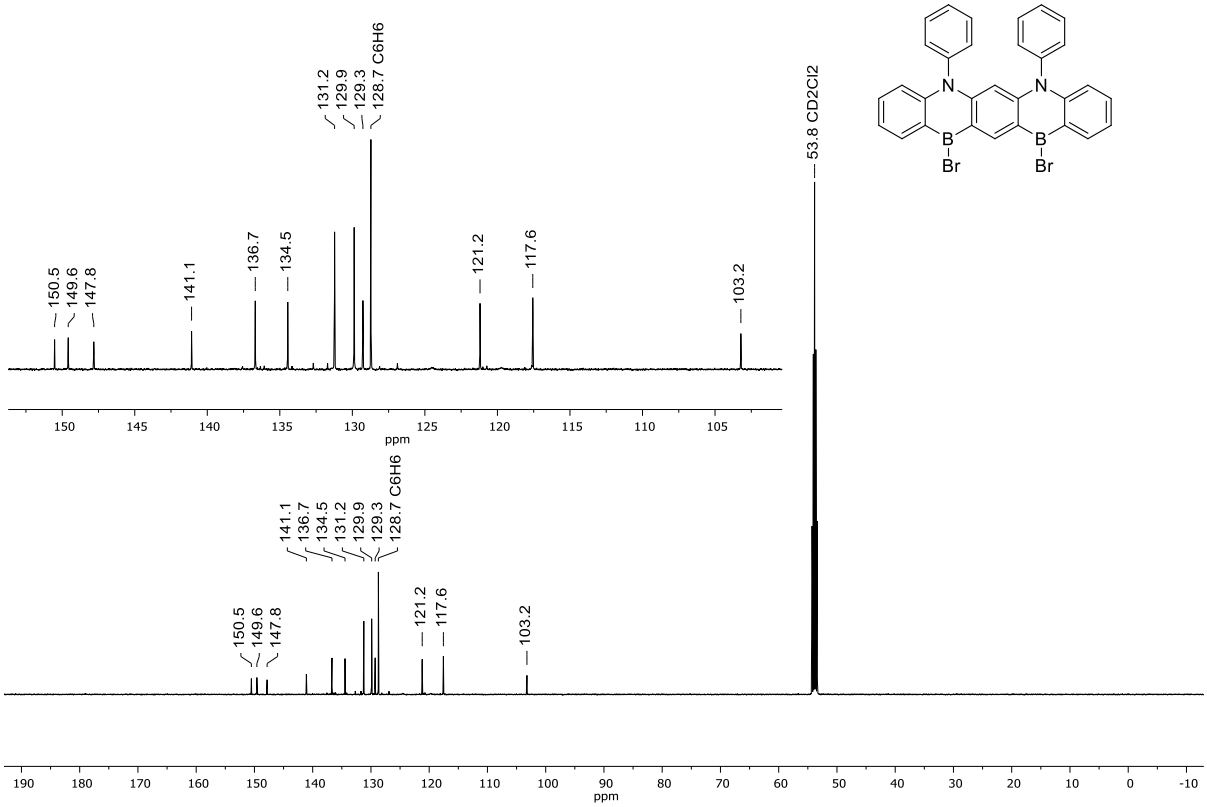

Figure S12. $^{13}C\{^{1}H\}$ NMR spectrum (125.8 MHz, CD_2Cl_2) of **2^{Br}**.

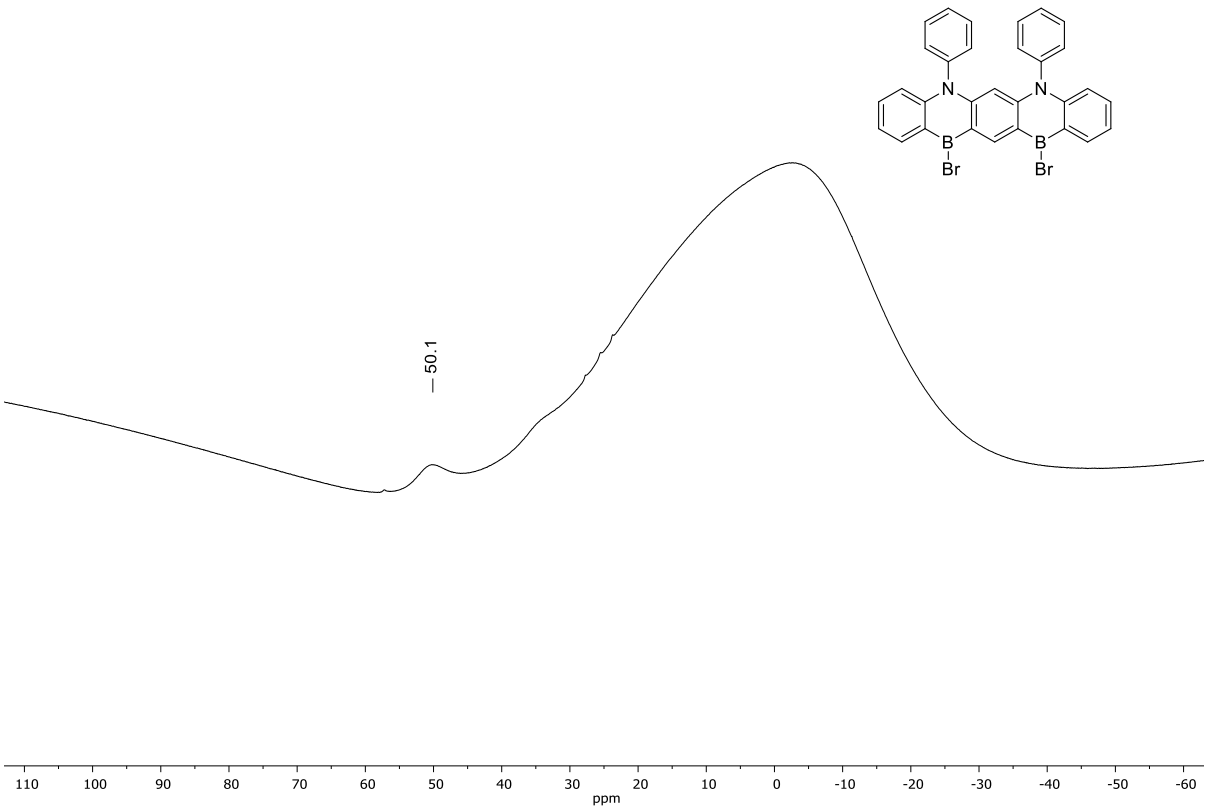

Figure S13. ^{11}B NMR spectrum (160.5 MHz, CD_2Cl_2) of **2^{Br}**.

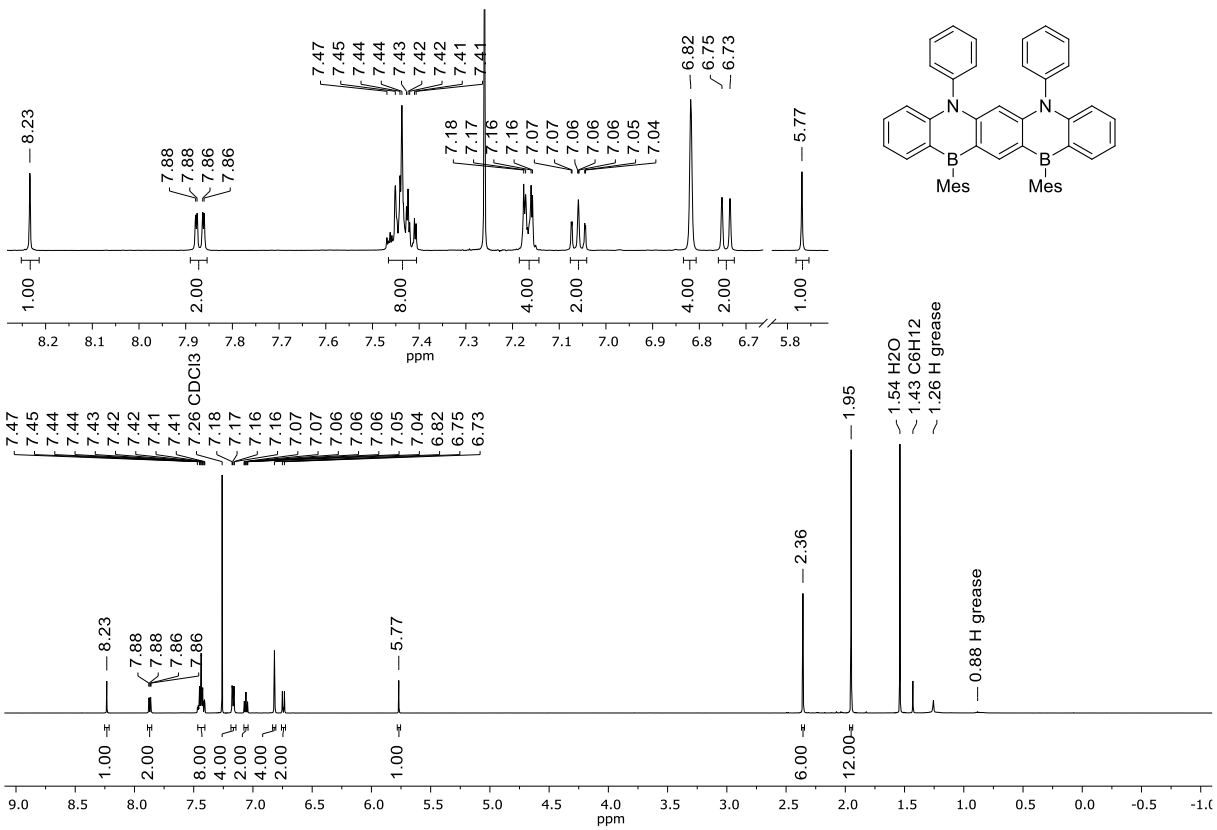

Figure S14. ^{1}H NMR spectrum (500.2 MHz, $CDCl_3$) of **2^{Mes}**.

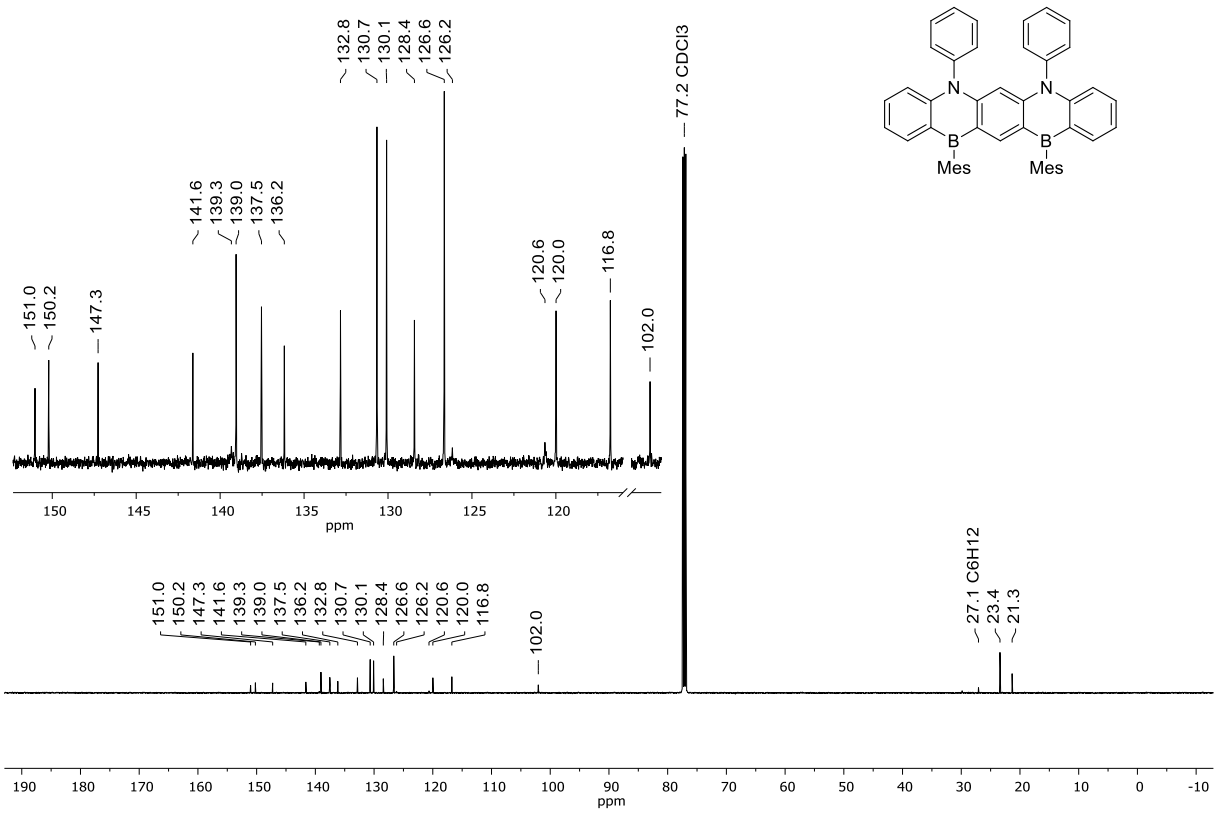

Figure S15. $^{13}C\{^{1}H\}$ NMR spectrum (125.8 MHz, $CDCl_3$) of **2^{Mes}**.

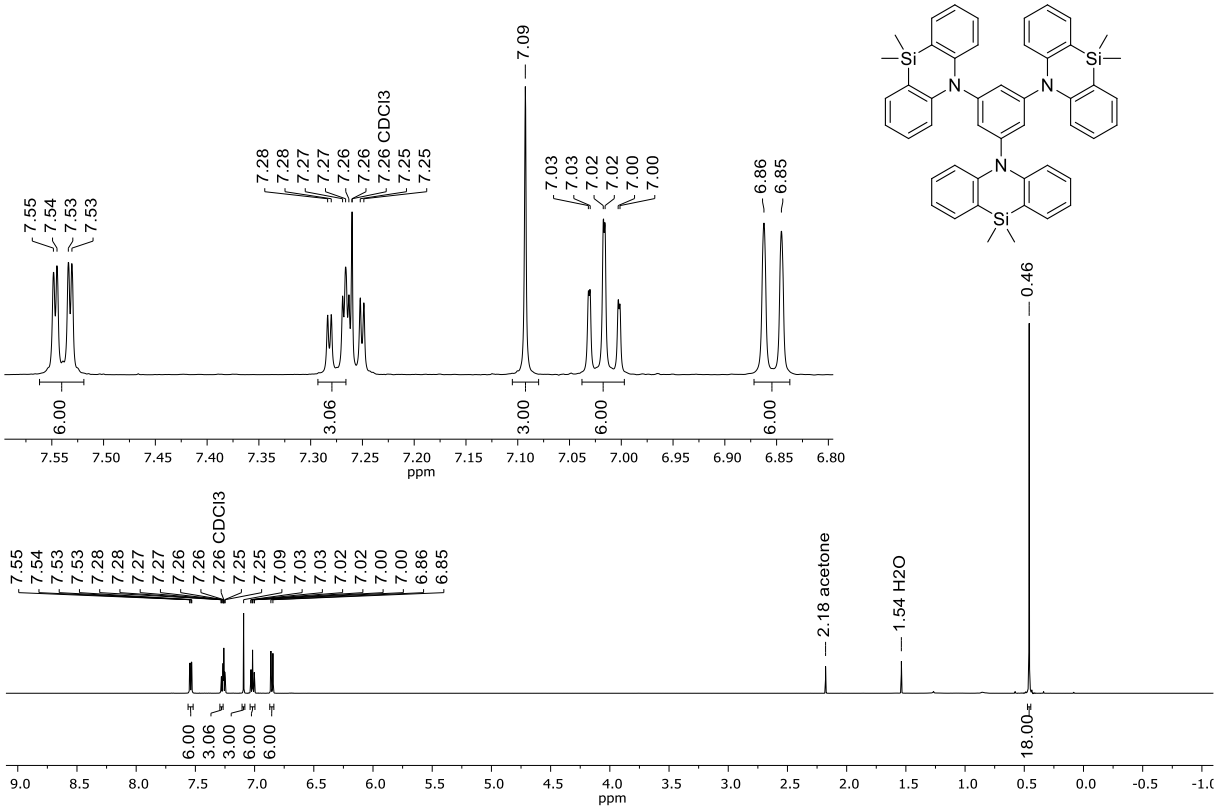

Figure S16. ^{1}H NMR spectrum (500.2 MHz, $CDCl_3$) of **5**. *Note*: The signal at 7.27 ppm partly overlaps with the solvent signal, which is why the integral only covers half of the signal.

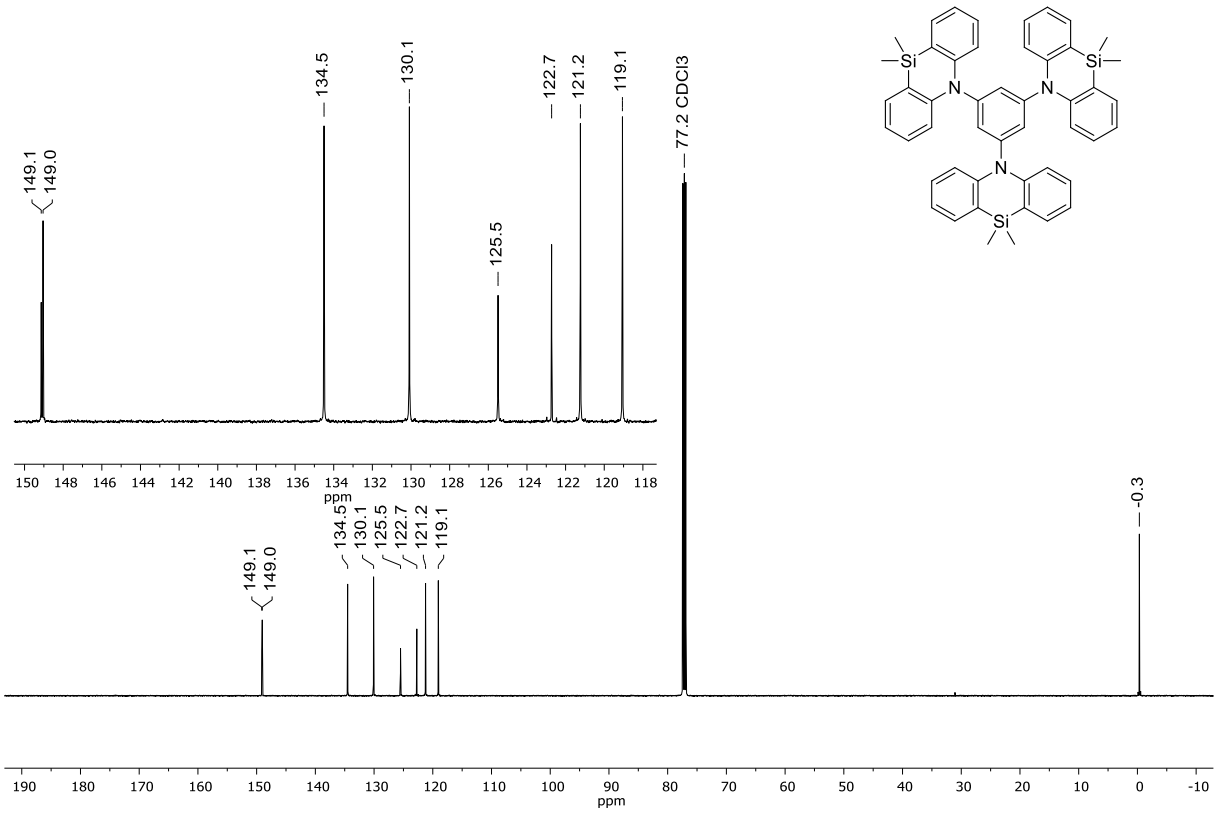

Figure S17. $^{13}C\{^{1}H\}$ NMR spectrum (125.8 MHz, $CDCl_3$) of **5**.

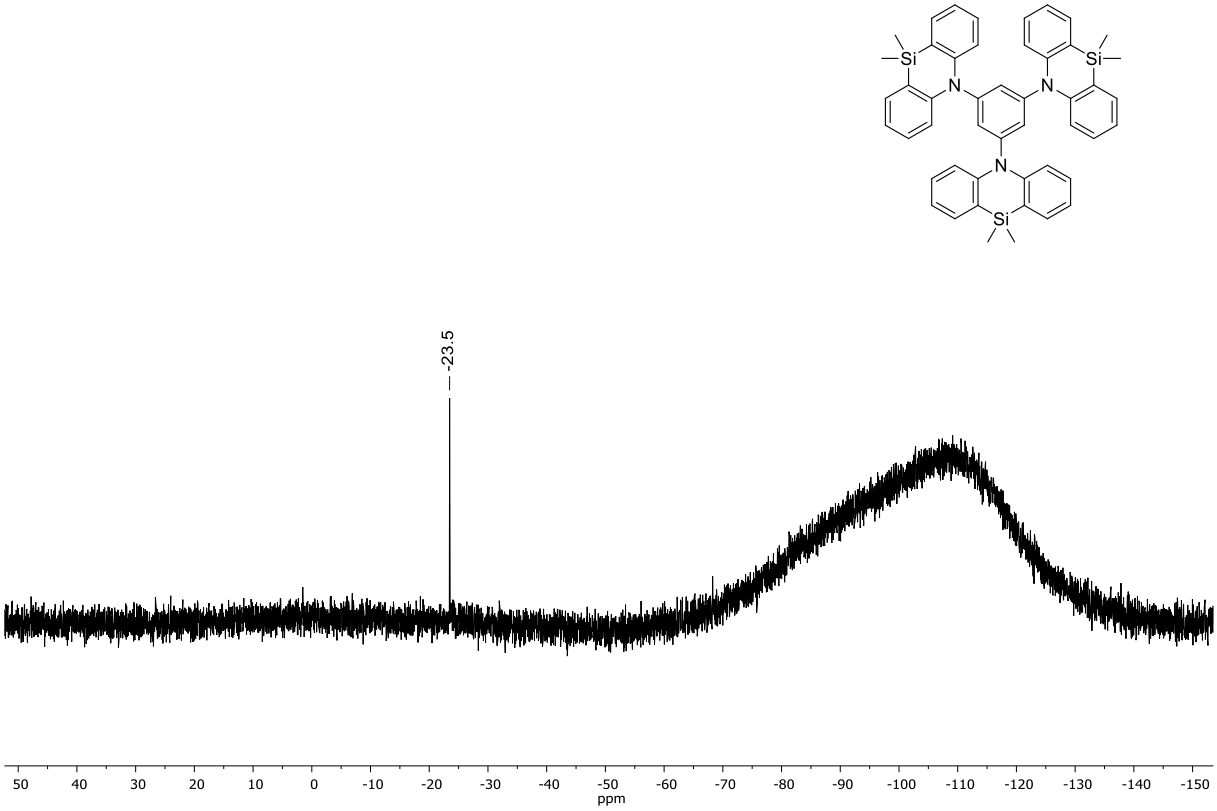

Figure S18. $^{29}Si\{^{1}H\}$ NMR spectrum (99.4 MHz, $CDCl_3$) of **5**.

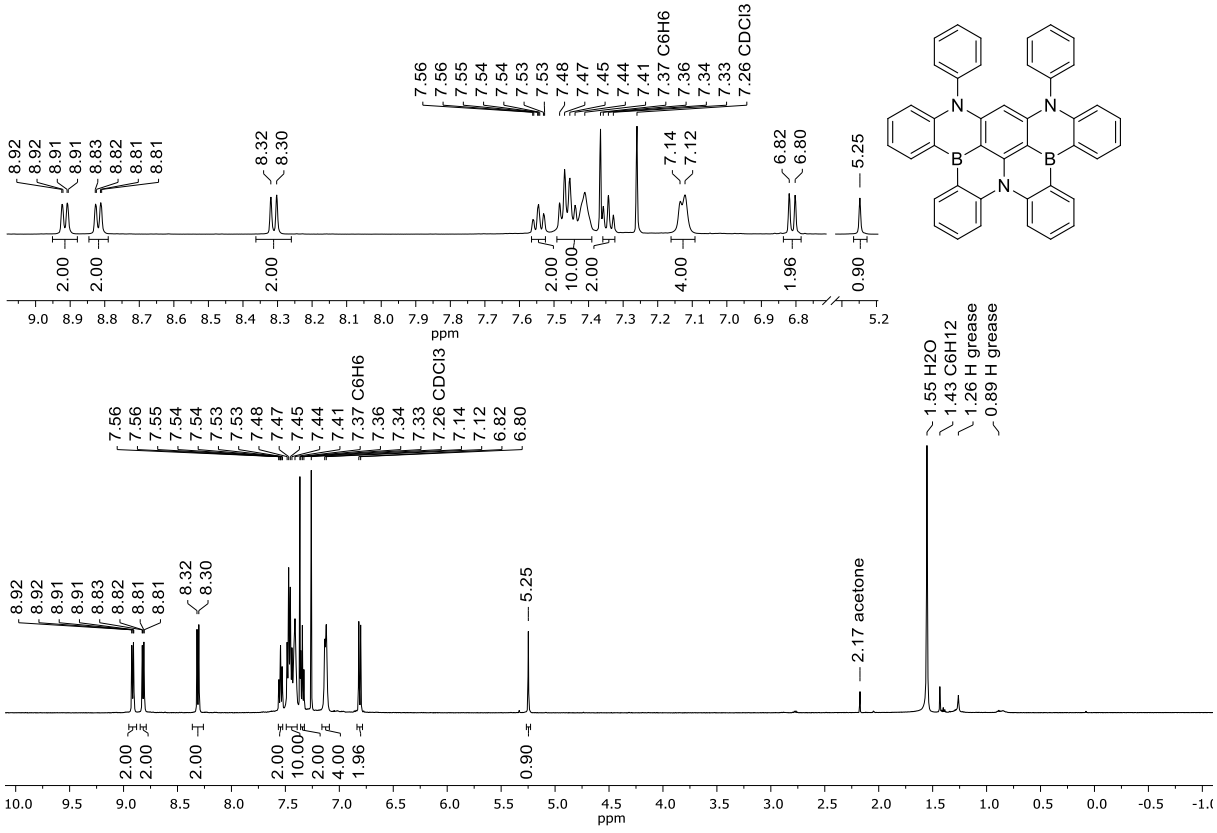

Figure S19. ^{1}H NMR spectrum (500.2 MHz, $CDCl_3$) of **6**.

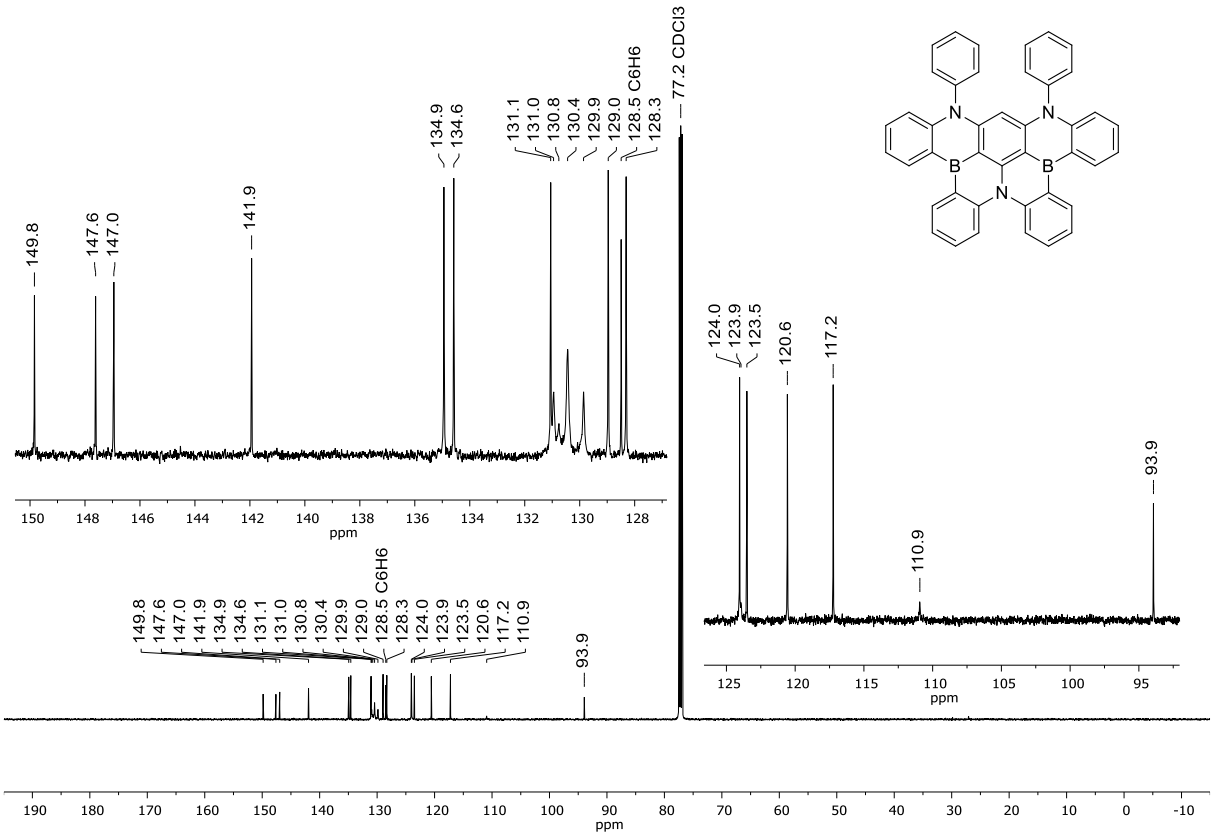

Figure S20. $^{13}C\{^{1}H\}$ NMR spectrum (125.8 MHz, $CDCl_3$) of **6**.

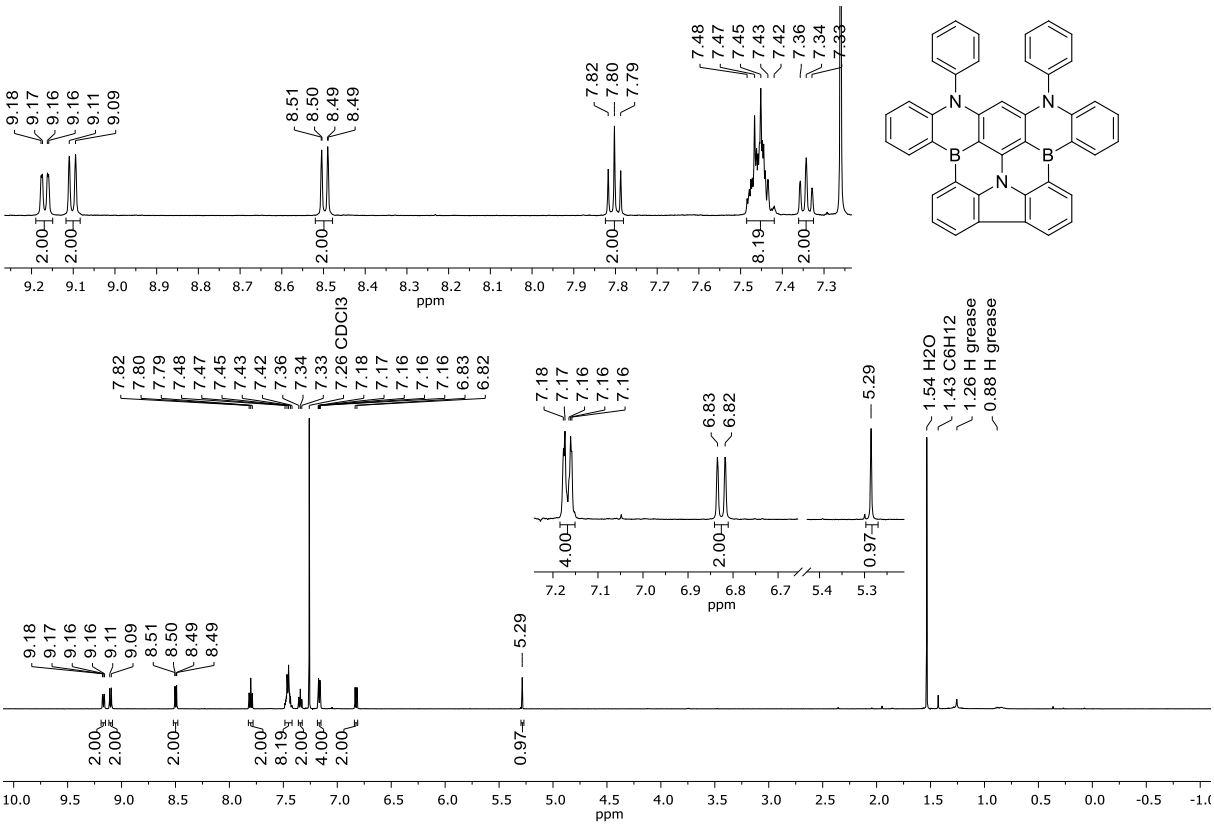

Figure S21. ^{1}H NMR spectrum (500.2 MHz, $CDCl_3$) of **7**.

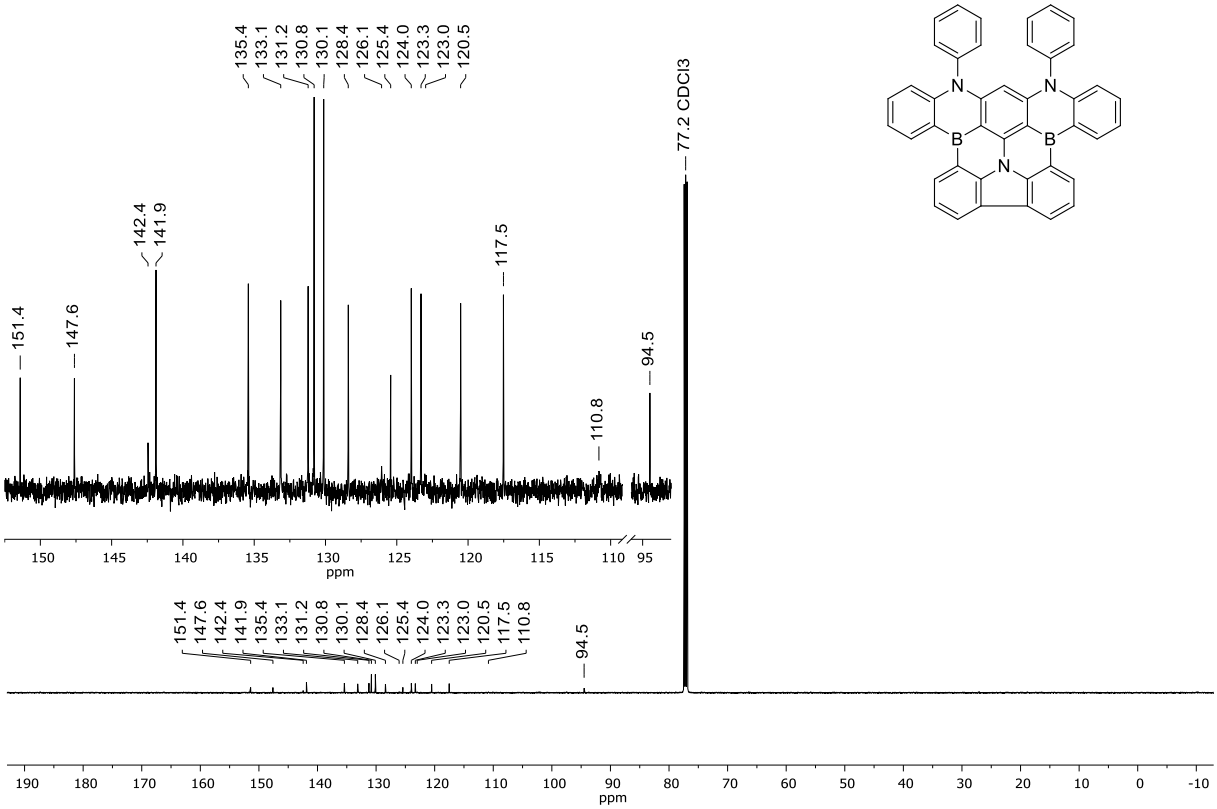

Figure S22. $^{13}C\{^{1}H\}$ NMR spectrum (125.8 MHz, $CDCl_3$) of **7**.

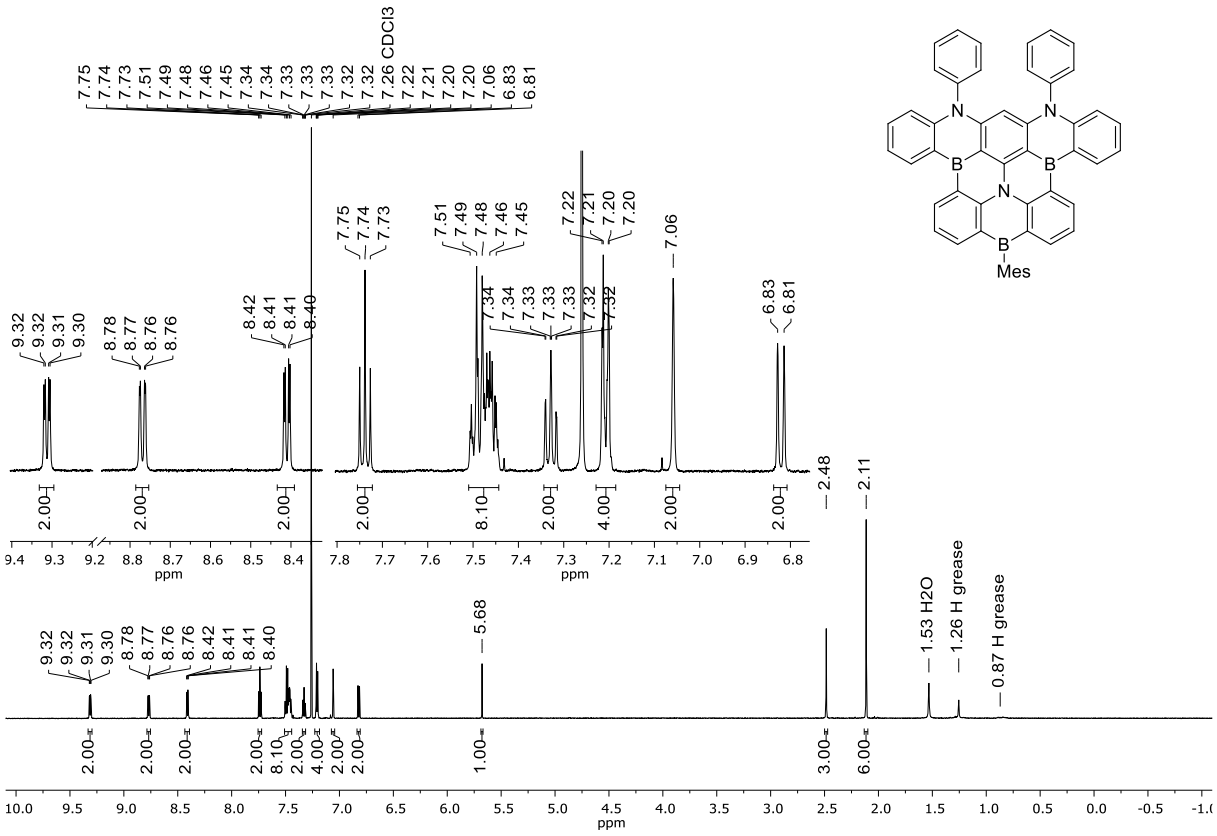

Figure S23. ^{1}H NMR spectrum (600.2 MHz, $CDCl_3$) of **8**.

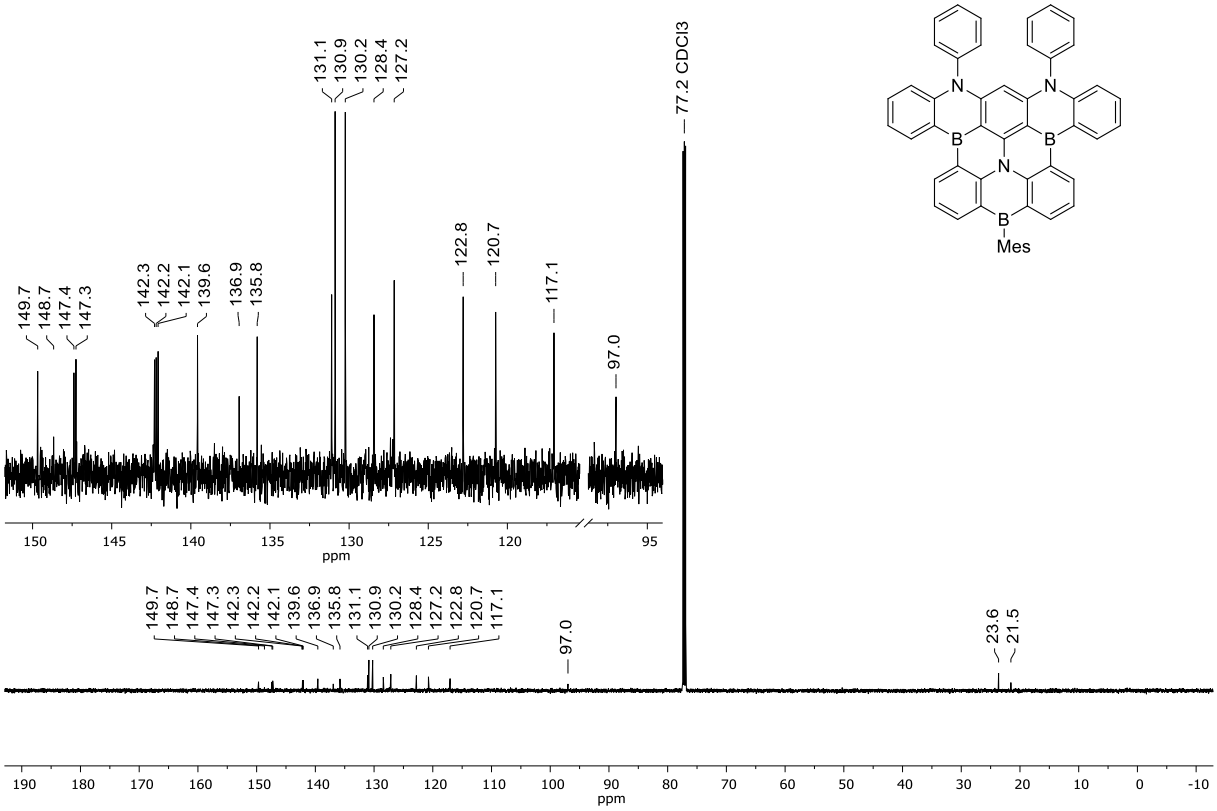

Figure S24. $^{13}C\{^{1}H\}$ NMR spectrum (150.9 MHz, $CDCl_3$) of **8**.

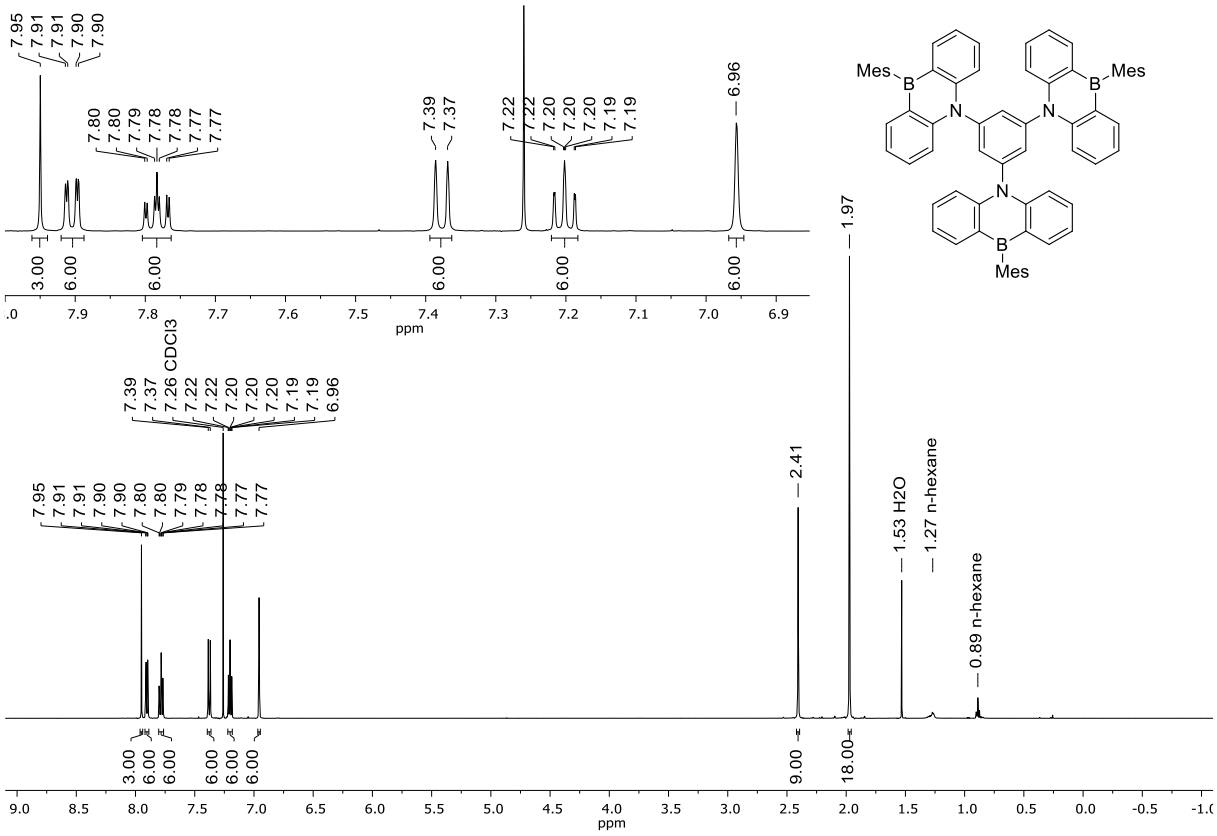

Figure S25. ^{1}H NMR spectrum (500.2 MHz, $CDCl_3$) of $\mathbf{9^{Mes}}$.

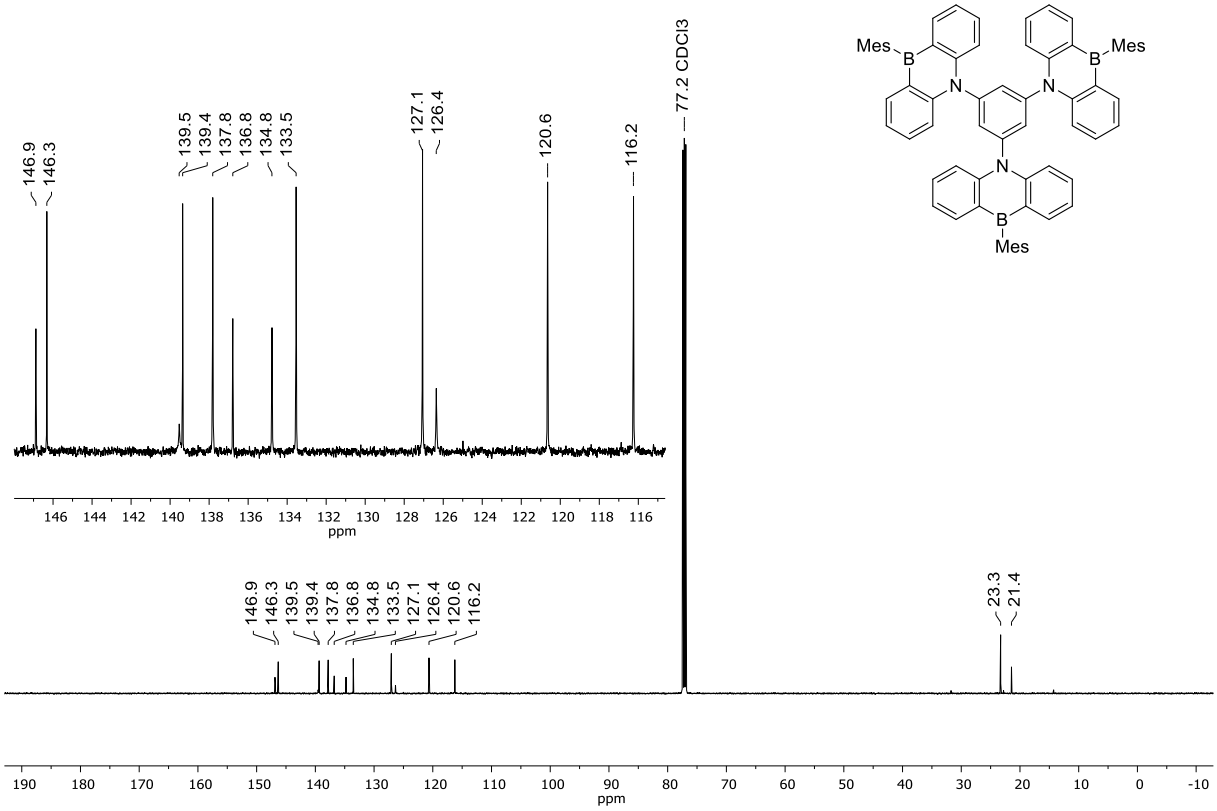

Figure S26. $^{13}C\{^{1}H\}$ NMR spectrum (125.8 MHz, $CDCl_3$) of $\mathbf{9^{Mes}}$.

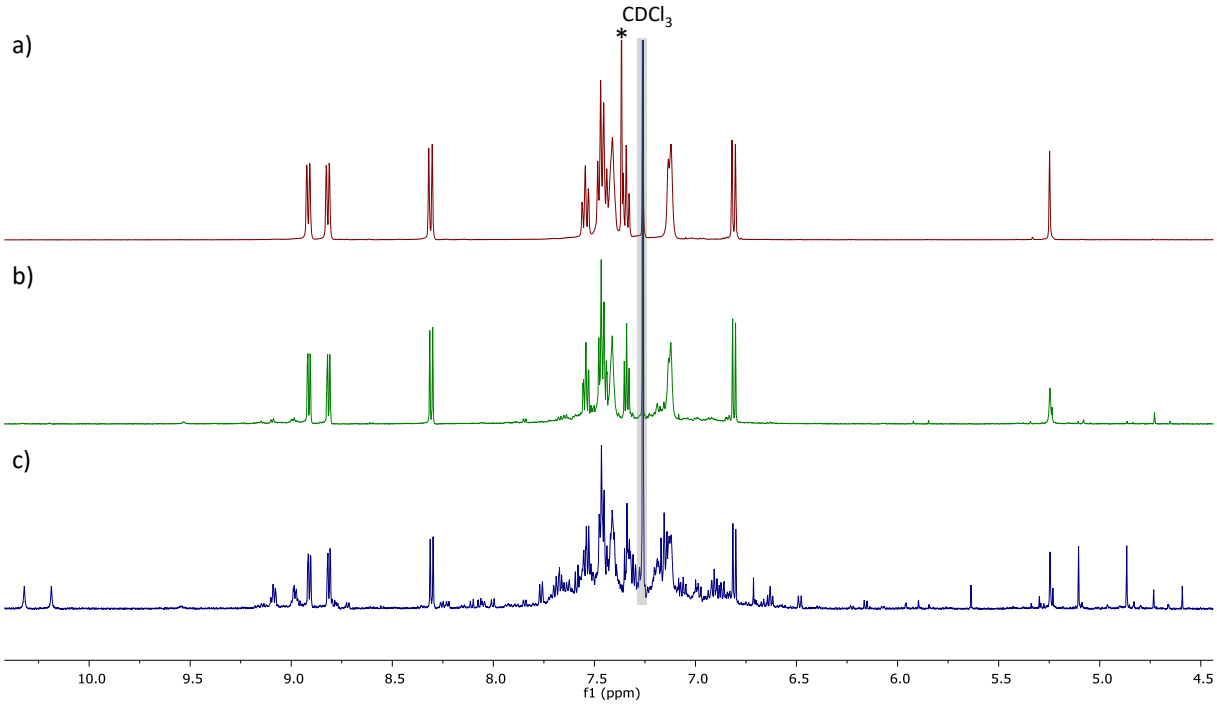

Figure S27. Aromatic regions of the ^{1}H NMR spectra ($CDCl_3$) of different samples of **6** to show the limited stability of this compound in $CHCl_3/CDCl_3$ under ambient conditions. The spectra were recorded: (a) after 30 min at room temperature (500.2 MHz), (b) after 1 month at room temperature (600.2 MHz), and (c) after **6** (1.6 mg) had been stored in $CHCl_3$ (5 mL; high dilution) for several hours, dried, and re-dissolved in $CDCl_3$ (0.5 mL; 600.2 MHz). *) C_6H_6.

3. Photophysical and electrochemical data

Table S1. Photophysical and electrochemical data of the compounds **1**, **2^{Mes}**, **5**, **6**, **7**, **8**, and **9^{Mes}**. Optical measurements were performed in C_6H_6, $CHCl_3$, THF, and/or on a PMMA layer; electrochemical measurements were performed in THF.

	Medium	λ_{abs} [nm] (ε [M^{-1} cm^{-1}])	λ_{onset}[a] [nm]	λ_{ex} [nm]	λ_{em}[b] [nm]	Φ_{PL}[c] [%]	Stokes shift[d] [cm^{-1}]	FWHM[e] [eV]	E_{HOMO}/ E_{LUMO}[f] [eV]	$E_{1/2}$[g]/ E_{onset}^{Red1}[g] [V]	E_G^{opt}[h] [eV]	τ_p[i] [ns]/ τ_d[i] [µs]
1	$CHCl_3$	292 (39300) 322* 335*	345	-	n.o.	-	-	-	-	-	3.59	-
	THF	-	-	-	-	-	-	-	-	n.o.	-	-
2^{Mes}	$CHCl_3$	325 (102000) 384 (10000) 418 (8800)	-	325	437	50	1040	0.18	-	-	-	-
	THF	324 383 419	437	325	440	66	1139	0.18	–5.42/ –2.58	–2.60/ –2.52	2.84	-
	PMMA	-	-	375	445	-	-	0.16	-	-	-	8.0/ n.o.
5	$CHCl_3$	292 (24500) 322*	346	-	n.o.	-	-	-	-	-	3.58	-
	THF	-	-	-	-	-	-	-	–5.56/ –1.98	–3.23/ –3.12	-	-
6	C_6H_6	353 (41900) 425 (26500)	-	325	442	35	905	0.18	-	-	-	-
	THF	350 424	440	325	447	18	1214	0.22	–5.43/ –2.61	–2.56/ –2.49	2.82	-
	PMMA	-	-	375	470	-	-	0.13	-	-	-	4.2/ 89
7	$CHCl_3$	312 (28700) 336 (31800) 369 (37300) 394 (7000) 413 (18800) 457 (9900)	-	369	478	67	961	0.17	-	-	-	-
	THF	311 335 368 393 413 456	476	369	479	84	1053	0.19	–5.43/ –2.82	–2.35/ –2.28	2.61	-
	PMMA	-	-	375	480	-	-	0.21	-	-	-	14.8/ 35

	Medium	λ_{abs} [nm] (ε [M^{-1} cm^{-1}])	λ_{onset}[a] [nm]	λ_{ex} [nm]	λ_{em}[b] [nm]	Φ_{PL}[c] [%]	Stokes shift[d] [cm^{-1}]	FWHM[e] [eV]	E_{HOMO}/ E_{LUMO}[f] [eV]	$E_{1/2}$[g]/ E_{onset}^{Red1}[g] [V]	E_G^{opt}[h] [eV]	τ_p[i] [ns]/ τ_d[i] [µs]
8	$CHCl_3$	306 (28000) 316 (30300) 345 (39700) 353 (38000) 371 (68700) 395 (8700) 460 (20100)	-	370	488	77	1247	0.19	-	-	-	-
	THF	304 315 344 353 370 394 461	485	370	493	84	1408	0.20	–5.53/ –2.97	–2.19/ –2.13	2.56	-
	PMMA	-	-	375	500	-	-	0.18	-	-	-	10.7/ 136
9^{Mes}	$CHCl_3$	371 (39500) 388 (69600)	-	368	398 415*	93	647	0.23	-	-	-	-
	THF	371 388	398	368	398 415*	96	647	0.23	–5.60/ –2.48	–2.72/ –2.62	3.12	-
	PMMA	-	-	360	403 422	-	-	0.24	-	-	-	7.7/ n.o.

[a] Each onset wavelength (λ_{onset}) was determined by constructing a tangent on the point of inflection of the bathochromic slope of the most red-shifted absorption maximum. [b] Second emission due to resolved vibrational fine structure. [c] Quantum yields were determined by using a calibrated integrating sphere. [d] Stokes shifts represent the difference between each longest-wavelength absorption maximum and the corresponding shortest-wavelength emission maximum. [e] Full-width at half-maximum. [f] $E_{HOMO} = E_{LUMO} - E_G^{opt}$, $E_{LUMO} = -5.1\ eV - E_{onset}^{Red1}$ ($FcH/FcH^+ = -5.1$ eV in the Fermi scale[S13]). [g] Cyclic voltammograms were measured in THF with [nBu$_4$N][PF_6] (0.1 M) as the supporting electrolyte; referenced vs. FcH/FcH^+. [h] Optical band gap $E_G^{opt} = 1240 / \lambda_{onset}$. [i] Prompt and delayed emission lifetimes were estimated from the ns and ms range transient photoluminescence decay curves, respectively (PMMA matrix; 0.1 wt% of the respective emitter; 300 K). *) shoulder. n.o. = not observed.

3.1. Plots of UV/Vis absorption and emission spectra

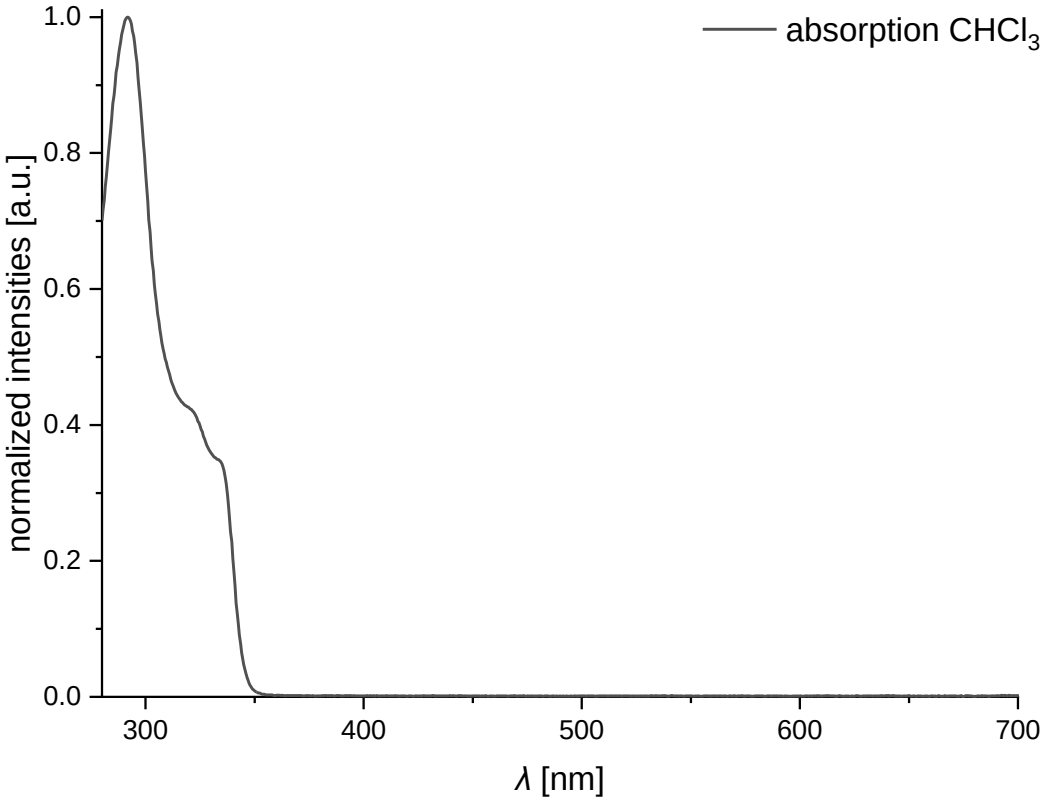

Figure S28. Normalized UV/Vis absorption spectrum of **1** ($CHCl_3$).

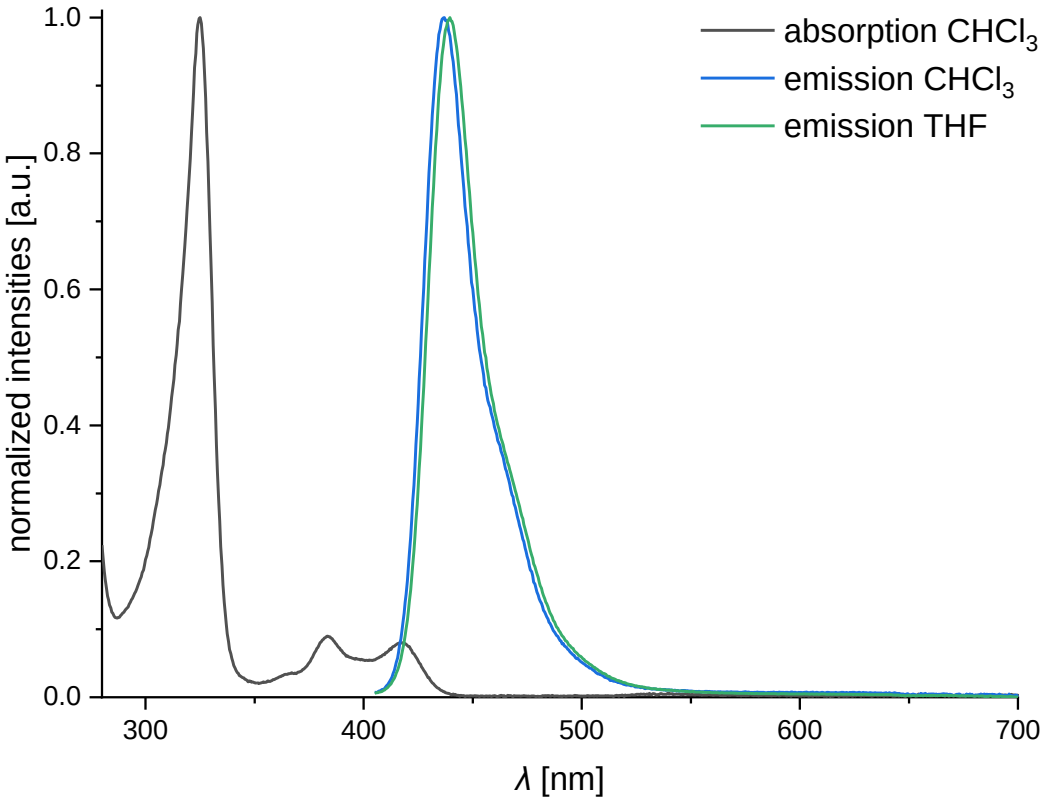

Figure S29. Normalized UV/Vis absorption and emission spectra of $\mathbf{2^{Mes}}$ (various solvents, λ_{ex} = 325 nm).

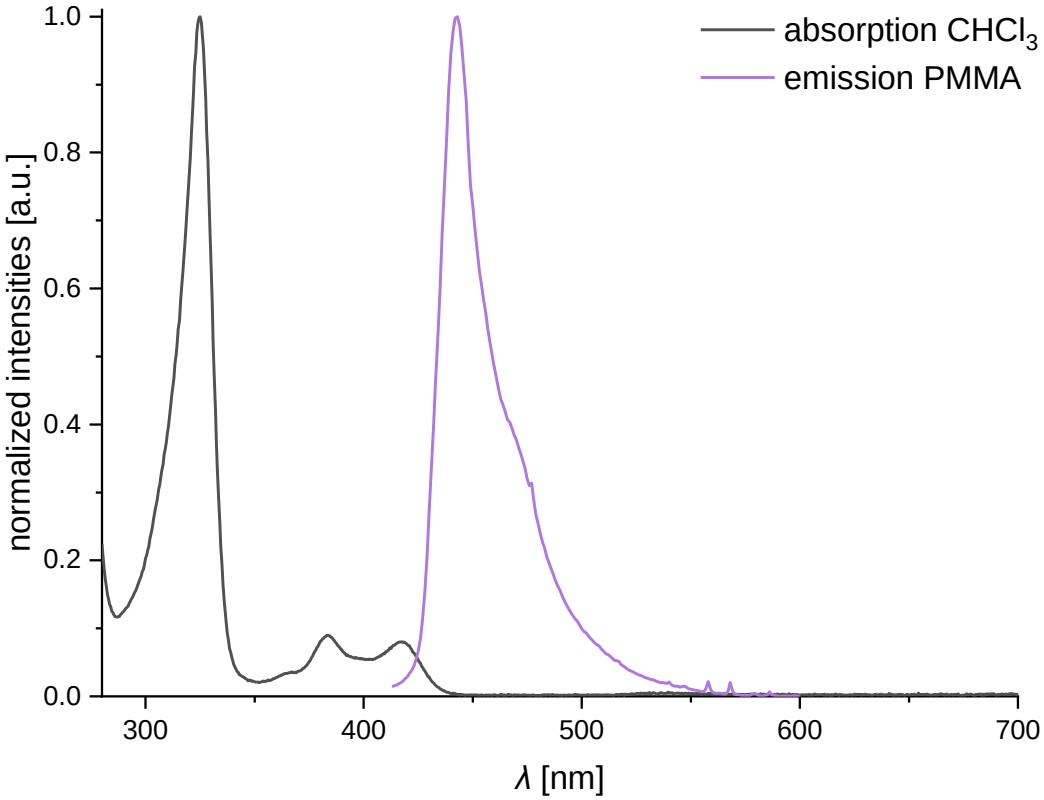

Figure S30. Normalized UV/Vis absorption ($CHCl_3$) and emission spectra (PMMA, 0.1 wt%) of $\mathbf{2^{Mes}}$ (λ_{ex} = 375 nm).

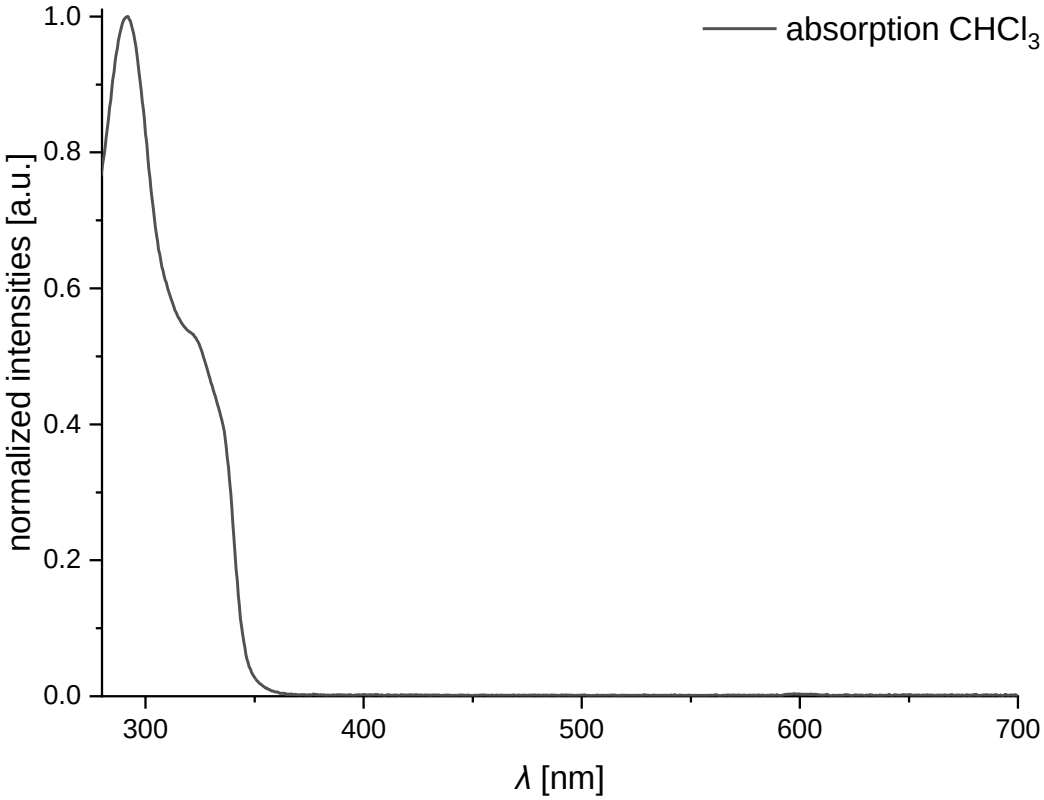

Figure S31. Normalized UV/Vis absorption spectrum of **5** ($CHCl_3$).

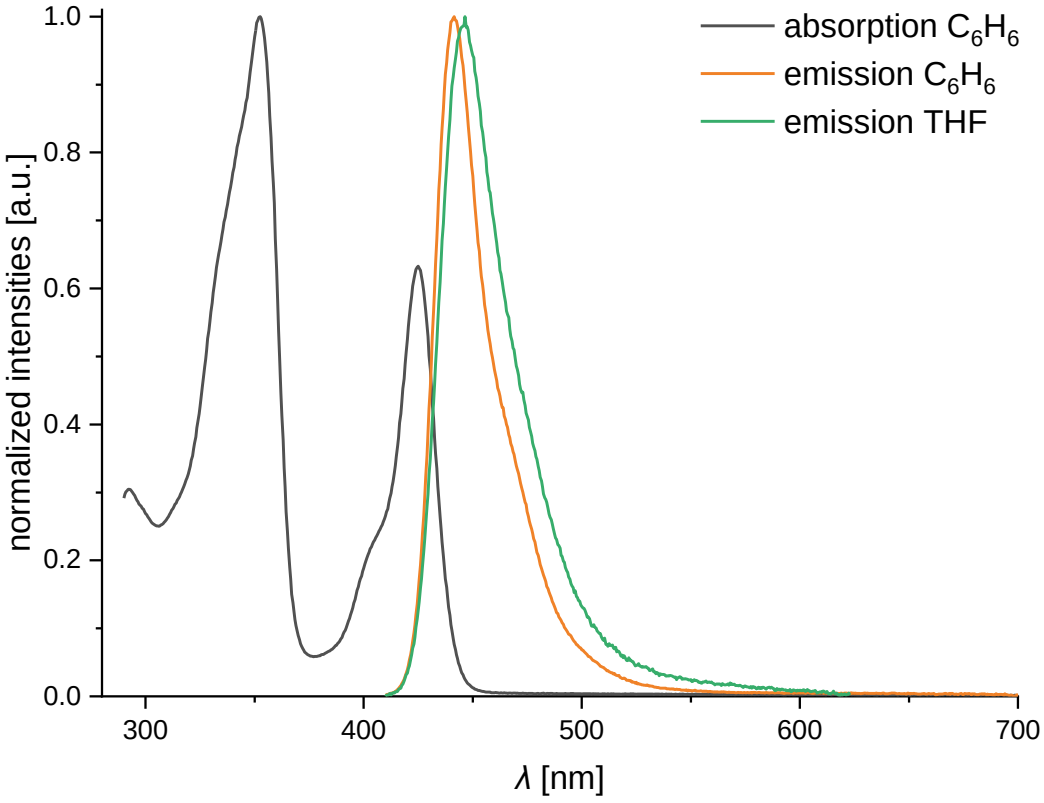

Figure S32. Normalized UV/Vis absorption and emission spectra of **6** (various solvents, λ_{ex} = 325 nm).

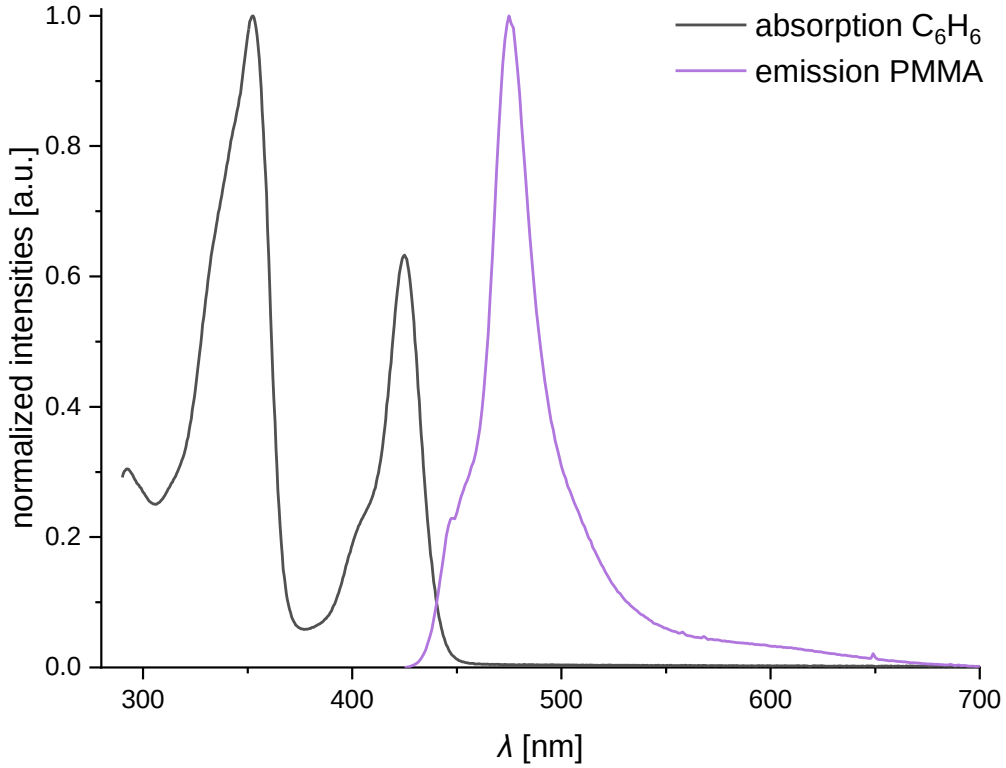

Figure S33. Normalized UV/Vis absorption (C_6H_6) and emission spectra (PMMA, 0.1 wt%) of **6** (λ_{ex} = 375 nm).

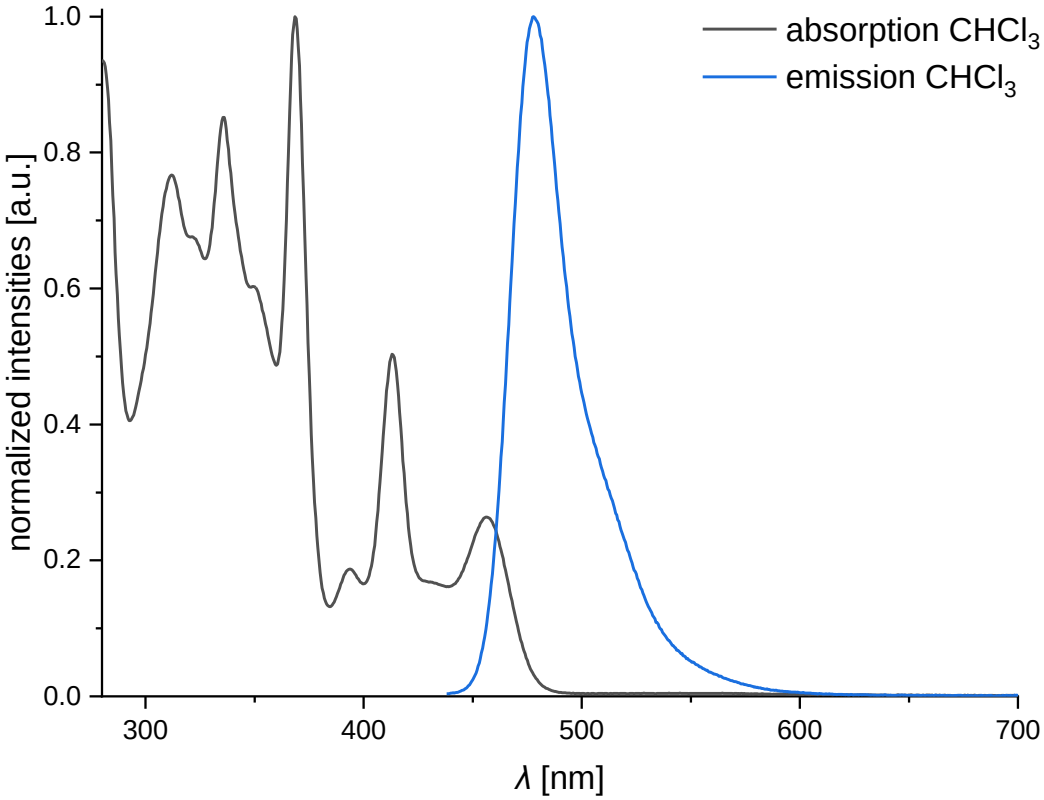

Figure S34. Normalized UV/Vis absorption and emission spectra of **7** ($CHCl_3$, λ_{ex} = 369 nm).

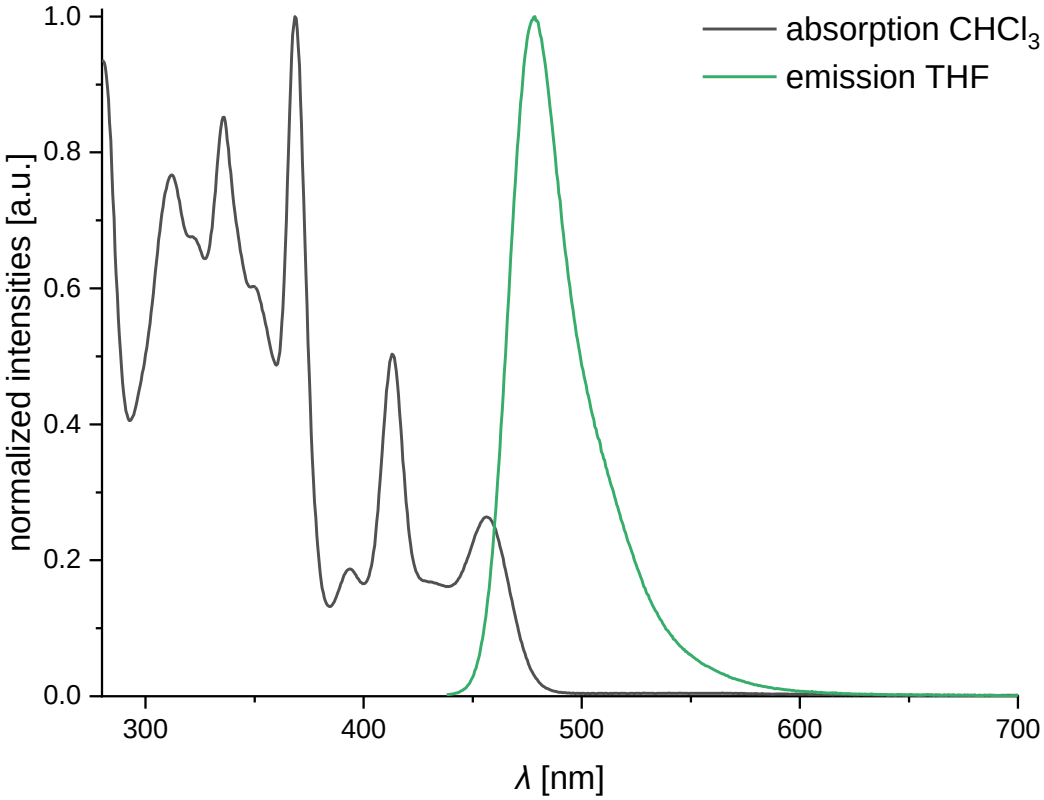

Figure S35. Normalized UV/Vis absorption ($CHCl_3$) and emission (THF) spectra of **7** (λ_{ex} = 369 nm).

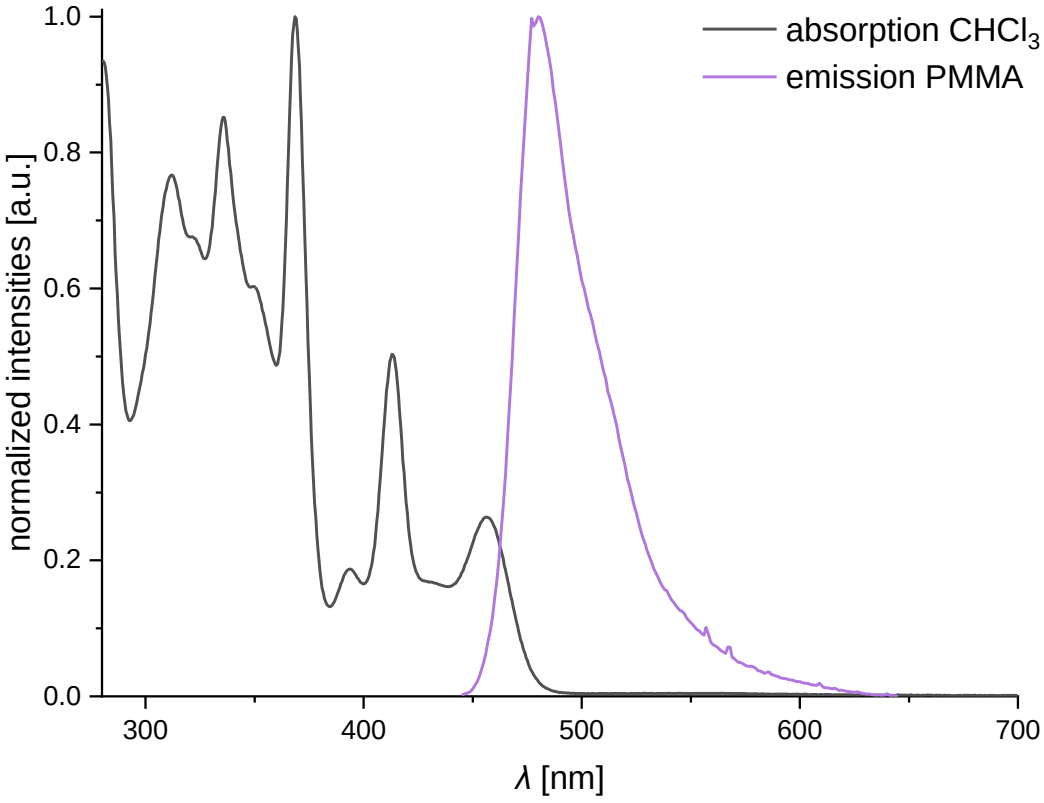

Figure S36. Normalized UV/Vis absorption ($CHCl_3$) and emission spectra (PMMA, 0.1 wt%) of **7** (λ_{ex} = 375 nm).

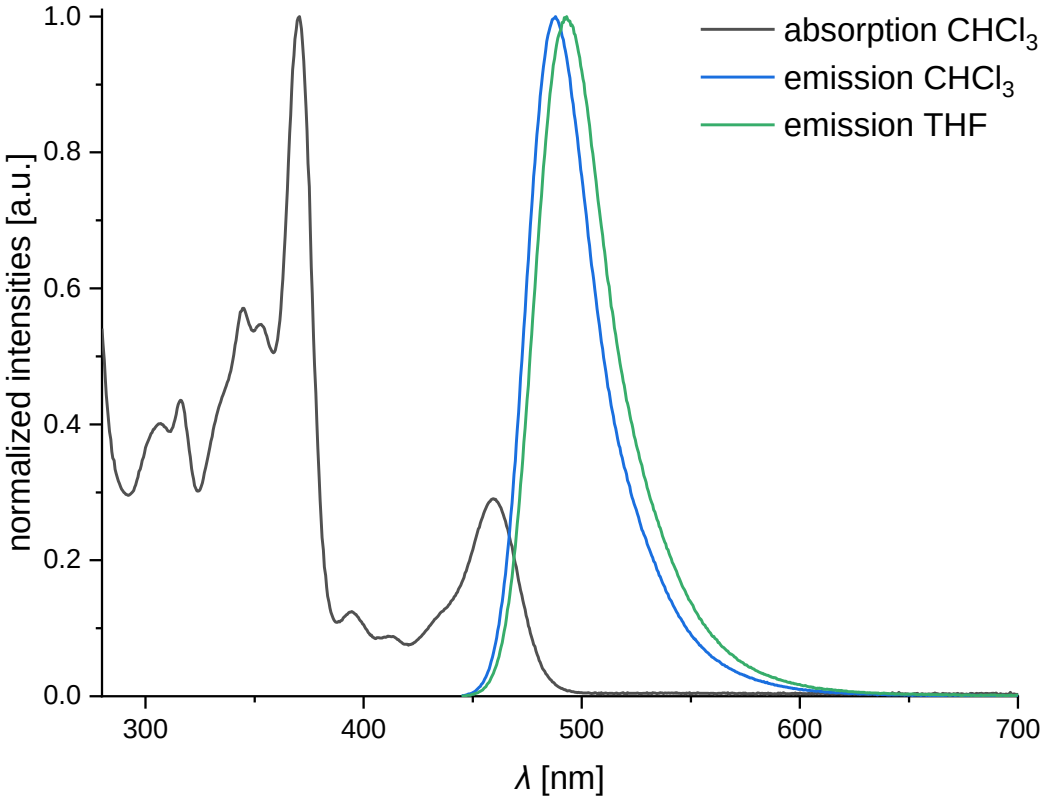

Figure S37. Normalized UV/Vis absorption and emission spectra of **8** (various solvents, λ_{ex} = 370 nm).

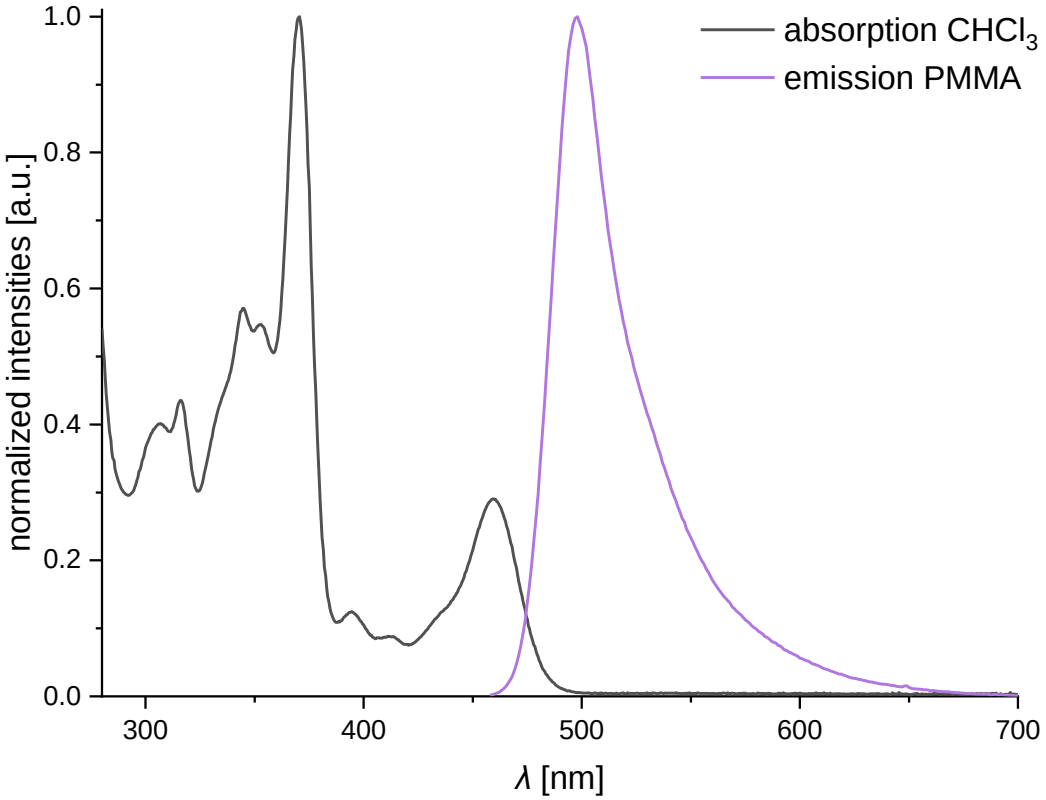

Figure S38. Normalized UV/Vis absorption ($CHCl_3$) and emission spectra (PMMA, 0.1 wt%) of **8** (λ_{ex} = 375 nm).

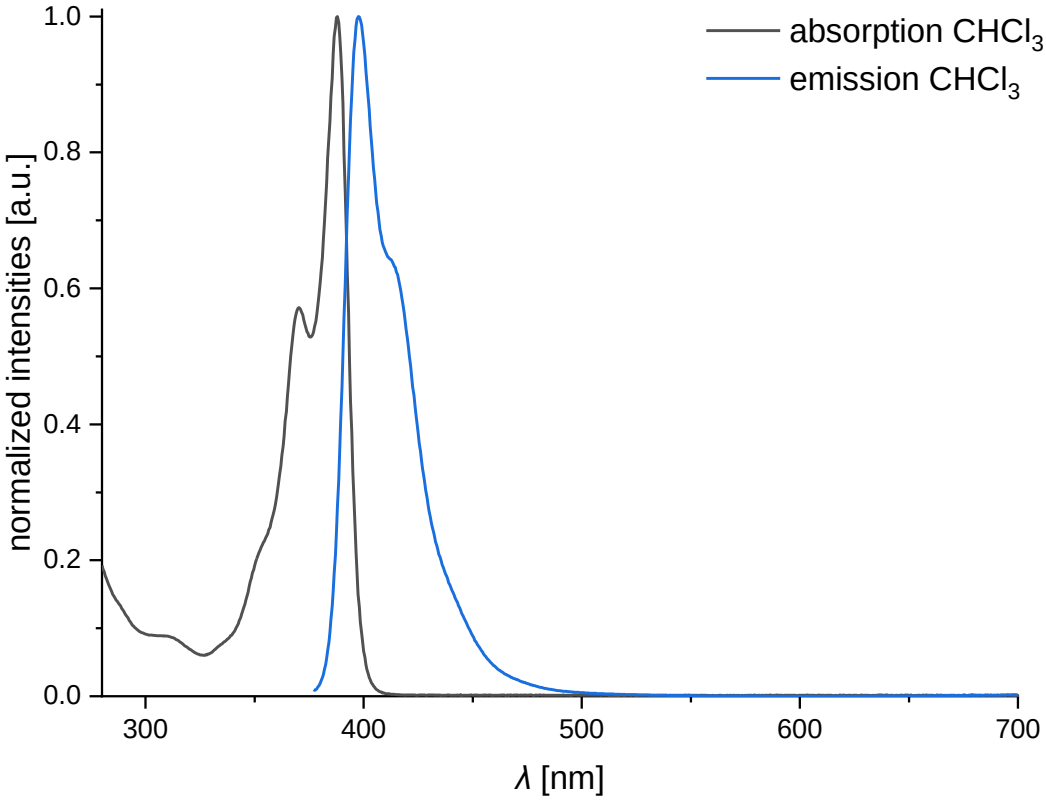

Figure S39. Normalized UV/Vis absorption and emission spectra of $\mathbf{9^{Mes}}$ ($CHCl_3$, λ_{ex} = 368 nm).

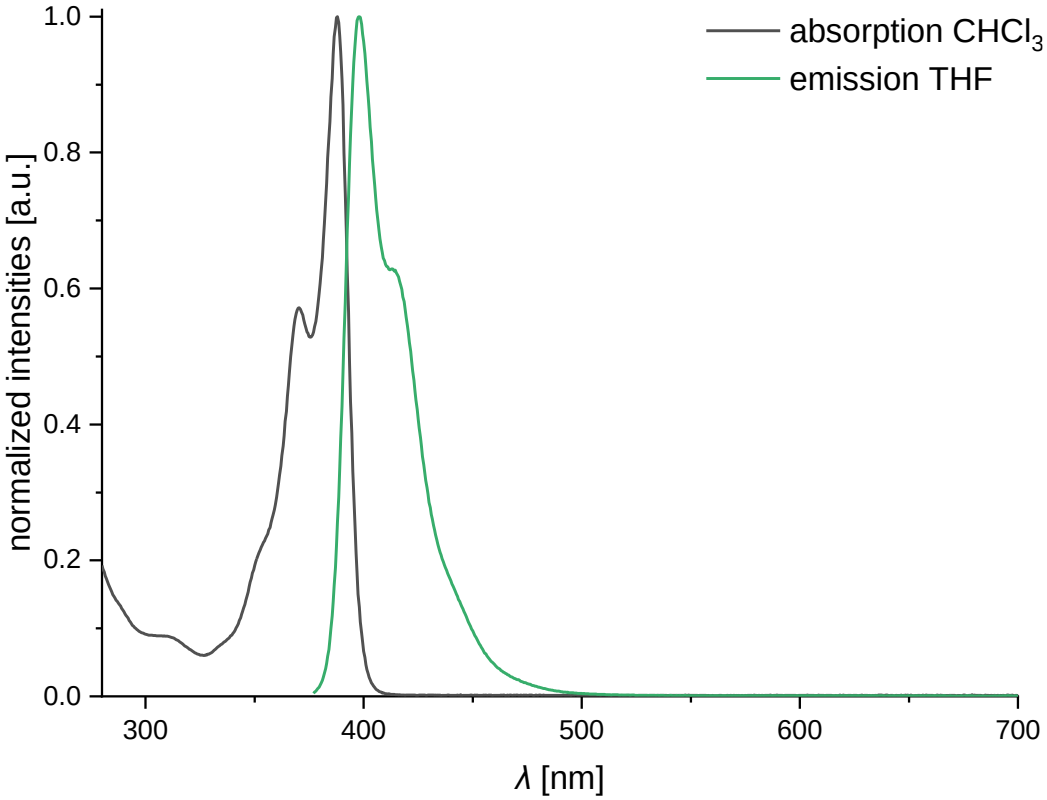

Figure S40. Normalized UV/Vis absorption ($CHCl_3$) and emission spectra (THF) of $\mathbf{9^{Mes}}$ (λ_{ex} = 368 nm).

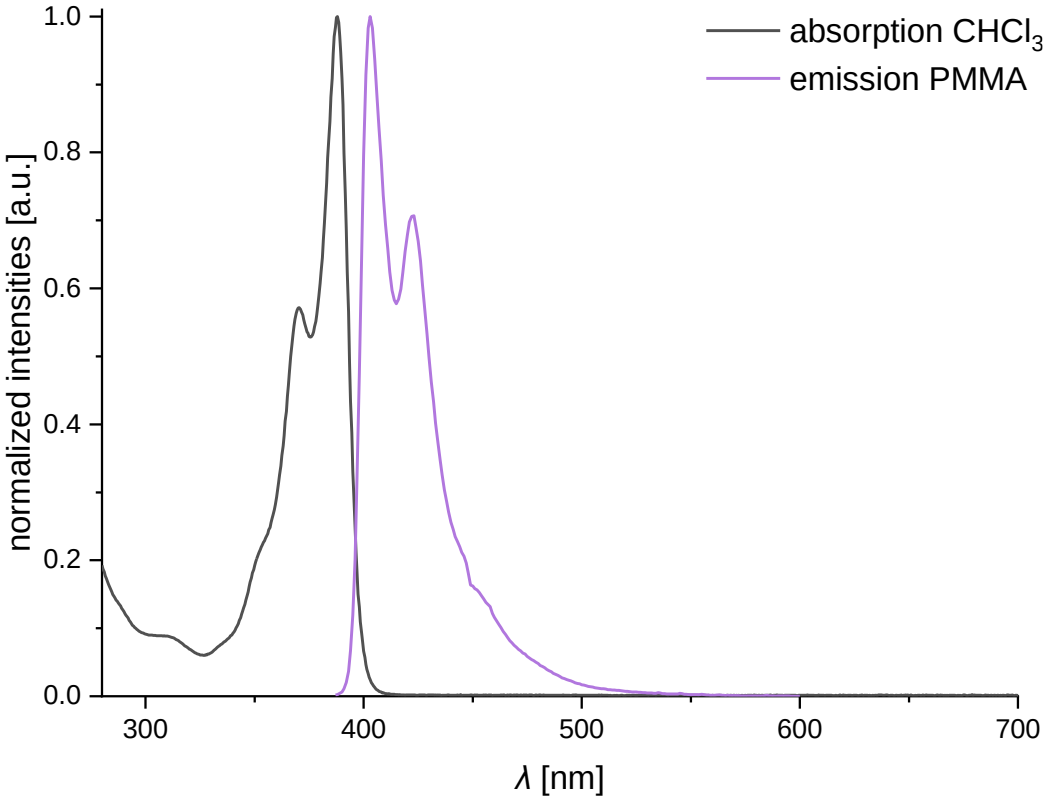

Figure S41. Normalized UV/Vis absorption ($CHCl_3$) and emission spectra (PMMA, 0.1 wt%) of $\mathbf{9^{Mes}}$ (λ_{ex} = 360 nm).

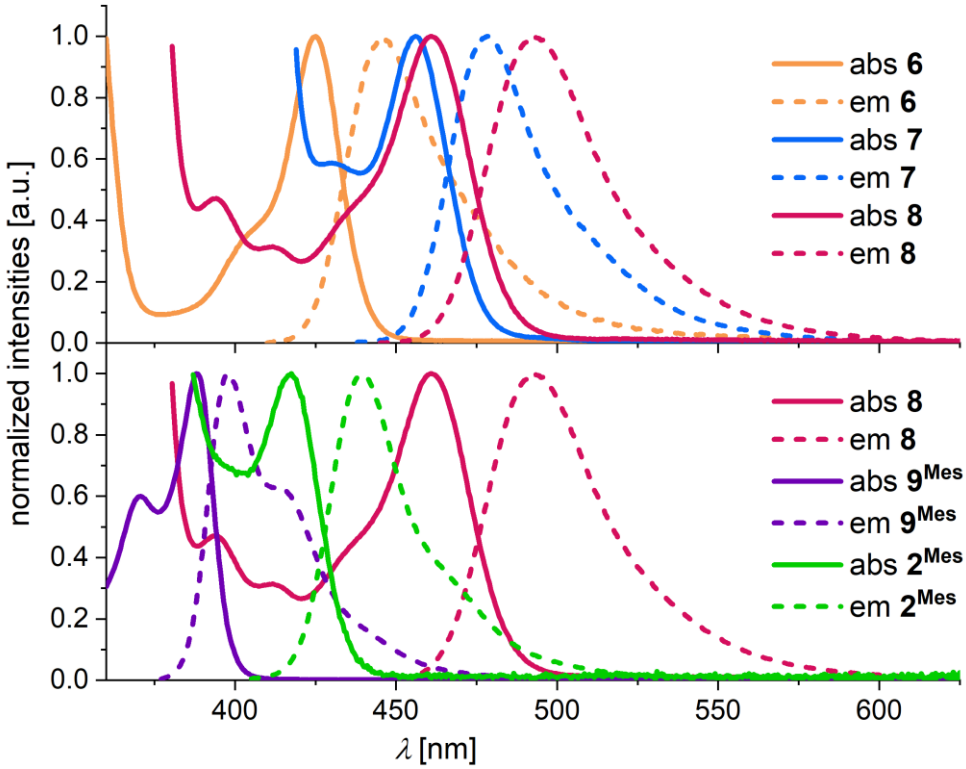

Chart S1. Normalized UV/Vis absorption and emission spectra of **6** (orange; λ_{ex} = 325 nm), **7** (blue; λ_{ex} = 369 nm), **8** (red; λ_{ex} = 370 nm), $\mathbf{9^{Mes}}$ (purple; λ_{ex} = 368 nm), and $\mathbf{2^{Mes}}$ (green; λ_{ex} = 325 nm), measured in THF.

3.2. Plots of transient decay curves

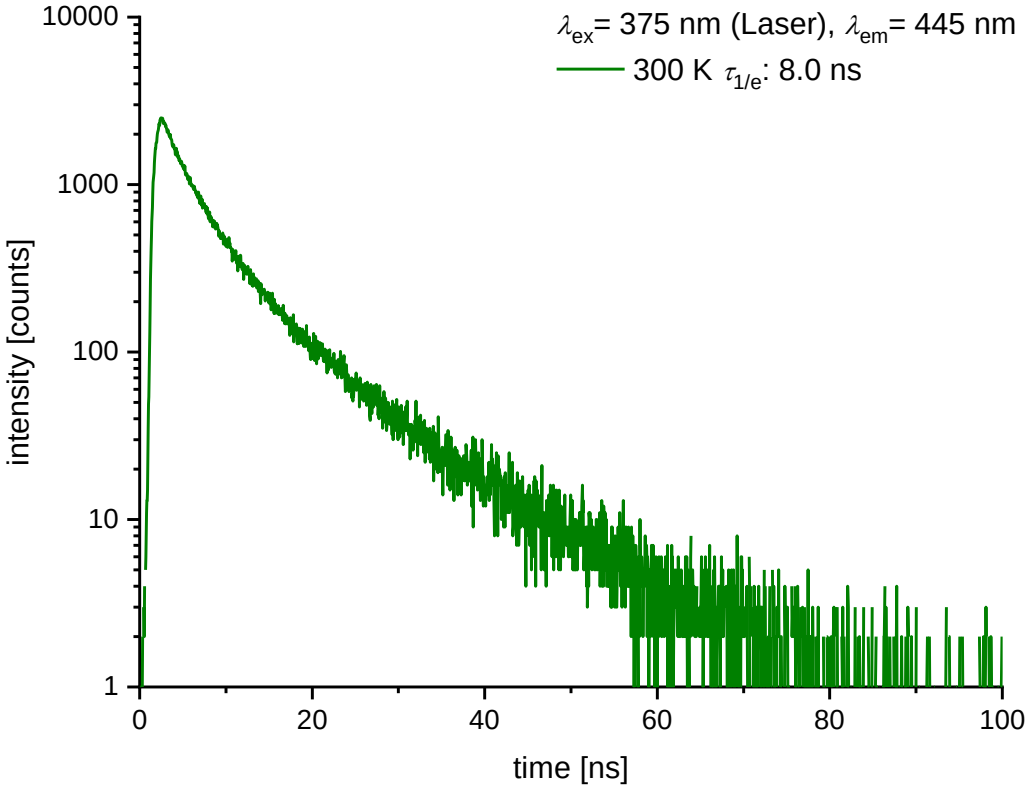

Figure S42. Transient photoluminescence decay curve of the prompt emission of **2^{Mes}** (300 K, PMMA, 0.1 wt%).

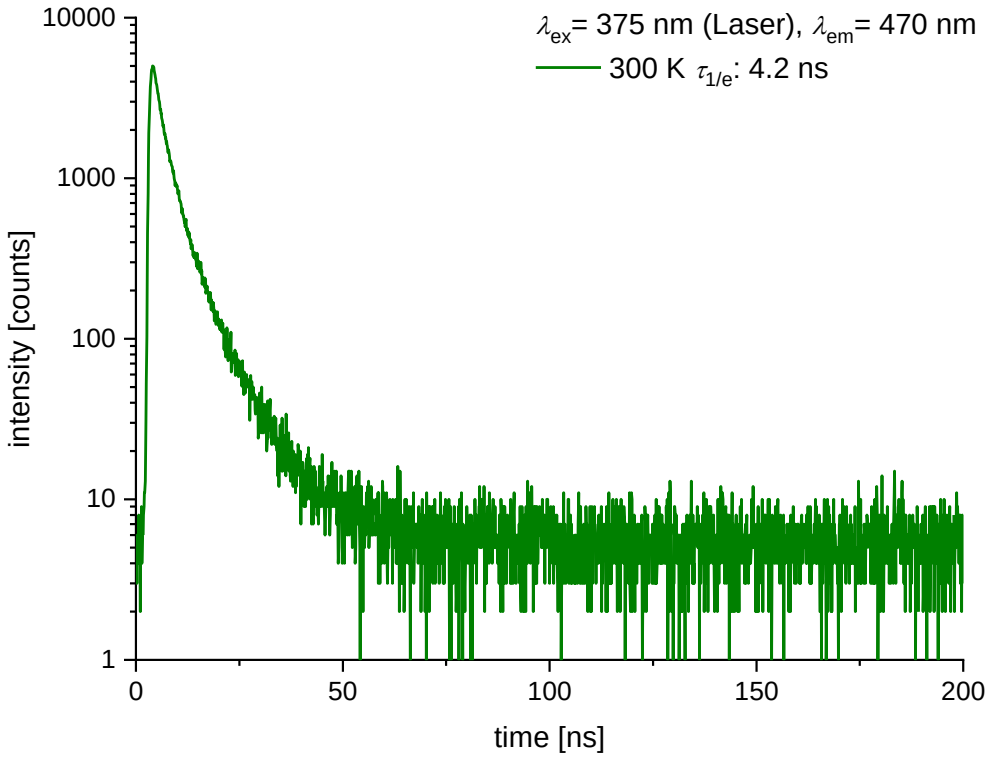

Figure S43. Transient photoluminescence decay curve of the prompt emission of **6** (300 K, PMMA, 0.1 wt%).

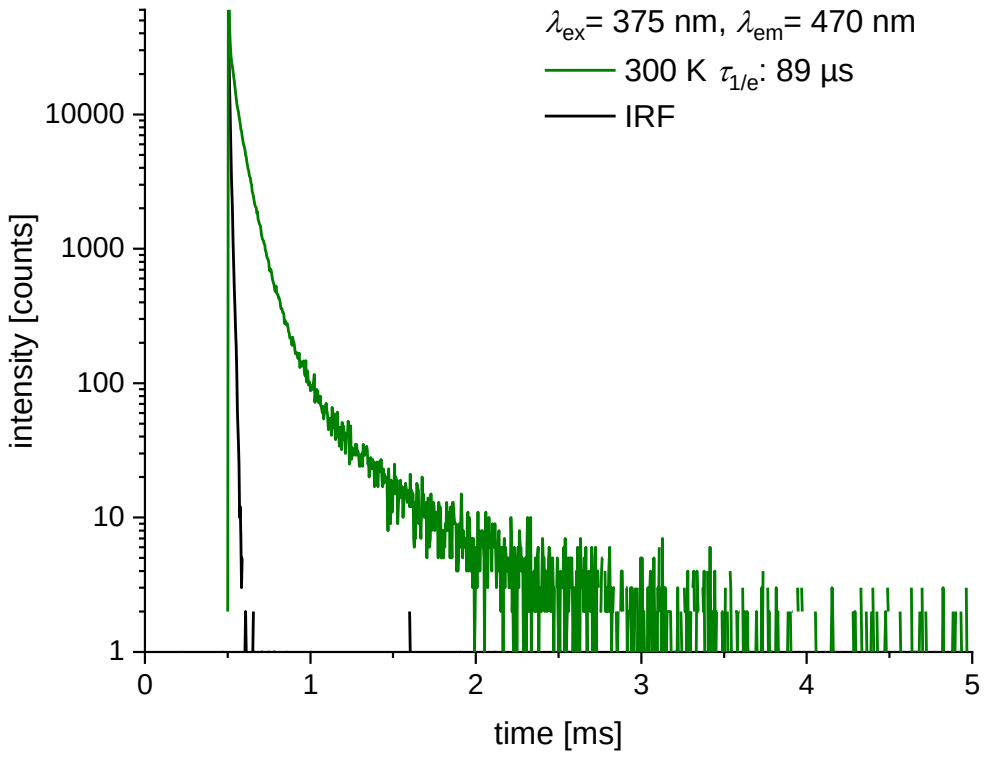

Figure S44. Transient photoluminescence decay curve of the delayed emission of **6** (300 K, PMMA, 0.1 wt%). IRF = Instrument response function.

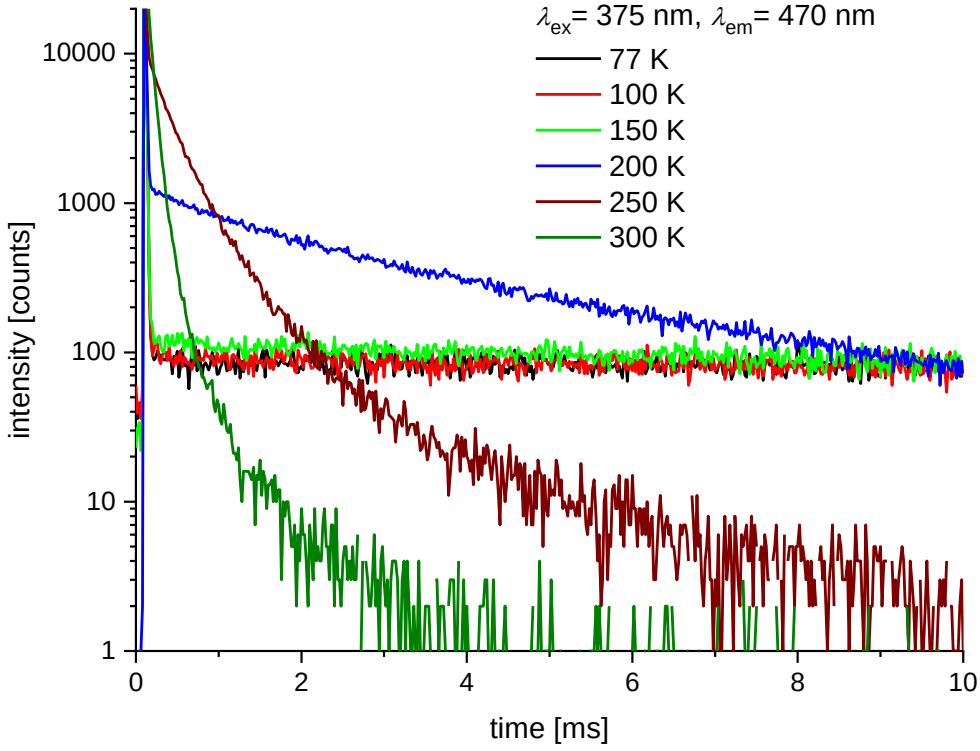

Figure S45. Transient photoluminescence decay curves of the delayed emission of **6** at different temperatures (PMMA, 0.1 wt%).

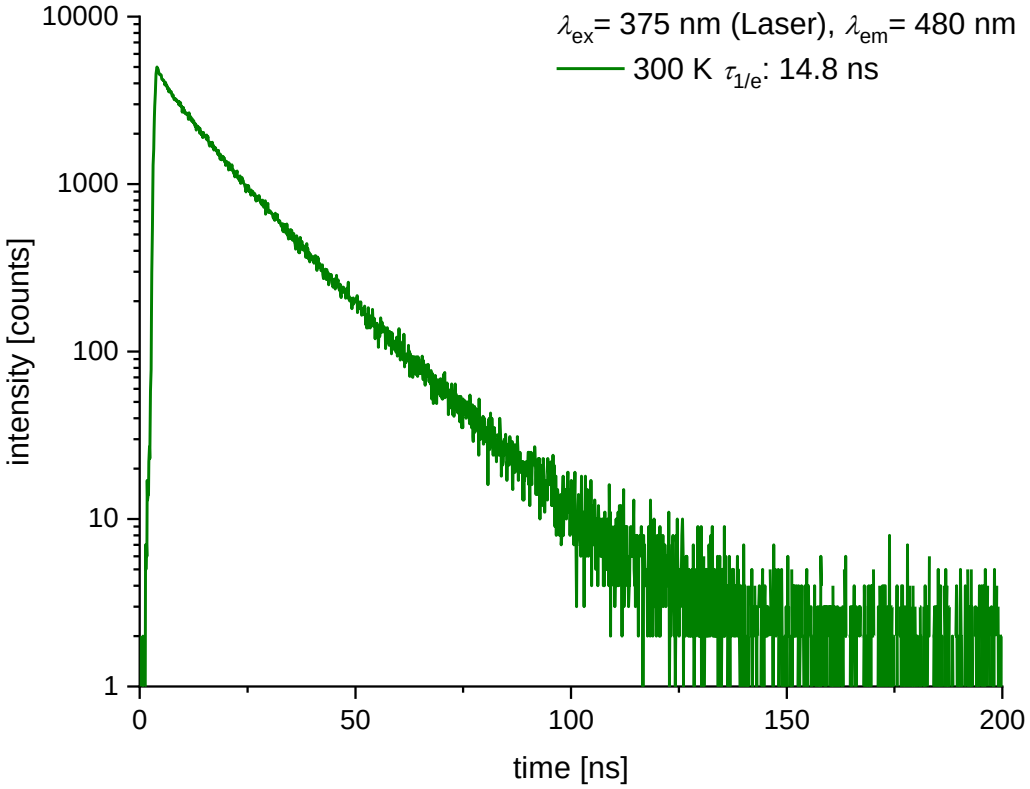

Figure S46. Transient photoluminescence decay curve of the prompt emission of **7** (300 K, PMMA, 0.1 wt%).

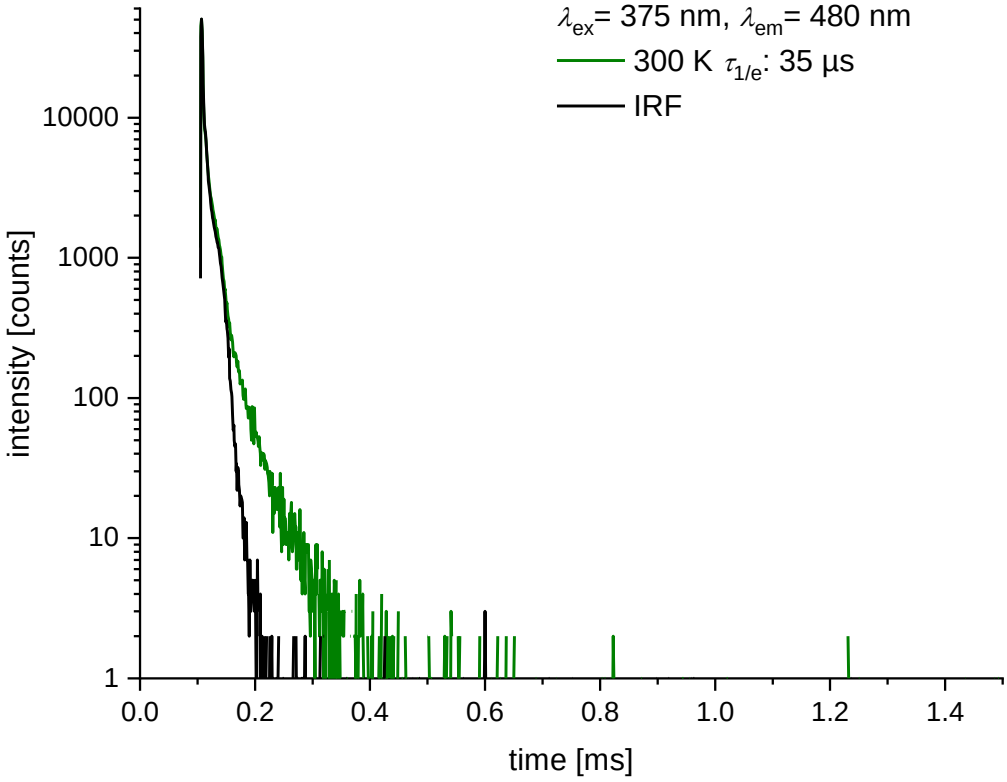

Figure S47. Transient photoluminescence decay curve of the delayed emission of **7** (300 K, PMMA, 0.1 wt%). IRF = Instrument response function.

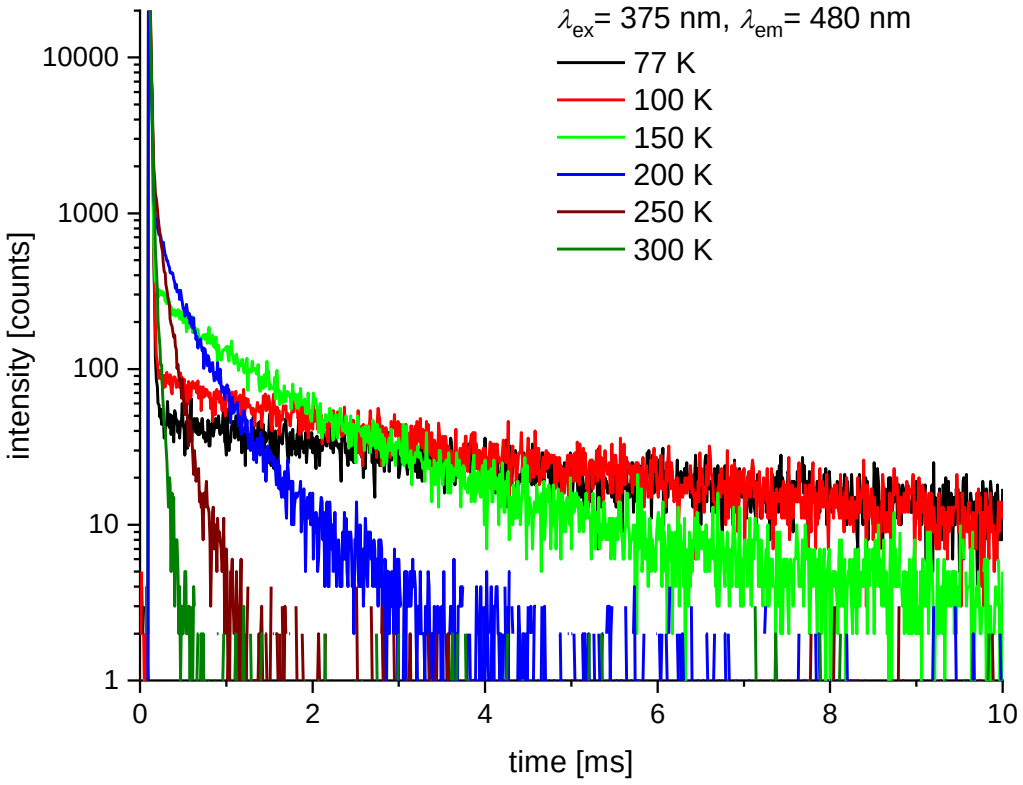

Figure S48. Transient photoluminescence decay curves of the delayed emission of **7** at different temperatures (PMMA, 0.1 wt%).

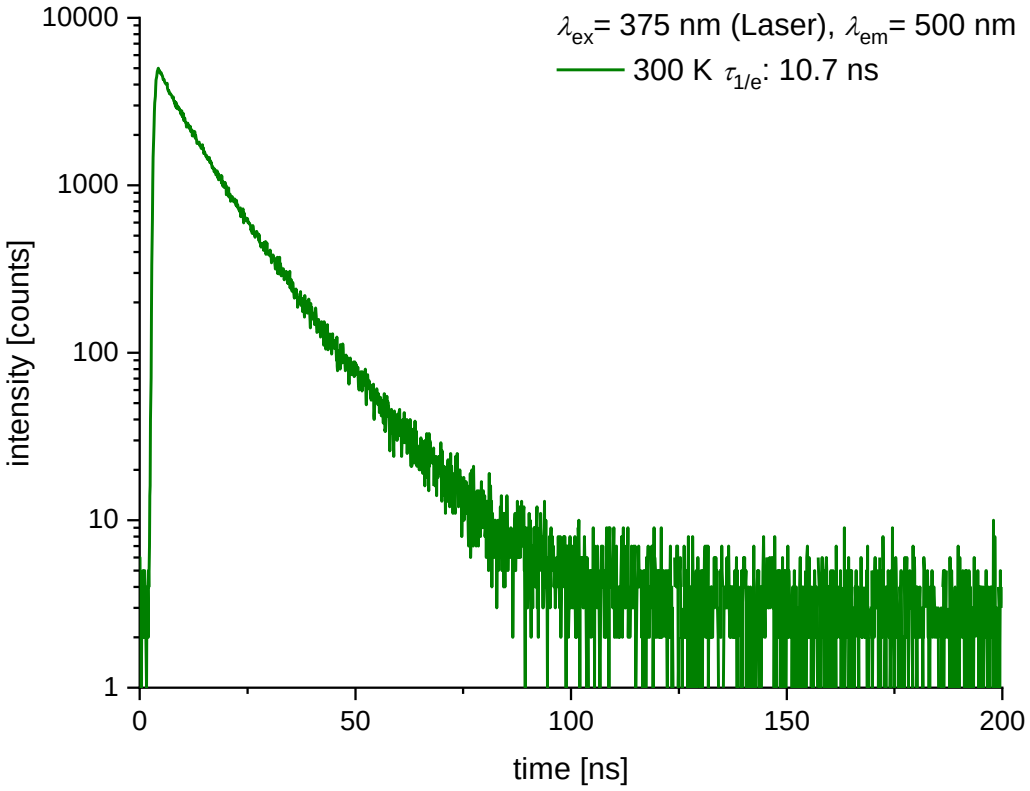

Figure S49. Transient photoluminescence decay curve of the prompt emission of **8** (300 K, PMMA, 0.1 wt%).

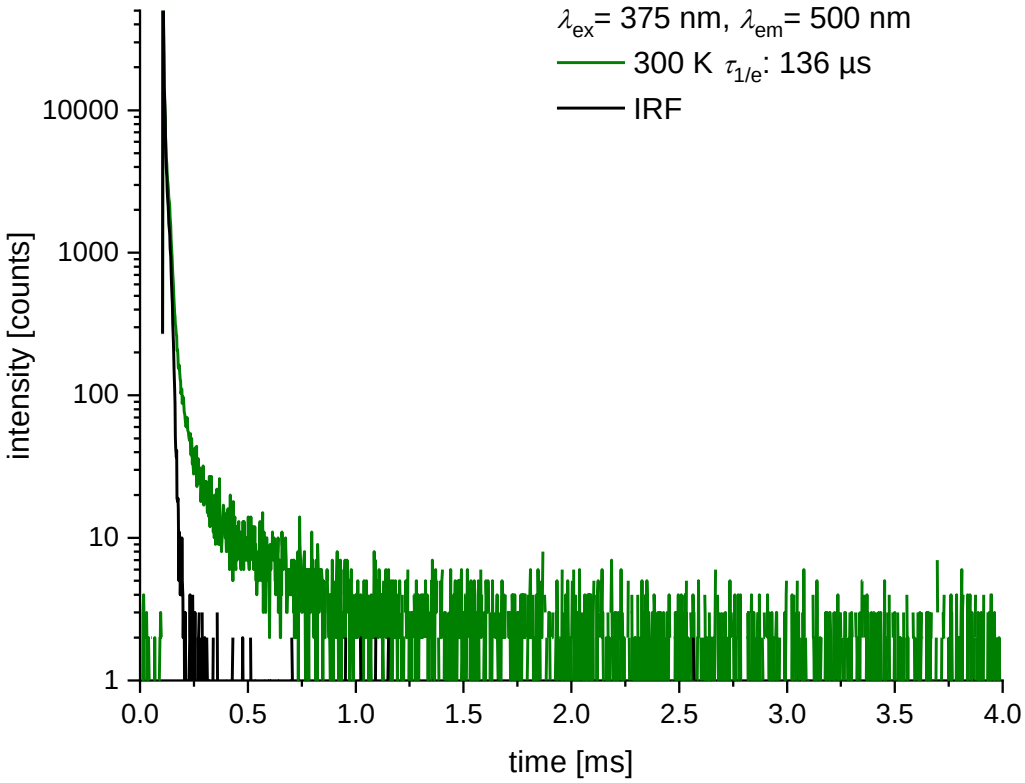

Figure S50. Transient photoluminescence decay curve of the delayed emission of **8** (300 K, PMMA, 0.1 wt%). IRF = Instrument response function.

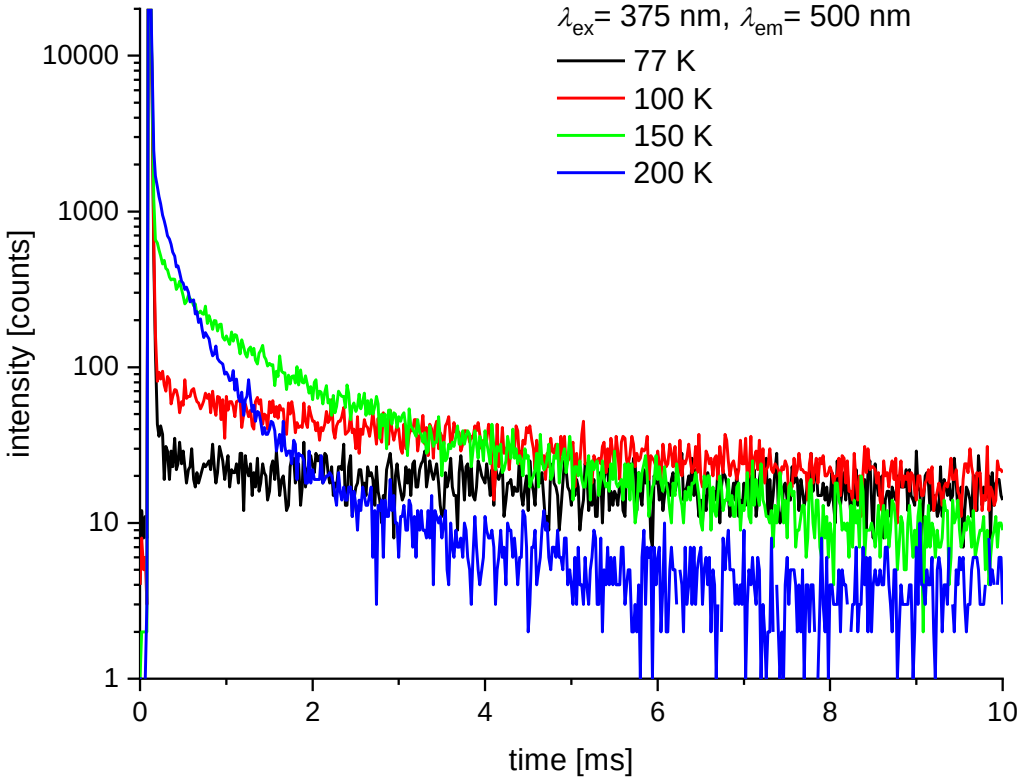

Figure S51. Transient photoluminescence decay curves of the delayed emission of **8** at different temperatures (PMMA, 0.1 wt%).

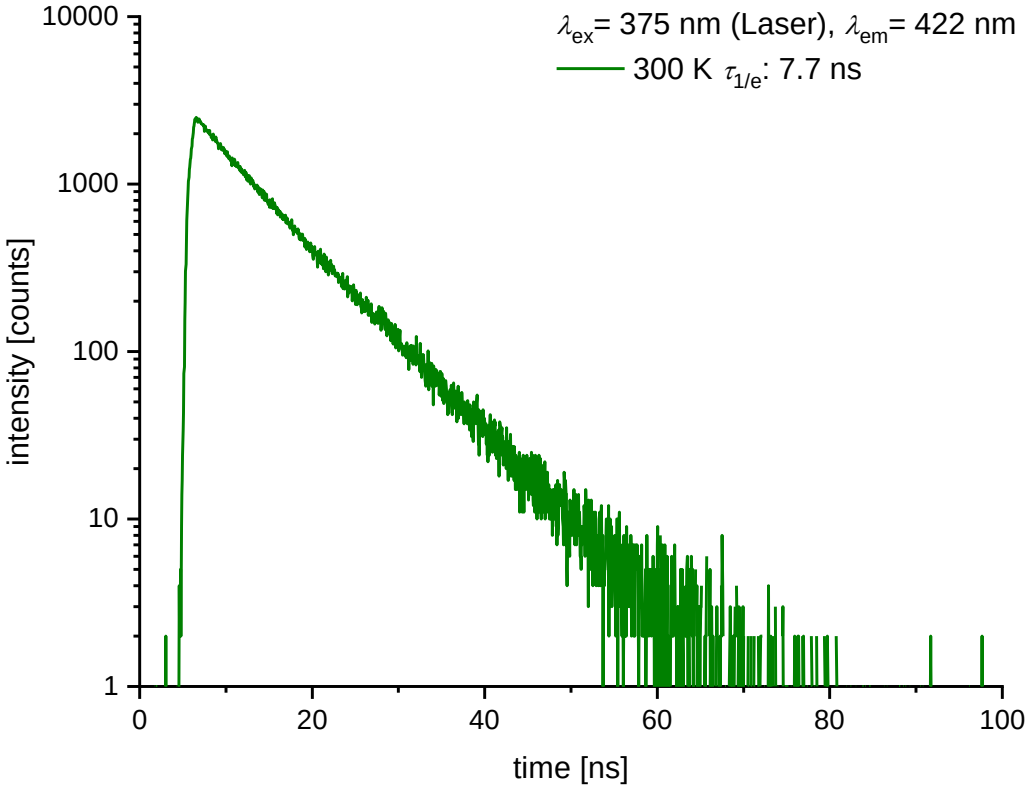

Figure S52. Transient photoluminescence decay curve of the prompt emission of **9^{Mes}** (300 K, PMMA, 0.1 wt%).

3.3. Plots of cyclic voltammograms

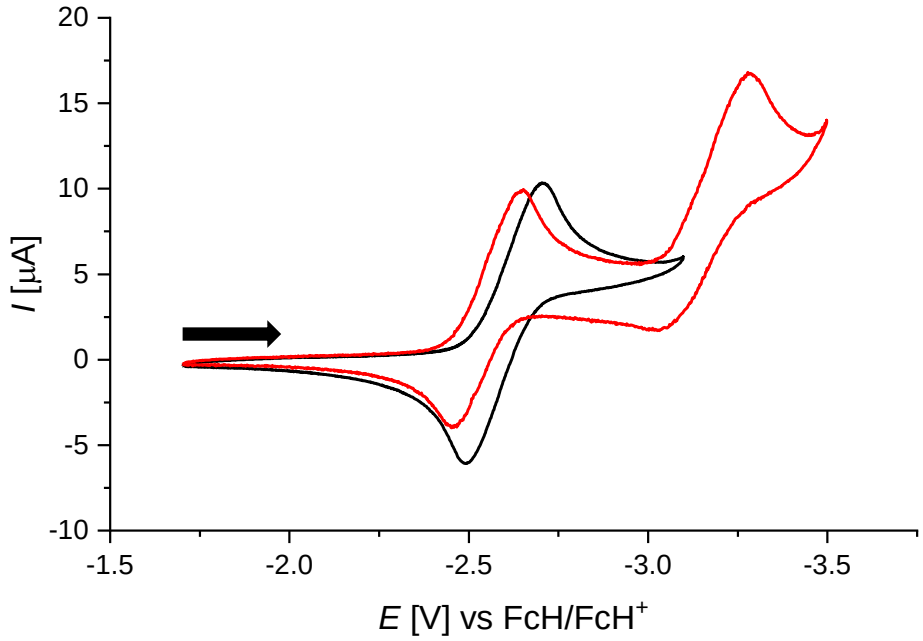

Figure S53. Cyclic voltammogram of **2^{Mes}** in THF (room temperature, supporting electrolyte: [*n*Bu$_4$N][PF$_6$] (0.1 M), scan rate: 200 mV s^{-1}). Black: switching potential = –3.10 V; red: switching potential = –3.50 V.

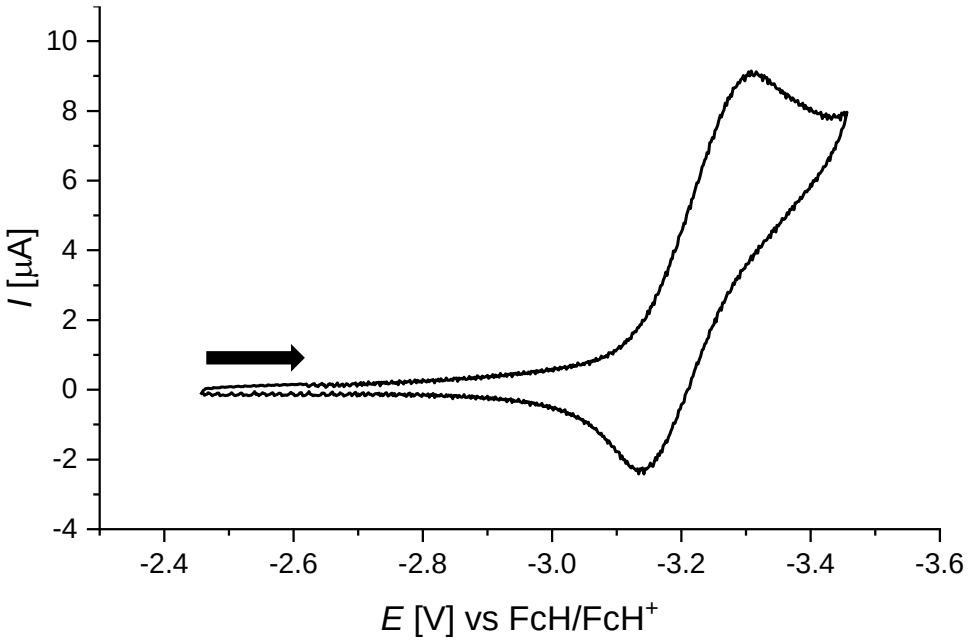

Figure S54. Cyclic voltammogram of **5** in THF (room temperature, supporting electrolyte: [*n*Bu$_4$N][PF$_6$] (0.1 M), scan rate: 600 mV s^{-1}).

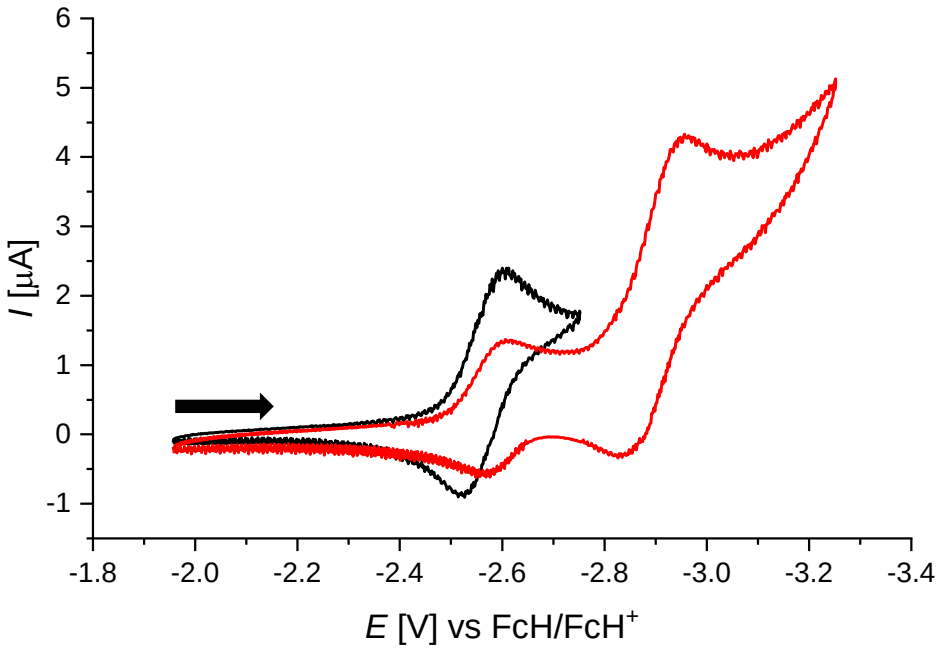

Figure S55. Cyclic voltammogram of **6** in THF (room temperature, supporting electrolyte: [nBu$_4$N][PF$_6$] (0.1 M), scan rate: 200 mV s^{-1}). Black: switching potential = –2.75 V; red: switching potential = –3.25 V.

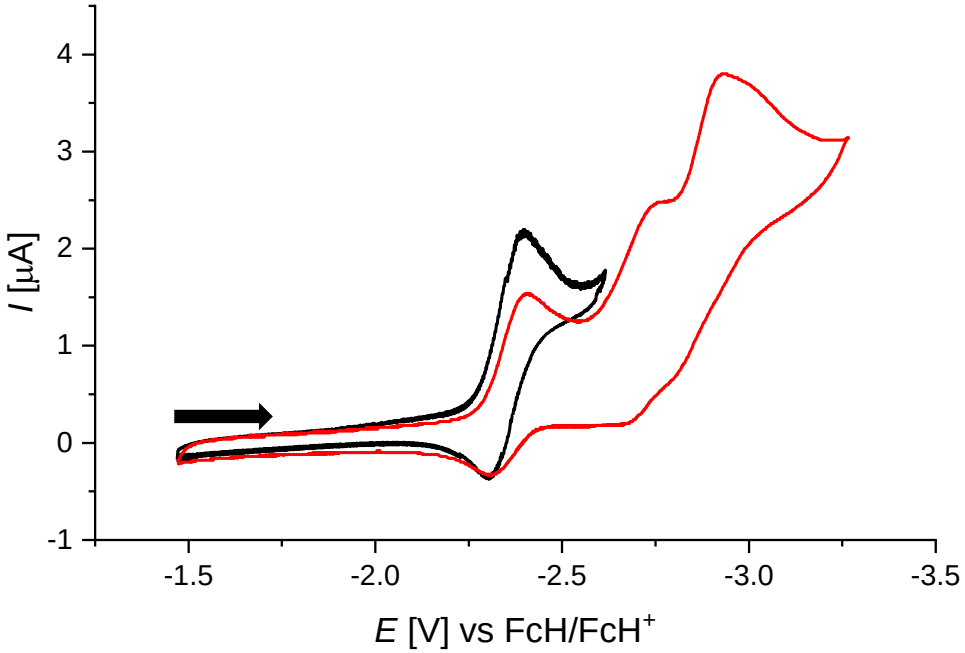

Figure S56. Cyclic voltammogram of **7** in THF (room temperature, supporting electrolyte: [nBu$_4$N][PF$_6$] (0.1 M), scan rate: 200 mV s^{-1}). Black: switching potential = –2.62 V; red: switching potential = –3.27 V.

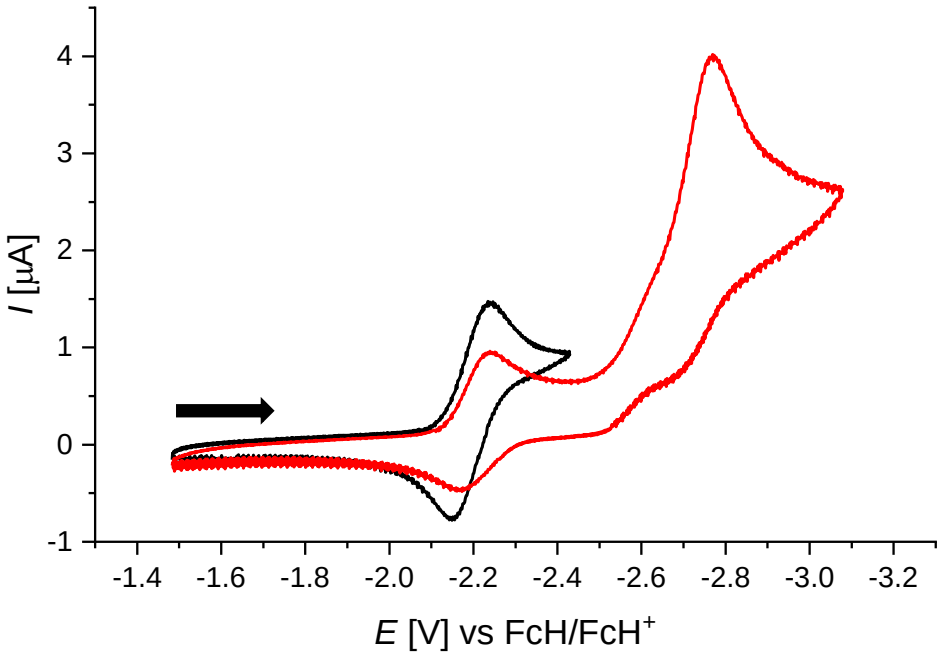

Figure S57. Cyclic voltammogram of **8** in THF (room temperature, supporting electrolyte: [nBu$_4$N][PF$_6$] (0.1 M), scan rate: 200 mV s^{-1}). Black: switching potential = –2.43 V; red: switching potential = –3.10 V.

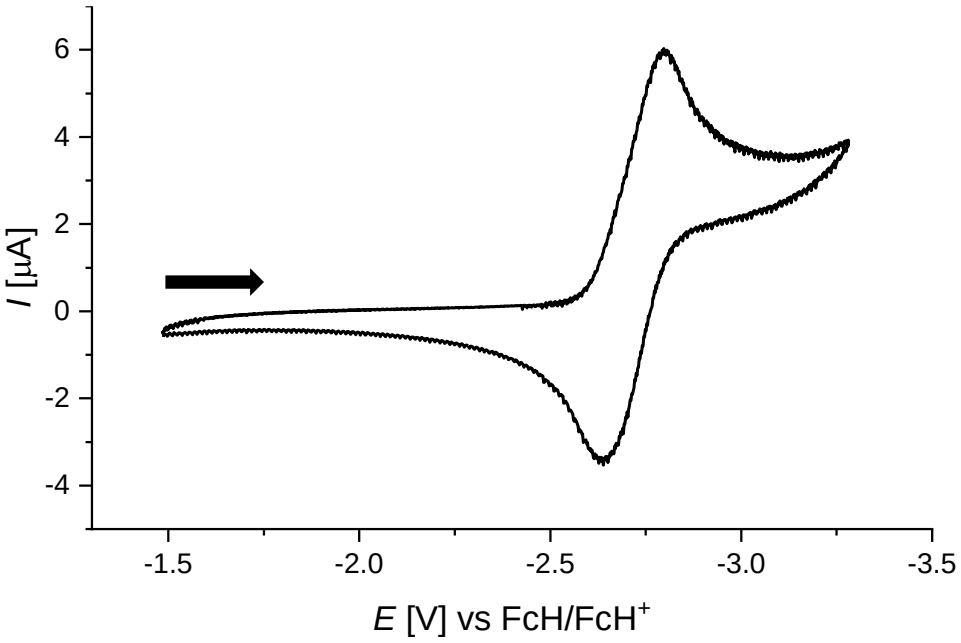

Figure S58. Cyclic voltammogram of **9^{Mes}** in THF (room temperature, supporting electrolyte: [nBu$_4$N][PF$_6$] (0.1 M), scan rate: 200 mV s^{-1}).

4. Single-crystal X-ray structure analyses

Single-crystal diffraction data for all compounds, except for **2**^{Mes}, **7**, and **8**, were collected at 173(2) K on a *STOE IPDS II* two-circle diffractometer equipped with a *Genix 3D HS* microfocus MoK_α X-ray source (λ = 0.71073 Å). The finalization of the data, including empirical absorption corrections, was done using the *CrysAlisPro* software v.1.171.42.43a (*Rigaku Oxford Diffraction*, 2022). The structures were solved using the *SHELXT* program and refined against $|F|^2$ with full-matrix least-squares techniques using the program *SHELXL*-2018/3.[S14,S15] All H atoms were located geometrically and refined riding on the pivot atom.

The diffraction data for the weakly scattering crystals of **2**^{Mes}, **7**, and **8** were collected at T = 100(2) K in the P24 beamline at the *DESY PETRA III* synchrotron (Hamburg). The EH2 end-station is equipped with a four-circle *HUBER* diffractometer with Eulerian geometry and either a *DECTRIS Pilatus3 CdTe* or a *X-Spectrum Lambda 7.5M CdTe* pixel array detector. The data were acquired by 360° ϕ-rotation with 0.4–0.5° scan width and an exposure time of 1.5–4 s per frame with the wavelength λ = 0.5 Å (24.797 keV) or λ = 0.56002 Å (22.139 keV). In the case of the *Lambda 7.5M CdTe* detector, two scans were performed for each crystal at different positions of the detector (2Θ = 0 and 10°) to overcome the loss of data due to rather wide gaps on the detector array. The diffraction data were integrated, merged, and all corrections were applied using the *CrysAlisPro* software v.1.171.42.43a (*Rigaku Oxford Diffraction*, 2022).

CIF files containing the crystallographic information are deposited in the Cambridge Crystallographic Data Centre under the deposition codes CCDC 2338843–2338851 and can be obtained free of charge via www.ccdc.cam.ac.uk/data_request/cif. Crystallographic data and parameters of the diffraction experiments are given in Tables S2–S6.

Table S2. Selected crystallographic data for two polymorphous modifications of **1**.

	α-**1**	β-**1**
Chemical formula	$C_{34}H_{32}N_2Si_2$	$C_{34}H_{32}N_2Si_2$
M_r	524.79	524.79
Crystal system, space group	Monoclinic, $P2_1/c$	Orthorhombic, $P2_12_12$
Temperature (K)	238	238
a, b, c (Å)	15.0752(11), 11.957 (10), 15.912 (11)	33.900(3), 12.1623(7), 15.9963(11)
α, β, γ (°)	90, 93.715(7), 90	90, 117.866(8), 90
V (Å^3)	2862.4(4)	1462.6(4)
Z	4	8
F(000)	1112	2224
D_x (Mg m^{-3})	1.218	1.196
Radiation type	Mo $K\alpha$	Mo $K\alpha$
μ (mm^{-1})	0.15	0.15
Crystal shape	Plate	Elongated plate (plank)
Color	Colorless	Colorless
Crystal size (mm)	0.35 × 0.14 × 0.04	0.50 × 0.18 × 0.10
Absorption correction	Multi-scan	Multi-scan
T_{min}, T_{max}	0.355, 1.000	0.691, 1.000
No. of measured, independent and observed [$I > 2s(I)$] reflections	19133, 5426, 3711	21123, 5517, 4002
R_{int}	0.087	0.076
Θ_{max} (°)	25.7	25.7
Range of h, k, l	h = –18→18, k = –12→14, l = –19→19	h = –41→41, k = –12→14, l = –19→19
$R[F^2 > 2s(F^2)]$, $wR(F^2)$, S	0.056, 0.147, 1.03	0.054, 0.149, 1.03
No. of reflections	5426	5517
No. of parameters	347	347
$\Delta\rho_{max}$, $\Delta\rho_{min}$ (e Å^{-3})	0.64, –0.28	0.65, –0.51

Computer programs: *X-AREA* (*Stoe & Cie*, 2001), *CrysAlis PRO* 1.171.42.43a (*Rigaku OD*, 2022), *SHELXS* (G. M. Sheldrick, 1997), *SHELXT* (G. M. Sheldrick, 2015), *SHELXL2018*/3 (Sheldrick, 2018).

Table S3. Selected crystallographic data for $\mathbf{2^{Br}}$ and $\mathbf{2^{Mes}}$.

	$\mathbf{2^{Br}}$	$\mathbf{2^{Mes}}$
Chemical formula	$C_{30}H_{20}B_2Br_2N_2$	$C_{48}H_{42}B_2N_2$
M_r	589.92	668.45
Crystal system, space group	Triclinic, $P\bar{1}$	Monoclinic, $P2_1/c$
Temperature (K)	173	100
a, b, c (Å)	10.4916(15), 11.4820(12), 12.0304(12)	14.4866(2), 9.54883(17), 27.3251(5)
α, β, γ (°)	66.894(9), 72.833(10), 80.133(10)	90, 96.5701(15), 90
V (Å^3)	1271.0(3)	3755.05(11)
Z	2	4
F(000)	588	1416
D_x (Mg m^{-3})	1.541	1.182
Radiation type	Mo $K\alpha$	Synchrotron, DESY P24 beamline, λ = 0.56002 Å
μ (mm^{-1})	3.21	0.04
Crystal shape	Needle	Needle
Color	Yellow	Colorless
Crystal size (mm)	0.47 × 0.06 × 0.05	0.51 × 0.06 × 0.03
Absorption correction	Multi-scan	Multi-scan
T_{min}, T_{max}	0.535, 1.000	0.855, 1.000
No. of measured, independent and observed [I > 2s(I)] reflections	15155, 4798, 3529	47662, 7389, 5784
R_{int}	0.079	0.082
Θ_{max} (°)	25.7	20.5
Range of h, k, l	h = –12→12, k = –13→14, l = –14→14	h = –18→18, k = –11→11, l = –34→34
$R[F^2 > 2s(F^2)]$, $wR(F^2)$, S	0.048, 0.117, 1.02	0.046, 0.139, 1.08
No. of reflections	4798	7389
No. of parameters	325	475
$\Delta\rho_{max}$, $\Delta\rho_{min}$ (e Å^{-3})	0.56, –0.59	0.20, –0.25

Computer programs: *X-AREA* (*Stoe & Cie*, 2001), *CrysAlis PRO* 1.171.42.43a (*Rigaku OD*, 2022), *SHELXS* (G. M. Sheldrick, 1997), *SHELXT* (G. M. Sheldrick, 2015), *SHELXL2018*/3 (Sheldrick, 2018).

Table S4. Selected crystallographic data for **5** and **6**·0.25(toluene).

	5	**6**·0.25(toluene)
Chemical formula	$C_{48}H_{45}N_3Si_3$	$C_{42}H_{27}B_2N_3$·0.25(C_7H_8)
M_r	748.14	618.32
Crystal system, space group	Hexagonal, $P6_3/m$	Triclinic, $P\bar{1}$
Temperature (K)	173	173
a, b, c (Å)	12.6858(8), 12.6858(8), 14.3160(19)	13.4369(8), 15.3305(9), 16.2651(10)
α, β, γ (°)	90, 90, 120	93.335(5), 104.594(5), 95.069(5)
V (Å^3)	1995.2(4)	3218.5 (3)
Z	2	4
F(000)	792	1290
D_x (Mg m^{-3})	1.245	1.276
Radiation type	Mo $K\alpha$	Mo $K\alpha$
μ (mm^{-1})	0.16	0.07
Crystal shape	Needle	Rhombic prism
Color	Colorless	Yellow
Crystal size (mm)	0.54 × 0.06 × 0.05	0.17 × 0.12 × 0.11
Absorption correction	Multi-scan	Multi-scan
T_{min}, T_{max}	0.242, 1.000	0.974, 1.000
No. of measured, independent and observed [$I > 2s(I)$] reflections	10894, 999, 693	26853, 13478, 9200
R_{int}	0.284	0.061
Θ_{max} (°)	23.2	26.7
Range of h, k, l	h = –14→14, k = –14→14, l = –15→14	h = –17→17, k = –19→19, l = –20→20
$R[F^2 > 2s(F^2)]$, $wR(F^2)$, S	0.063, 0.166, 1.00	0.056, 0.151, 1.02
No. of reflections	999	13478
No. of parameters	93	899
$\Delta\rho_{max}$, $\Delta\rho_{min}$ (e Å^{-3})	0.35, –0.34	0.29, –0.26

Computer programs: *X-AREA* (*Stoe & Cie*, 2001), *CrysAlis PRO* 1.171.42.43a (*Rigaku OD*, 2022), *SHELXS* (G. M. Sheldrick, 1997), *SHELXT* (G. M. Sheldrick, 2015), *SHELXL2018*/3 (Sheldrick, 2018).

Table S5. Selected crystallographic data for **7**·0.5(C_6H_6) and **8**·2($CHCl_3$).

	7·0.5(C_6H_6)	**8**·2($CHCl_3$)
Chemical formula	$C_{42}H_{25}B_2N_3$·0.5(C_6H_6)	$C_{51}H_{36}B_3N_3$·2($CHCl_3$)
M_r	632.32	961.99
Crystal system, space group	Triclinic, $P\bar{1}$	Triclinic, $P\bar{1}$
Temperature (K)	100	100
a, *b*, *c* (Å)	12.53928(10), 13.09723(10), 20.87428(18)	12.7063(9), 13.7794(11), 15.4494(12)
α, β, γ (°)	104.8782(7), 102.0676(7), 103.7954(7)	114.175(8), 101.129(6), 103.186(7)
V (Å^3)	3081.36(5)	2274.3(3)
Z	4	2
F(000)	1316	1416
D_x (Mg m^{-3})	1.363	1.182
Radiation type	Synchrotron, DESY P24 beamline, λ = 0.500 Å	Synchrotron, DESY P24 beamline, λ = 0.5 Å
μ (mm^{-1})	0.04	0.16
Crystal shape	Plate	Elongated prism
Color	Yellow	Brownish yellow
Crystal size (mm)	0.25 × 0.20 × 0.10	0.39 × 0.08 × 0.05
Absorption correction	Multi-scan	Multi-scan
T_{min}, T_{max}	0.959, 1.000	0.855, 1.000
No. of measured, independent and observed [$I > 2s(I)$] reflections	120579, 22259, 19883	46742, 8606, 7127
R_{int}	0.058	0.034
Θ_{max} (°)	22.6	18.0
Range of *h*, *k*, *l*	*h* = –19→19, *k* = –19→19, *l* = –32→32	*h* = –15→15, *k* = –17→17, *l* = –19→19
$R[F^2 > 2s(F^2)]$, $wR(F^2)$, *S*	0.045, 0.135, 1.06	0.080, 0.247, 1.06
No. of reflections	22259	8606
No. of parameters	902	616
$\Delta\rho_{max}$, $\Delta\rho_{min}$ (e Å^{-3})	0.49, –0.69	1.21, –0.71

Computer programs: *X-AREA* (*Stoe & Cie*, 2001), *CrysAlis PRO* 1.171.42.43a (*Rigaku OD*, 2022), *SHELXS* (G. M. Sheldrick, 1997), *SHELXT* (G. M. Sheldrick, 2015), *SHELXL2018*/3 (Sheldrick, 2018).

Table S6. Selected crystallographic data for $\mathbf{9^{Mes}}\cdot 4(CH_3CN)$.

	$\mathbf{9^{Mes}}\cdot 4(CH_3CN)$
Chemical formula	$C_{69}H_{60}B_3N_3\cdot 4(C_2H_3N)$
M_r	1127.84
Crystal system, space group	Monoclinic, *C*2/*c*
Temperature (K)	173
a, *b*, *c* (Å)	23.3411(13), 16.5921(5), 18.8439(9)
α, β, γ (°)	90, 113.996(5), 90
V (Å^3)	6667.1(6)
Z	4
F(000)	2392
D_x (Mg m^{-3})	1.124
Radiation type	Mo *K*α
μ (mm^{-1})	0.07
Crystal shape	Block
Color	Colorless
Crystal size (mm)	0.44 × 0.29 × 0.28
Absorption correction	Multi-scan
T_{min}, T_{max}	0.585, 1.000
No. of measured, independent and observed [$I > 2s(I)$] reflections	34526, 8962, 6279
R_{int}	0.058
Θ_{max} (°)	29.1
Range of *h*, *k*, *l*	*h* = –31→31, *k* = –22→22, *l* = –25→25
$R[F^2 > 2s(F^2)]$, $wR(F^2)$, *S*	0.058, 0.167, 1.03
No. of reflections	8962
No. of parameters	403
$\Delta\rho_{max}$, $\Delta\rho_{min}$ (e Å^{-3})	0.42, –0.26

Computer programs: *X-AREA* (*Stoe & Cie*, 2001), *CrysAlis PRO* 1.171.42.43a (*Rigaku OD*, 2022), *SHELXS* (G. M. Sheldrick, 1997), *SHELXT* (G. M. Sheldrick, 2015), *SHELXL2018*/3 (Sheldrick, 2018).

4.1. Single-crystal X-ray structure analysis of 1

Compound **1** crystallizes in two polymorphous modifications, denoted as α-**1** (denser) and β-**1** (less dense). Single crystals of both modifications, in the shape of elongated plates or planks, were selected from the same sample, and may therefore belong to the class of concomitant polymorphs. Both modifications crystallize in the monoclinic system, space groups $P2_1/c$ (α) and $C2/c$ (β). The crystallographically unique molecules lie in the general positions (Figure S59a,b). The geometry of the molecules in both modifications is almost the same (Figure S59c).

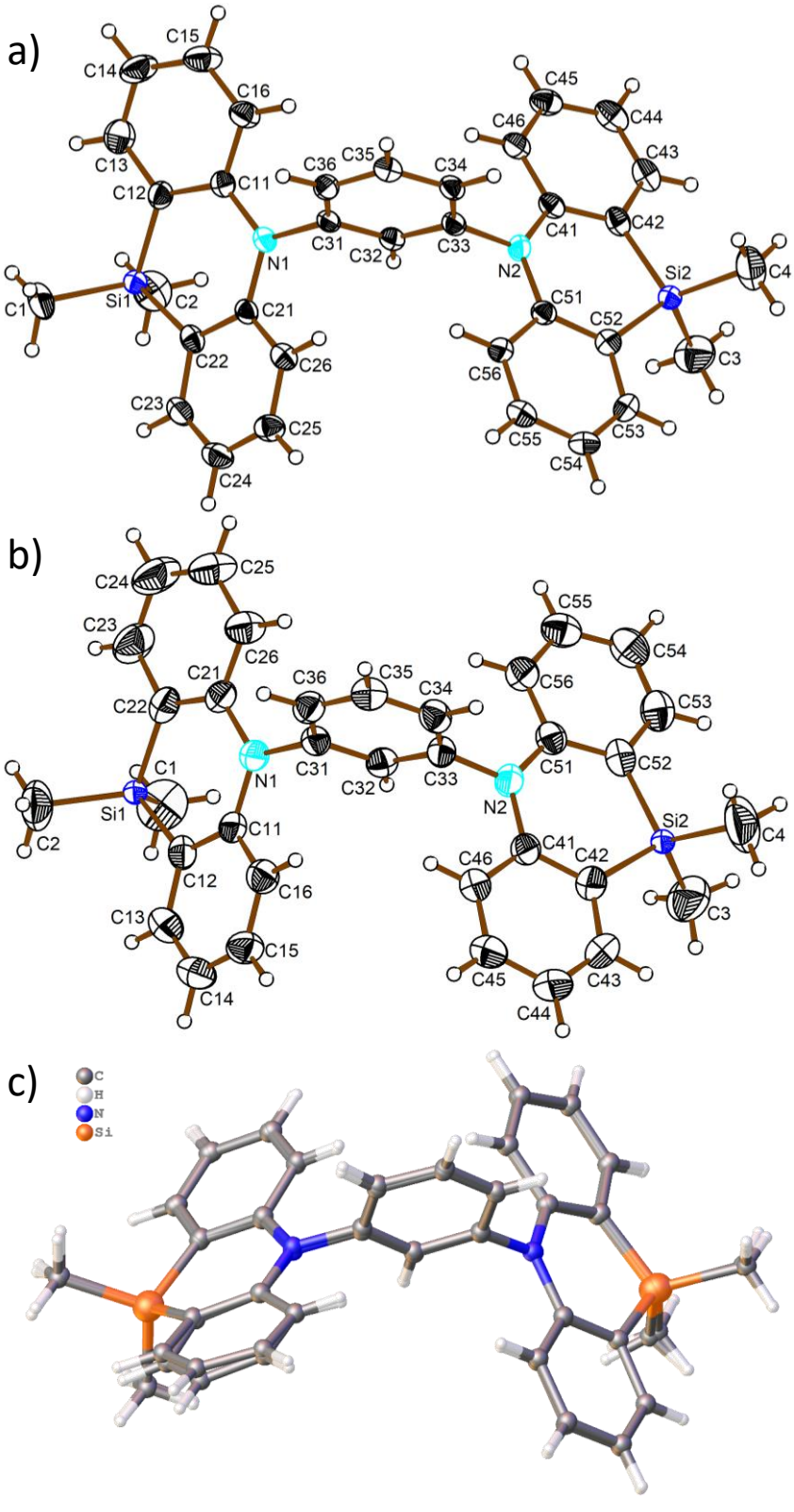

Figure S59. Molecular structure of **1** in the solid state in the (a) α- and (b) β-modification. Atomic displacement ellipsoids are drawn at the 50% probability level. (c) Overlay of the molecular structures of **1** in both polymorphous modifications. Selected dihedral angles for α-**1**: C(11)N(1)C(21)//C(32)C(31)C(36) = 71.65(19)°, C(41)N(2)C(51)//C(32)C(33)C(34) = 86.23(18)°, C(12)Si(1)C(22)//C(11)N(1)C(21) = 16.7(4)°, C(42)Si(2)C(52)//C(41)N(2)C(51) = 7.6(4)°. Selected dihedral angles for β-**1**: C(11)N(1)C(21)//C(32)C(31)C(36) = 69.8(2)°, C(41)N(2)C(51)//C(32)C(33)C(34) = 84.8(2)°, C(12)Si(1)C(22)//C(11)N(1)C(21) = 22.7(4)°, C(42)Si(2)C(52)//C(41)N(2)C(51) = 10.1(4)°.

4.2. Single-crystal X-ray structure analysis of 2^{Br}

Compound $\mathbf{2}^{Br}$ crystallizes in the triclinic space group *P*$\bar{1}$ (No. 2) with one crystallographically unique molecule in the general position (Figure S60).

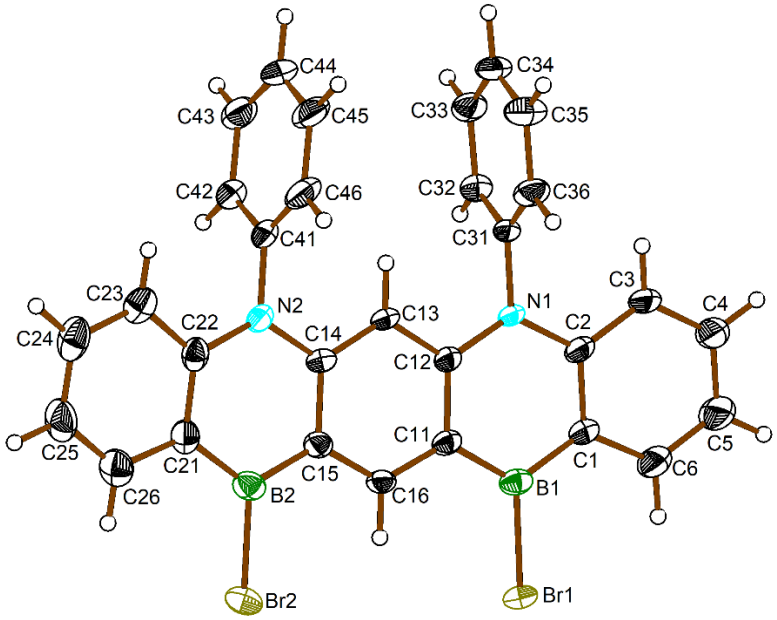

Figure S60. Molecular structure of $\mathbf{2}^{Br}$ in the solid state. Atomic displacement ellipsoids are drawn at the 50% probability level. Selected dihedral angles: C(1)B(1)C(11)//C(2)N(1)C(12) = 5.4(7)°, C(15)B(2)C(21)//C(14)N(2)C(22) = 3.4(8)°, C(1)C(2)C(3)C(4)C(5)C(6)//C(21)C(22)C(23)C(24)C(25)C(26) = 8.6(8)°.

4.3. Single-crystal X-ray structure analysis of 2^{Mes}

Compound $\mathbf{2}^{Mes}$ crystallizes in the monoclinic space group $P2_1/c$ (No. 14) with one crystallographically unique molecule in the general position (Figure S61). Due to a very low scattering ability of the crystals, the structure determination became possible only by using the high-flux synchrotron X-ray source (Table S3).

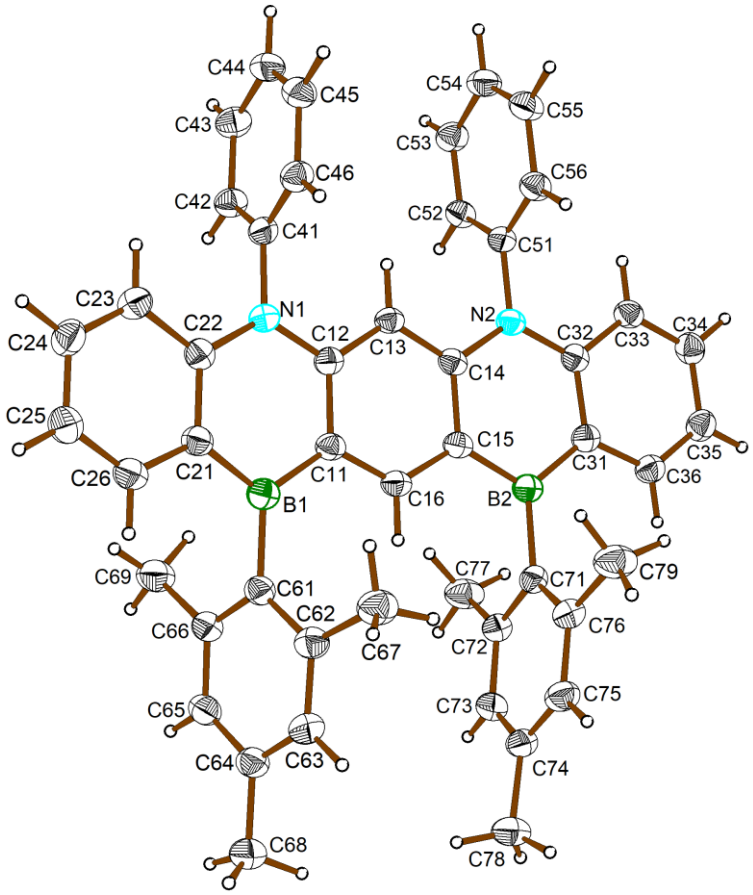

Figure S61. Molecular structure of $\mathbf{2}^{Mes}$ in the solid state. Atomic displacement ellipsoids are drawn at the 50% probability level. Selected dihedral angles: C(11)B(1)C(21)//C(12)N(1)C(22) = 7.68(5)°, C(15)B(2)C(31)//C(14)N(2)C(32) = 0.709(11)°, C(21)C(22)C(23)C(24)C(25)C(26)//C(31)C(32)C(33)C(34)C(35)C(36) = 8.874(11)°.

4.4. Single-crystal X-ray structure analysis of 5

Compound **5** crystallizes in the hexagonal space group $P6_3/m$ (No. 176) with one crystallographically unique molecule at the inversion center belonging to the crystallographic $\bar{6}$ axis with the mirror plane passing through the atoms Si(1), N(1), C(7), C(8), C(9), and C(10) (Figure S62). Therefore, the point symmetry of the molecule in the crystal is C_{3h}, resulting in the asymmetric unit comprising only 12 non-H atoms. The H atoms at the methyl groups C(9) and C(10) are disordered over two positions by mirror reflection.

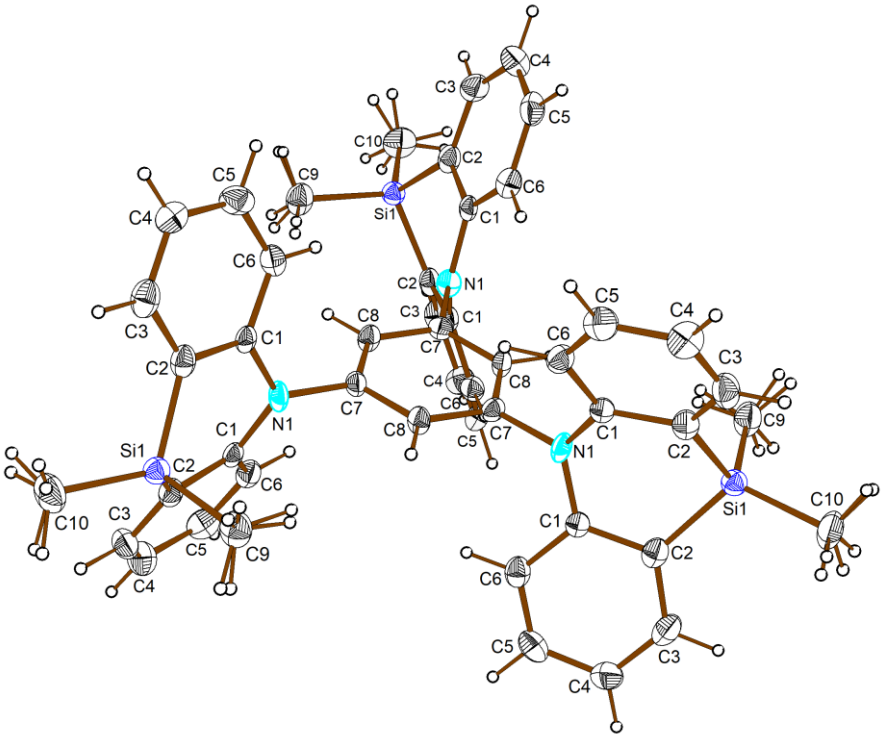

Figure S62. Molecular structure of **5** in the solid state. Atomic displacement ellipsoids are drawn at the 50% probability level. Selected dihedral angles: C(2)Si(1)C(2')//C(1)N(1)C(1') = 65.0(4)°.

4.5. Single-crystal X-ray structure analysis of 6·0.25(toluene)

Compound **6** crystallizes with 0.25 toluene solvate molecules in the triclinic space group $P\bar{1}$ (No. 2). Both crystallographically unique molecules lie in general positions (Figure S63a). Their geometrical parameters are similar (Figure S63b). In addition, a partly occupied toluene molecule also lies in the general position. Its site occupancy factor was fixed at the refined value of 0.5.

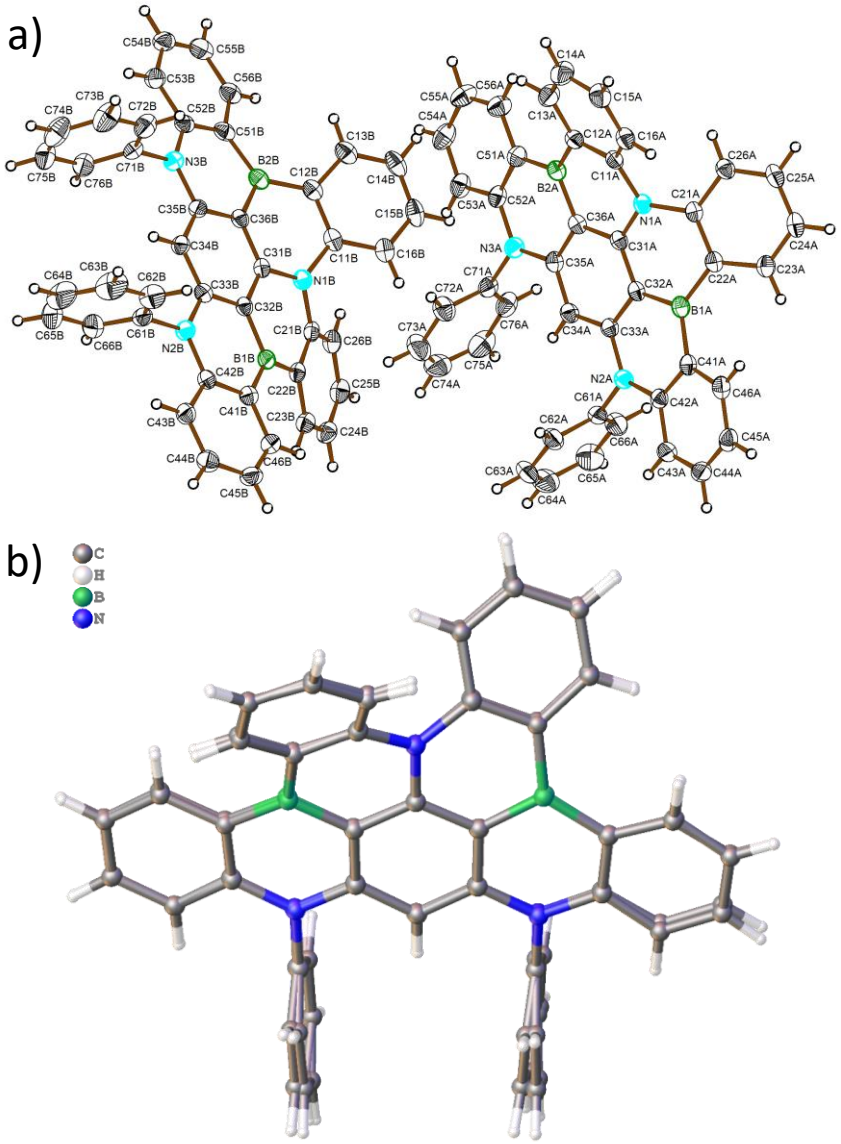

Figure S63. (a) Molecular structures of the two crystallographically unique molecules of **6**·0.25(toluene) in the solid state. The toluene molecule is omitted for clarity. Atomic displacement ellipsoids are drawn at the 50% probability level. (b) Overlay of the two crystallographically unique molecules of **6**·0.25(toluene). Selected dihedral angles for the molecule denoted with A [corresponding values for the molecule denoted with B]: C(41A)C(42A)C(43A)C(44A)C(45A)C(46A)//C(51A)C(52A)C(53A)C(54A)C(55A)C(56A) = 4.55(12)° [7.01(12)°], C(11A)C(12A)C(13A)C(14A)C(15A)C(16A)//C(51A)C(52A)C(53A)C(54A)C(55A)C(56A) = 29.45(8)° [30.73(9)°], C(21A)C(22A)C(23A)C(24A)C(25A)C(26A)//C(41A)C(42A)C(43A)C(44A)C(45A)C(46A) = 29.37(8)° [33.86(8)°], C(11A)C(12A)C(13A)C(14A)C(15A)C(16A)//C(21A)C(22A)C(23A)C(24A)C(25A)C(26A) = 48.97(7)° [50.75(7)°].

4.6. Single-crystal X-ray structure analysis of 7·0.5(C_6H_6)

Compound **7** crystallizes as a C_6H_6 solvate in the triclinic space group *P*$\bar{1}$ (No. 2) with two crystallographically unique molecules in general positions (Figure S64). Two unique C_6H_6 molecules lie in the inversion centers resulting in 0.5 C_6H_6 per one **7** in the formula unit. Due to a low scattering ability of the crystals, the structure determination became possible only by using the high-flux synchrotron source (Table S5).

In the crystal, pairs of molecules demonstrate π-π-stacking interaction. The distance between atom N(1) of one molecule and the best plane passing through N(4), C(76), C(92), and C(102) of another one is 3.39 Å.

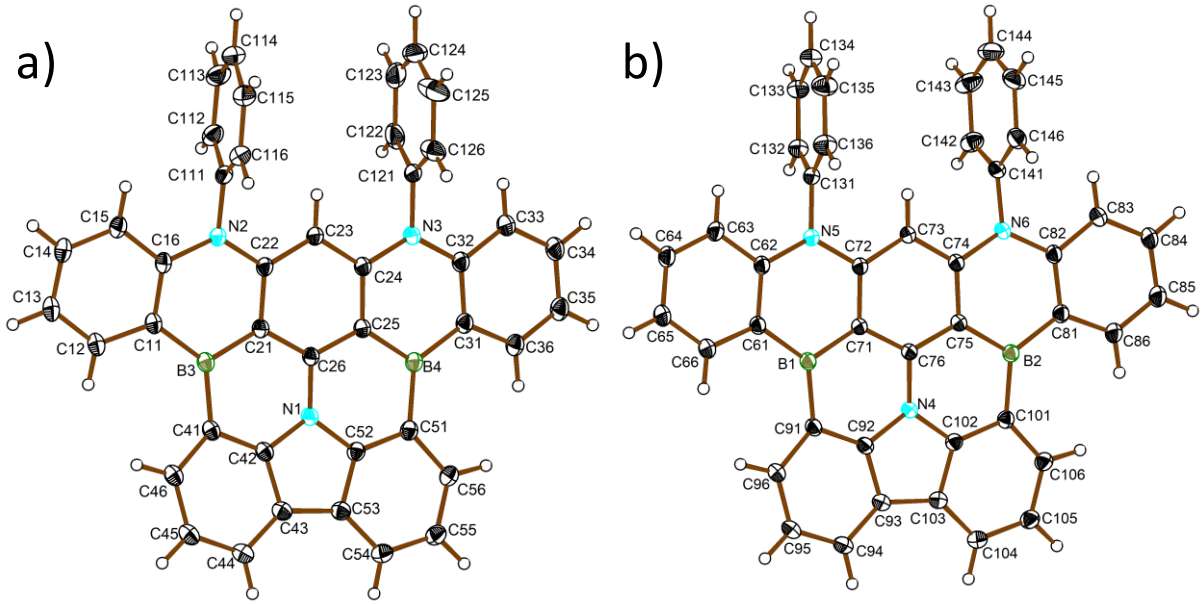

Figure S64. (a), (b) Molecular structures of two crystallographically unique molecules of **7**·0.5(C_6H_6) in the solid state. The C_6H_6 molecule is omitted for clarity. Atomic displacement ellipsoids are drawn at the 50% probability level. Selected dihedral angles:
C(11)C(12)C(13)C(14)C(15)C(16)//C(31)C(32)C(33)C(34)C(35)C(36) = 13.98(4)°,
C(61)C(62)C(63)C(64)C(65)C(66)//C(81)C(82)C(83)C(84)C(85)C(86) = 4.10(5)°,
C(11)C(12)C(13)C(14)C(15)C(16)//C(41)C(42)C(43)C(44)C(45)C(46) = 17.99(4)°,
C(31)C(32)C(33)C(34)C(35)C(36)//C(51)C(52)C(53)C(54)C(55)C(56) = 9.17(5)°,
C(61)C(62)C(63)C(64)C(65)C(66)//C(91)C(92)C(93)C(94)C(95)C(96) = 3.66(5)°,
C(81)C(82)C(83)C(84)C(85)C(86)//C(101)C(102)C(103)C(104)C(105)C(106) = 3.43(5)°,
C(41)C(42)C(43)C(44)C(45)C(46)//C(51)C(52)C(53)C(54)C(55)C(56) = 1.87(5)°,
C(91)C(92)C(93)C(94)C(95)C(96)//C(101)C(102)C(103)C(104)C(105)C(106) = 2.89(5)°.

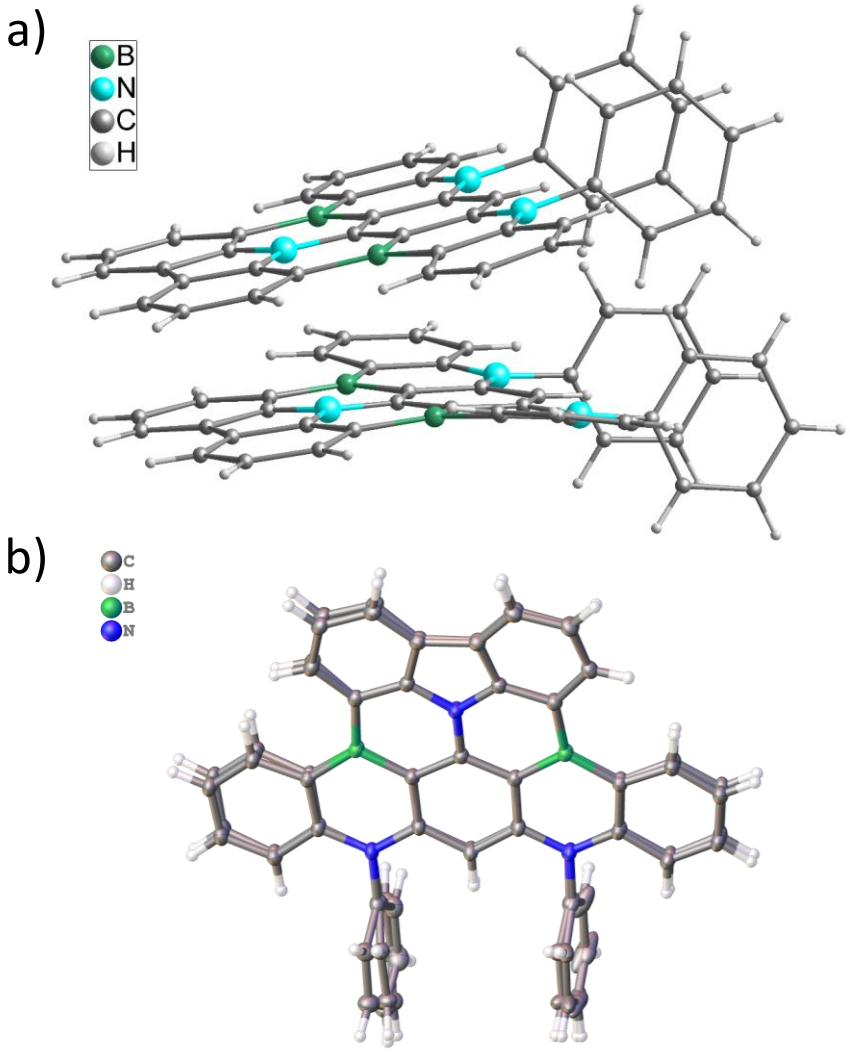

Figure S65. (a) Mutual arrangement of the two crystallographically unique molecules of **7**·0.5(C_6H_6) in the crystal. (b) Overlay of the molecular structures of the two crystallographically unique molecules of **7**·0.5(C_6H_6).

4.7. Single-crystal X-ray structure analysis of 8·2($CHCl_3$)

Compound **8** crystallizes with two $CHCl_3$ solvate molecules in the triclinic space group *P*$\bar{1}$ (No. 2). The only crystallographically unique molecule lies in the general position (Figure S66). One of two unique $CHCl_3$ molecules is disordered over two positions with the relative weight refined as 55:45%. It seems that all crystals are twinned to different degrees. First, we measured the diffraction on the laboratory diffractometer and then on the synchrotron (Table S5). Nevertheless, our attempts to separate domains during the integration of frames failed, even having the data from the very low divergent high-brilliance synchrotron source. However, in the latter case, the effect of minor domain(s) was rather small, resulting in non-perfect but quite appropriate R-values (Table S5).

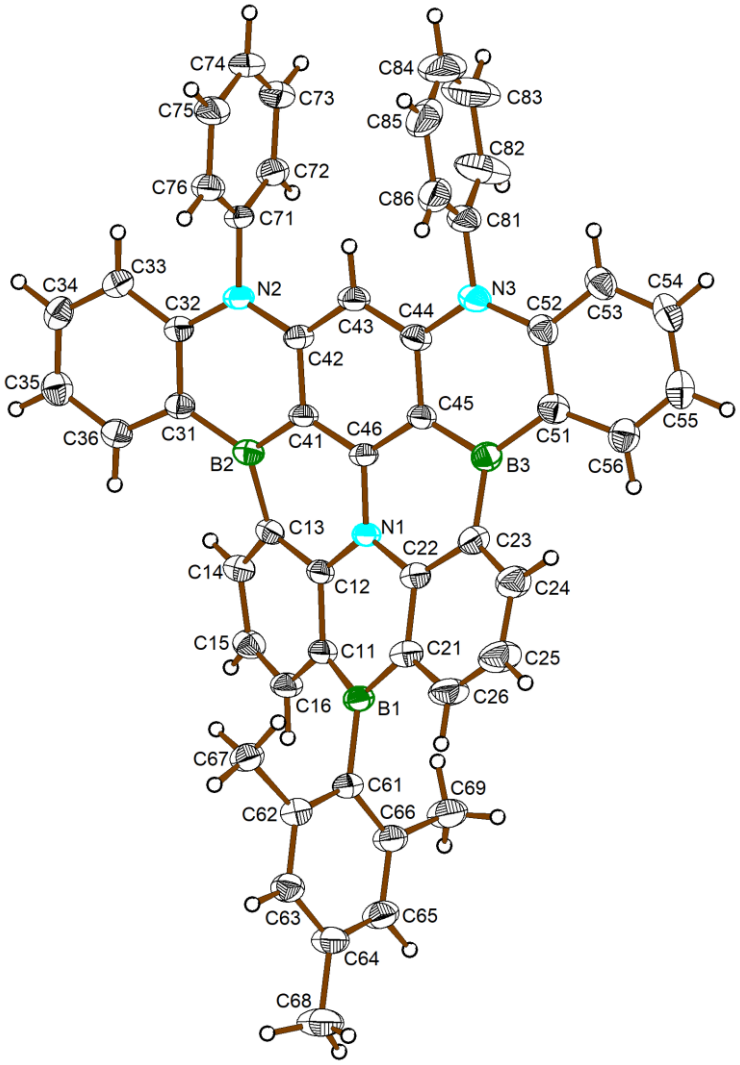

Figure S66. Molecular structure of **8**·2($CHCl_3$) in the solid state. The $CHCl_3$ molecules are omitted for clarity. Atomic displacement ellipsoids are drawn at the 50% probability level. Selected dihedral angles: C(31)C(32)C(33)C(34)C(35)C(36)//C(51)C(52)C(53)C(54)C(55)C(56) = 10.5(2)°, C(11)C(12)C(13)C(14)C(15)C(16)//C(31)C(32)C(33)C(34)C(35)C(36) = 28.10(14)°, C(21)C(22)C(23)C(24)C(25)C(26)//C(51)C(52)C(53)C(54)C(55)C(56) = 29.92(17)°, C(11)C(12)C(13)C(14)C(15)C(16)//C(21)C(22)C(23)C(24)C(25)C(26) = 23.57(15)°.

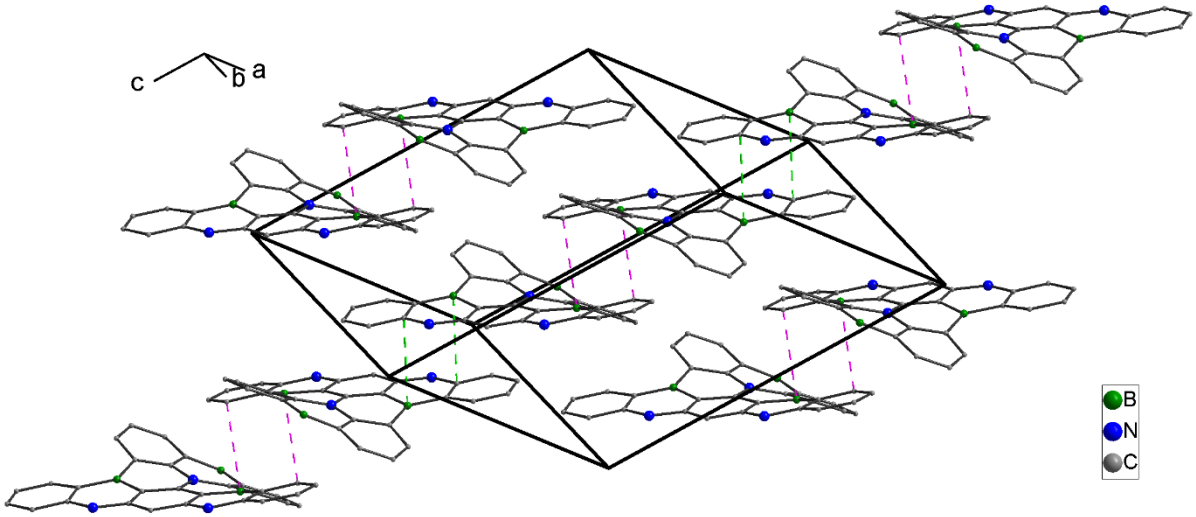

Figure S67. Section of the crystal lattice showing the stacking interactions in **8**·2($CHCl_3$). The short intradimer contacts are represented by pink dashed lines (see main text). The longer interdimer contacts are represented by green dashed lines; if these are calculated between atom B(2) of dimer I and the C(31)-to-C(36) plane of dimer II, the corresponding values are 3.631(3) Å. Since there is no big off-set for the weaker stacking, one can alternatively consider the bigger conjugated system involving {C(31)-to-C(36) and N(2) and B(2) and C(41)-to-C(46)} of dimer II (root-mean-square deviation of atoms from the best plane through these atoms: 0.067 Å). For this bigger conjugated system, the interdimer distance is 3.610(3) Å. All H atoms as well as the Mes and Ph substituents are omitted for clarity.

4.8. Single-crystal X-ray structure analysis of 9^{Mes}·4(CH_3CN)

Compound $\mathbf{9^{Mes}}$ crystallizes with four non-coordinating CH_3CN solvate molecules in the monoclinic space group *C*2/*c* (No. 15). The only crystallographically unique molecule lies at the 2-fold axis passing through the C(41)···C(66) line (Figure S68).

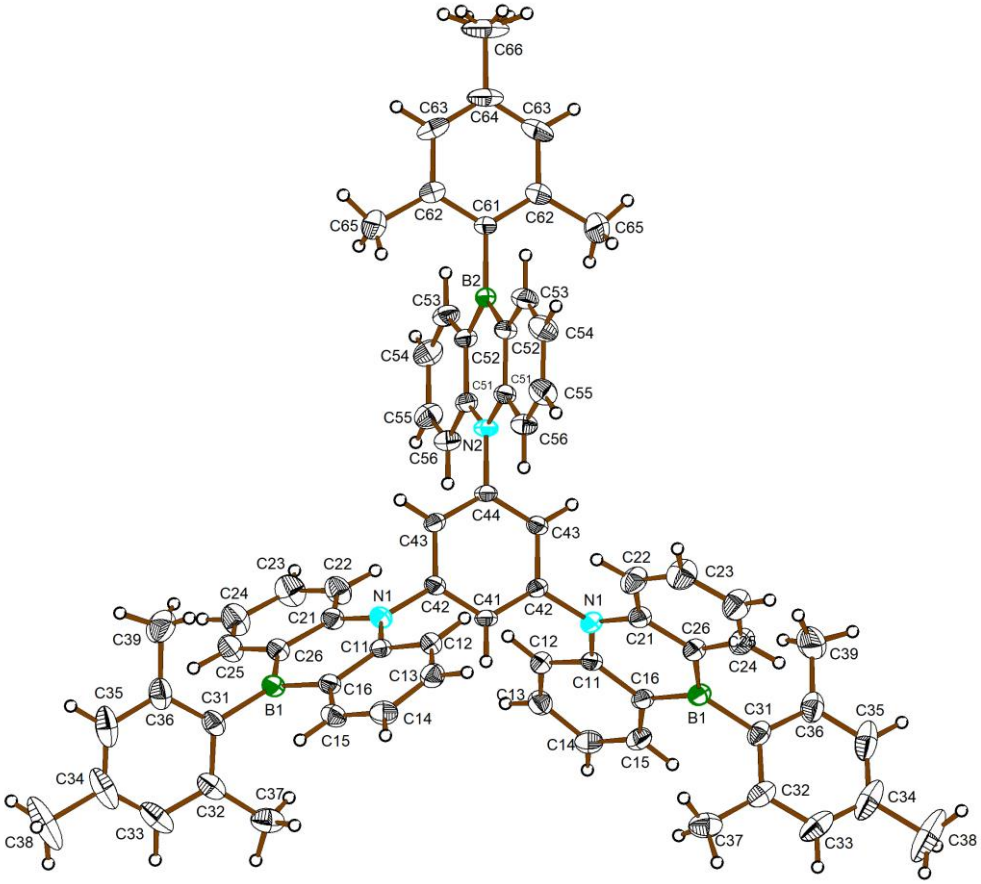

Figure S68. Molecular structure of $\mathbf{9^{Mes}}$·4(CH_3CN) in the solid state. The CH_3CN molecules are omitted for clarity. Atomic displacement ellipsoids are drawn at the 50% probability level. Selected dihedral angles: C(11)N(1)C(21)//C(41)C(42)C(43) = 70.73(11)°, C(51)N(2)C(51')//C(43)C(44)C(43') = 89.38(8)°, C(16)B(1)C(26)//C(11)N(1)C(21) = 3.2(3)°, C(52)B(2)C(52')//C(51)N(2)C(51') = 0.19(15)°.

5. Computational details

5.1. Corrected free energy values for computed structures of 2^{Br} and 3^{Br}

The DFT calculations for the free energy values of **2^{Br}** and **3^{Br}** were performed using *Gaussian 16*, *Revision B.01*.[S16] Geometry optimizations and frequency calculations were performed at the *ω*B97XD[S17]/def2-SVP[S18] level of theory, including implicit solvation by the solvent model based on density (SMD; solvent = C_6H_6).[S19] Harmonic vibrational frequency calculations confirmed that the optimized geometries correspond to minimum energy structures since no imaginary frequencies were found. Single-point calculations for free energy values were performed at the SMD(C_6H_6)/*ω*B97XD/def2-TZVP[S18] level of theory. Graphical representations of molecular geometries were produced with *Avogadro 1.1.1* and *POV-Ray 3.7.0*.

2^{Br}

$G_{298,corr}$ =–6462.71499593 Hartree

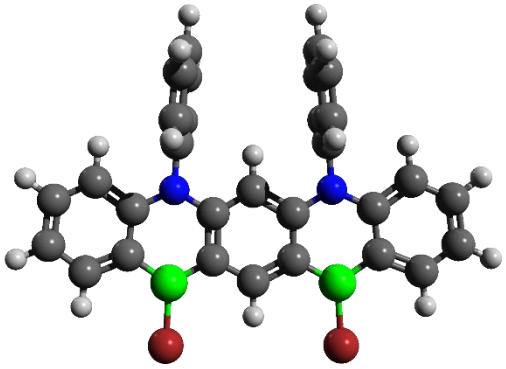

3^{Br}

$G_{298,corr}$ =–6462.70816335 Hartree

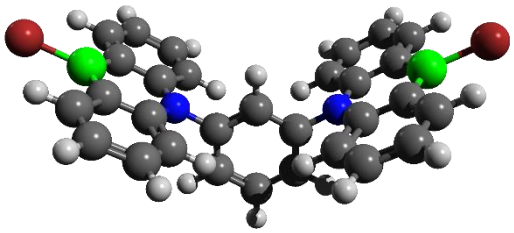

5.2. Characterization of the optoelectronic properties of compounds 6, 7, 8, and 2^{Mes}

The ground and the first singlet and triplet excited states of **6**, **7**, **8**, and **2^{Mes}** compounds were optimized by using the second-order algebraic-diagrammatic construction in combination with a spin-component scaling correction (SCS-ADC(2))[S20,S21] method and the def2-SVP basis set.[S18] Note that the ADC(2) reduces to MP2 (second-order Møller-Plesset perturbation theory)[S22] for the ground-state geometry optimization. Singlet and triplet vertical excitation energies calculation on top of the SCS-ADC(2) optimized structures was carried out at the same level of theory employed for the geometry optimization procedure, i.e., SCS-ADC(2)/def2-SVP. All these calculations were performed using Turbomole 7.5.[S23] The $S_1 \rightarrow T_1$ and $S_1 \rightarrow T_2$ spin-orbit coupling (SOC) values were estimated resorting to the time-dependent density functional theory (TD-DFT) within the Tamm-Dancoff (TDA) approach.[S24] using a Breit-Pauli Hamiltonian within the ZORA approximation, as implemented in Orca 5.0.4.[S25]

The simulation of the vibrationally-resolved electronic absorption and emission spectra were carried out at room temperature (300 K) using Fcclasses3.3,[S26] and the overlap between the vibrational wavefunctions were computed using the vertical Hessian (VH) multidimensional harmonic oscillator approximation neglecting the contribution of normal modes associated with torsion angles of the substituents.[S27] We neglected the contribution of the normal modes associated with the torsion angles of the substituents since the S_1 excited states of all compounds are primarily localized on the core and not on the substituents. Both ground and S_1 minima were reoptimized at DFT and TD-DFT, respectively using the PBE0 functional with the def2-SVP basis set within the Gaussian 16[S28] package, verifying that

all harmonic vibrational frequencies are positive. The adiabatic energy between the ground and S_1 states was refined at the SCS-ADC(2)/def2-SVP level.

The electron density variation (ρ) upon the excitation is quantified as the difference between the electronic density in the ground and in the excited state. This electron density variation can be split into positive (ρ_+) and negative (ρ_-) contributions. The absolute transferred charge (q_{CT}) can be computed as the integral of the ρ_+ or ρ_- over the whole space as follows:

$$q_{CT} = \int \rho_+(\boldsymbol{r})d\boldsymbol{r} = \left|\int \rho_-(\boldsymbol{r})d\boldsymbol{r}\right|$$

The charge transfer distance (d_{CT}) is computed as the norm of the vector difference between the barycenter of positive ($\mathbf{R}_+$) and negative ($\mathbf{R}_-$) parts of ρ:

$$d_{CT} = \sqrt{D_x^2 + D_y^2 + D_z^2}$$

in which,

$$D_i = \left|R_{+,i} - R_{-,i}\right| = \left|\frac{\int i\rho_+(\boldsymbol{r})d\boldsymbol{r}}{\int \rho_+(\boldsymbol{r})d\boldsymbol{r}} - \frac{\int i\rho_-(\boldsymbol{r})d\boldsymbol{r}}{\int \rho_-(\boldsymbol{r})d\boldsymbol{r}}\right| \qquad (i = x, y, z)$$

The simulation of the vibronically-resolved emission spectra has been carried out within the displaced undistorted harmonic oscillator model, neglecting the Duschinsky rotation and assuming equal frequencies and normal modes for the ground- and excited-state. Within the Thermal Vibration Correlation Function formalism, the emission cross-section in time-domain can be written as follows:

$$\sigma(\omega)_{i\to f}^{FC} = \frac{2\omega^3}{3\pi\hbar c^3}\left|\vec{\mu}_{if}^{0}\right|^2 \int_{-\infty}^{+\infty} d\tau\ exp(iE_{if}\tau)Z^{-1}\rho_{if}^{FC}(t,T)$$

in which the superscript "FC" means that the calculation of the emission cross-section is carried out within the Frank-Condon approximation, $\vec{\mu}_{if}^{0}$ is the electronic transition dipole moment obtained for the (undistorted) optimized S_1 geometry, E_{if} is the energy gap between the initial and final electronic state, Z is the partition function and ρ_{if}^{FC} is the thermal vibration correlation function defined as:

$$\rho_{if}^{FC}(t,T) = Tr[exp\left(-i\varepsilon_{f,v_f}\tau_f\right)exp\left(-i\varepsilon_{i,v_i}\tau_i\right)]$$

in which ε_{f,v_f} and ε_{i,v_i} is the vibrational level associated with the final and initial state, respectively, $\tau_f = t/\hbar$ and $\tau_i = -\tau_f - \beta$, where $\beta = (k_B T)^{-1}$.

The simulation of the spectra has been carried out at T = 300 K. The Huang-Rhys factors are defined as:

$$S_k = \frac{1}{2}\left\{\sqrt{\frac{\omega_k}{\hbar}}\left[X_i - X_f\right]\boldsymbol{M}^{\frac{1}{2}}\boldsymbol{L}_k(f)\right\}^2$$

in which ω_k is the vibrational frequency of the k-th normal mode, X_i and X_f are the Cartesian coordinates of the equilibrium geometry of state state i and f, $\boldsymbol{M}$ is the diagonal matrix whose elements are the atomic masses, $\boldsymbol{L}_k(f)$ is the vector containing the normal coordinates written in terms of mass-weighted Cartesian coordinates of the final state. The projection of the geometry displacement has been carried out on the ground-state vibrational normal modes computed at the PBE0/6-31G(d,p) level of theory. The reorganization energies (λ) were also estimated by summing the contribution of each individual normal mode (λ_{ij}) that within the harmonic approximation reads as:

$$\lambda_{ij} = \hbar\omega_{ij}S_j$$

In which, S_j is the Huang-Rhys factor that in simple words represents the projection of the geometry displacement between the states i and j along the j-th normal model and expressed as follow:

$$S_j = \frac{1}{2}\left\{\sqrt{\frac{\omega_j}{\hbar}}\left[X_f - X_i\right]M^{\frac{1}{2}}L_j(f)\right\}^2$$

where ω_j is the vibrational frequency of the j-th normal mode, X_i and X_j are the Cartesian coordinates of the equilibrium geometry of initial and final states, respectively, M is the diagonal matrix containing the atomic masses, and $L_j(f)$ is the vector including the normal coordinates written in function of mass weighted Cartesian coordinates of the final state.

5.2.1. HOMO and LUMO energies

Table S7. HOMO and LUMO energies (eV) computed at the PBE0/def2-SVP level.

Molecule	HOMO	LUMO
6	–5.30	–1.67
7	–5.44	–1.77
8	–5.55	–1.94
2^{Mes}	–5.73	–1.40

5.2.2. Vertical excitation energies and canonical molecular orbitals

Table S8. Vertical excitation energies (ΔE in eV), wavelength (λ in nm), oscillator strength (f), and the molecular orbitals that best describe the electronic transition of the low-lying singlet and triplet excited states with their respective weight in parenthesis.

Molecule	State	ΔE [eV]	λ [nm]	f	Contribution
6	S_1	3.31	375	0.106	HOMO→LUMO (71%)
	T_1	3.25	381		HOMO→LUMO+1 (85%)
	T_2	3.32	373		HOMO→LUMO (85%)
7	S_1	3.28	378	0.184	HOMO→LUMO (88%)
	T_1	3.13	396		HOMO→LUMO (84%)
	T_2	3.27	379		HOMO-2→LUMO (34%) HOMO-1→LUMO (28%)
8	S_1	3.22	385	0.289	HOMO→LUMO (84%)
	T_1	3.10	400		HOMO→LUMO (81%)
	T_2	3.38	367		HOMO-1→LUMO (54%)
2^{Mes}	S_1	3.47	357	0.106	HOMO→LUMO (84%)
	T_1	3.20	388		HOMO→LUMO (83%)
	T_2	3.48	356		HOMO-1→LUMO (73%)

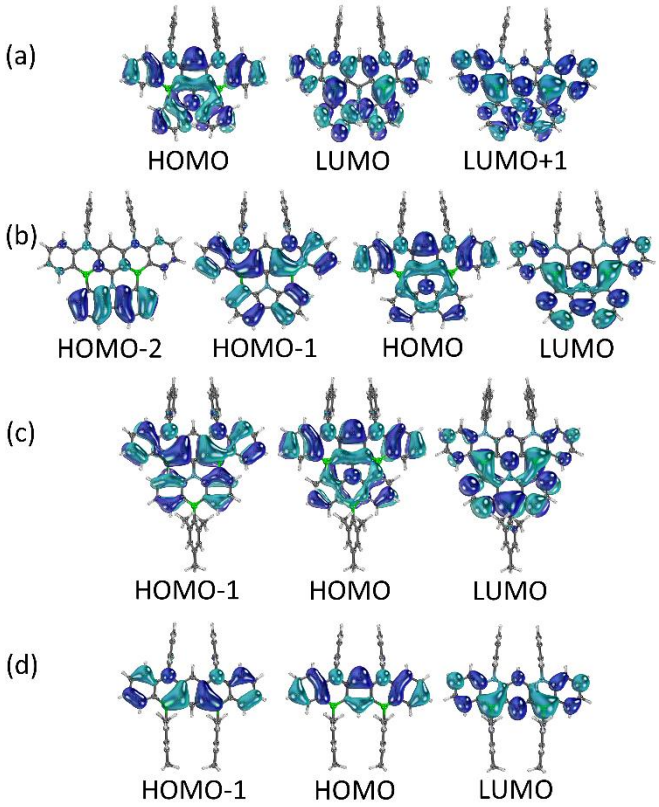

Figure S69. Shape of the canonical molecular orbitals that describe the lower singlet and triplet excited states of (a) **6**, (b) **7**, (c) **8**, and (d) $\mathbf{2^{Mes}}$.

Table S9. Transferred charge (q_{CT} in atomic unit) between the positive (ρ_+) and negative (ρ_-) electronic density and the charge transfer length (d_{CT} in angstrom).

Molecule	State	q_{CT}	d_{CT}
6	S_1	0.640	0.800
	T_1	0.613	0.795
	T_2	0.348	0.911
7	S_1	0.521	2.353
	T_1	0.590	1.858
	T_2	0.574	0.246
8	S_1	0.653	2.450
	T_1	0.641	2.129
	T_2	0.575	2.187
$\mathbf{2^{Mes}}$	S_1	0.682	1.850
	T_1	0.641	1.628
	T_2	0.575	1.313

5.2.3. Adiabatic energies

Table S10. Adiabatic S_1 and T_1 energies with respect to the ground-state optimized structure. The adiabatic singlet-triplet energy gap (ΔE_{ST}) is also reported. All energies are in eV.

Molecule	$(S_1)_{min}$	$(T_1)_{min}$	ΔE_{ST}
6	3.28	3.08	0.20
7	3.20	3.05	0.15
8	3.15	3.03	0.12
$\mathbf{2}^{Mes}$	3.39	3.05	0.34

5.2.4. Spin-orbit coupling

Table S11. Spin-orbit coupling between S_1 and T_1 and S_1 and T_2 computed at the TDA-PBE0/def2-SVP level. The values are reported in cm^{-1}.

SOC	**6**	**7**	**8**	$\mathbf{2}^{Mes}$
$S_1 \rightarrow T_1$	0.662	0.051	0.062	0.054
$S_1 \rightarrow T_2$	0.194	0.083	0.794	0.059

5.2.5. Simulated absorption and emission spectra

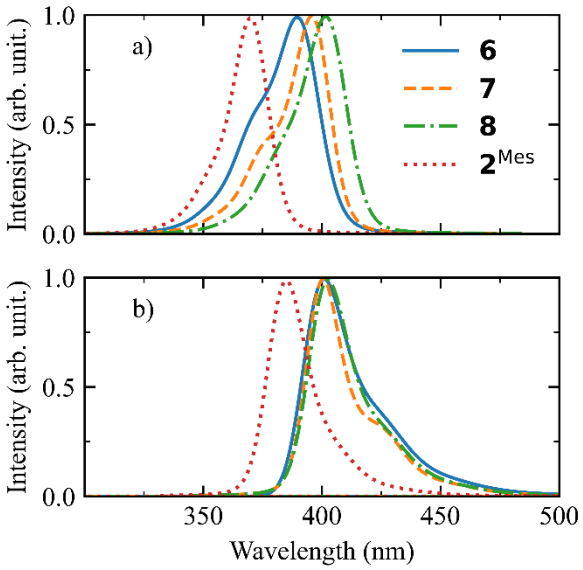

Figure S70. Simulated vibronically-resolved (a) absorption and (b) emission spectra using the vertical energy between the S_1 and S_0 states computed at the SCS-ADC(2)/def2-SVP level and harmonic frequencies computed at the TDA-PBE0/def2-SVP level.

5.2.6. Reorganization energy and Huang Rhys factors

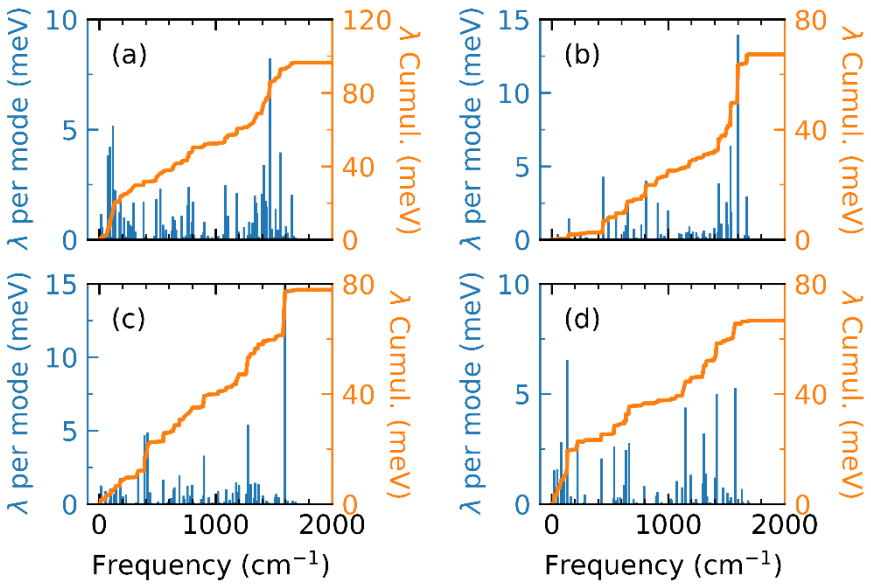

Figure S71. Reorganization energy per mode and cumulative reorganization energy in meV for the S_1 state in function of the frequency in cm^{-1} for (a) **6**, (b) **7**, (c) **8** and (d) **2^{Mes}**.

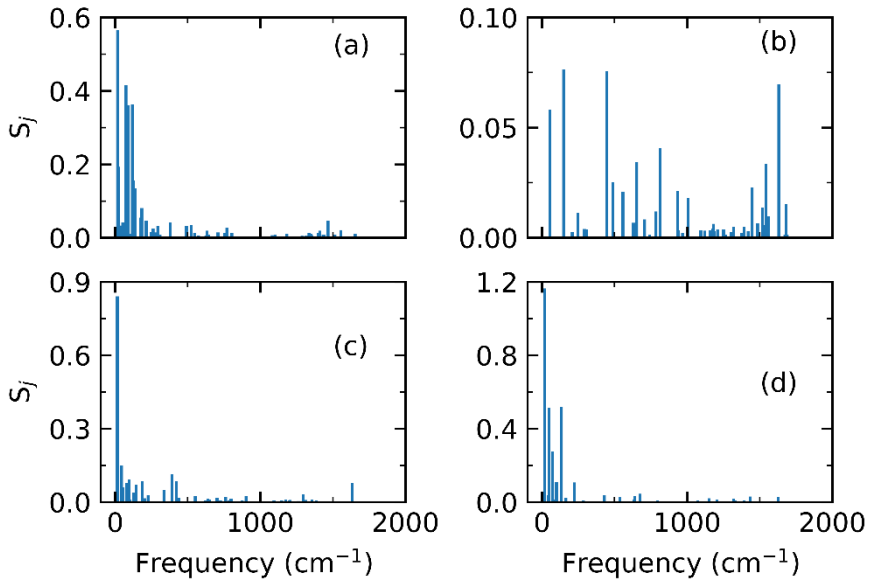

Figure S72. Huang-Rhys factor magnitude as a function of the harmonic vibrational normal mode computed for the S_1 state for (a) **6**, (b) **7**, (c) **8** and (d) **2^{Mes}**.

6. References

S1 E. Zender, S. Karger, R. Neubaur, A. Virovets, H.-W. Lerner and M. Wagner, *Org. Lett.*, 2024, **26**, 939–944.

S2 C. Li, S. K. Mellerup, X. Wang and S. Wang, *Organometallics*, 2018, **37**, 3360–3367.

S3 J. J. Dunsford, E. R. Clark and M. J. Ingleson, *Angew. Chem. Int. Ed.*, 2015, **54**, 5688–5692.

S4 A. Hübner, T. Bernert, I. Sänger, E. Alig, M. Bolte, L. Fink, M. Wagner and H.-W. Lerner, *Dalton Trans.*, 2010, **39**, 7528–7533.

S5 G. R. Fulmer, A. J. M. Miller, N. H. Sherden, H. E. Gottlieb, A. Nudelman, B. M. Stoltz, J. E. Bercaw and K. I. Goldberg, *Organometallics*, 2010, **29**, 2176–2179.

S6 A. M. Brouwer, *Pure Appl. Chem.*, 2011, **83**, 2213–2228.

S7 K. Suzuki, A. Kobayashi, S. Kaneko, K. Takehira, T. Yoshihara, H. Ishida, Y. Shiina, S. Oishi and S. Tobita, *Phys. Chem. Chem. Phys.*, 2009, **11**, 9850–9860.

S8 Y. Hirai and Y. Uozumi, *Chem. Asian J.*, 2010, **5**, 1788–1795.

S9 T. Hatakeyama, A. Mizutani and T. Koike, WO2017188111A1, 2017.

S10 W. C. Lewis and B. E. Norcross, *J. Org. Chem.*, 1965, **30**, 2866–2867.

S11 S. Duttwyler, A. M. Butterfield and J. S. Siegel, *J. Org. Chem.*, 2013, **78**, 2134–2138.

S12 Y. Wang, Y. Duan, R. Guo, S. Ye, K. Di, W. Zhang, S. Zhuang and L. Wang, *Org. Electron.*, 2021, **97**, 106275.

S13 As an alternative to the scale of –5.1 eV for 0.0 V vs FcH/FcH^+, a –5.39 eV scale is also considered appropriate, while the commonly used –4.8 eV scale has been questioned in recent literature. Since both values of –5.1 and –5.39 eV are "based on calculations that neglect solvent and supporting electrolyte effects, […] orbital energies obtained with different scales cannot be directly compared and researchers should state in their experimental procedures what parameters and assumptions are included in their calculations": C. M. Cardona, W. Li, A. E. Kaifer, D. Stockdale and G. C. Bazan, *Adv. Mater.*, 2011, **23**, 2367–2371.

S14 G. M. Sheldrick, *Acta Cryst.*, 2015, **A71**, 3–8.

S15 G. M. Sheldrick, *Acta Cryst.*, 2015, **C71**, 3–8.

S16 M. J. Frisch, G. W. Trucks, H. B. Schlegel, G. E. Scuseria, M. A. Robb, J. R. Cheeseman, G. Scalmani, V. Barone, G. A. Petersson, H. Nakatsuji, X. Li, M. Caricato, A. V. Marenich, J. Bloino, B. G. Janesko, R. Gomperts, B. Mennucci, H. P. Hratchian, J. V. Ortiz, A. F. Izmaylov, J. L. Sonnenberg, D. Williams-Young, F. Ding, F. Lipparini, F. Egidi, J. Goings, B. Peng, A. Petrone, T. Henderson, D. Ranasinghe, V. G. Zakrzewski, J. Gao, N. Rega, G. Zheng, W. Liang, M. Hada, M. Ehara, K. Toyota, R. Fukuda, J. Hasegawa, M. Ishida, T. Nakajima, Y. Honda, O. Kitao, H. Nakai, T. Vreven, K. Throssell, J. A. Montgomery, Jr., J. E. Peralta, F. Ogliaro, M. J. Bearpark, J. J. Heyd, E. N. Brothers, K. N. Kudin, V. N. Staroverov, T. A. Keith, R. Kobayashi, J. Normand, K. Raghavachari, A. P. Rendell, J. C. Burant, S. S. Iyengar, J. Tomasi, M. Cossi, J. M. Millam, M. Klene, C. Adamo, R. Cammi, J. W. Ochterski, R. L. Martin, K. Morokuma, O. Farkas, J. B. Foresman and D. J. Fox, *Gaussian 16*, *Revision B.01*, Gaussian, Inc., Wallingford CT, 2016.

S17 J.-D. Chai and M. Head-Gordon, *Phys. Chem. Chem. Phys.*, 2008, **10**, 6615–6620.

S18 F. Weigend and R. Ahlrichs, *Phys. Chem. Chem. Phys.*, 2005, **7**, 3297–3305.

S19 A. V Marenich, C. J. Cramer and D. G. Truhlar, *J. Phys. Chem. B*, 2009, **113**, 6378–6396.

S20 A. Dreuw and M. Wormit, *Wiley Interdiscip. Rev.: Comput. Mol. Sci.*, 2015, **5**, 82–95.

S21 N. O. C. Winter and C. Hättig, *J. Chem. Phys.*, 2011, **134**, 184101.

S22 C. Møller and M. S. Plesset, *Phys. Rev.*, 1934, **46**, 618–622.

S23 F. Furche, R. Ahlrichs, C. Hättig, W. Klopper, M. Sierka and F. Weigend, *Wiley Interdiscip. Rev.: Comput. Mol. Sci.*, 2014, **4**, 91–100.

S24 S. Hirata and M. Head-Gordon, *Chem. Phys. Lett.*, 1999, **314**, 291–299.

S25 F. Neese, *Wiley Interdiscip. Rev.: Comput. Mol. Sci.*, 2012, **2**, 73–78.

S26 J. Cerezo and F. Santoro, *J. Comput. Chem.*, 2023, **44**, 626–643.

S27 A. Humeniuk, M. Bužančić, J. Hoche, J. Cerezo, R. Mitrić, F. Santoro and V. Bonačić-Koutecký, *J. Chem. Phys.*, 2020, **152**, 054107.

S28 M. J. Frisch, G. W. Trucks, H. B. Schlegel, G. E. Scuseria, M. A. Robb, J. R. Cheeseman, G. Scalmani, V. Barone, G. A. Petersson, H. Nakatsuji, X. Li, M. Caricato, A. V. Marenich, J. Bloino, B. G. Janesko, R. Gomperts, B. Mennucci, H. P. Hratchian, J. V. Ortiz, A. F. Izmaylov, J. L. Sonnenberg, D. Williams-Young, F. Ding, F. Lipparini, F. Egidi, J. Goings, B. Peng, A. Petrone, T. Henderson, D. Ranasinghe, V. G. Zakrzewski, J. Gao, N. Rega, G. Zheng, W. Liang, M. Hada, M. Ehara, K. Toyota, R. Fukuda, J. Hasegawa, M. Ishida, T. Nakajima, Y. Honda, O. Kitao, H. Nakai, T. Vreven, K. Throssell, J. A. Montgomery, Jr., J. E. Peralta, F. Ogliaro, M. J. Bearpark, J. J. Heyd, E. N. Brothers, K. N. Kudin, V. N. Staroverov, T. A. Keith, R. Kobayashi, J. Normand, K. Raghavachari, A. P. Rendell, J. C. Burant, S. S. Iyengar, J. Tomasi, M. Cossi, J. M. Millam, M. Klene, C. Adamo, R. Cammi, J. W. Ochterski, R. L. Martin, K. Morokuma, O. Farkas, J. B. Foresman and D. J. Fox, *Gaussian 16*, *Revision C.01*, Gaussian, Inc., Wallingford CT, 2016.